

Quantitative investigation of point defects and their dynamics in focused ion beam-prepared group III-nitride lamellas by off-axis electron holography

Keyan Ji

Information

Band / Volume 105

ISBN 978-3-95806-782-0

Forschungszentrum Jülich GmbH
Ernst Ruska-Centrum für Mikroskopie und Spektroskopie mit Elektronen (ER-C)
Physik Nanoskaliger Systeme (ER-C-1)

Quantitative investigation of point defects and their dynamics in focused ion beam-prepared group III-nitride lamellas by off-axis electron holography

Keyan Ji

Schriften des Forschungszentrums Jülich
Reihe Information / Information

Band / Volume 105

ISSN 1866-1777

ISBN 978-3-95806-782-0

Bibliografische Information der Deutschen Nationalbibliothek.
Die Deutsche Nationalbibliothek verzeichnet diese Publikation in der
Deutschen Nationalbibliografie; detaillierte Bibliografische Daten
sind im Internet über <http://dnb.d-nb.de> abrufbar.

Herausgeber
und Vertrieb: Forschungszentrum Jülich GmbH
 Zentralbibliothek, Verlag
 52425 Jülich
 Tel.: +49 2461 61-5368
 Fax: +49 2461 61-6103
 zb-publikation@fz-juelich.de
 www.fz-juelich.de/zb

Umschlaggestaltung: Grafische Medien, Forschungszentrum Jülich GmbH

Druck: Grafische Medien, Forschungszentrum Jülich GmbH

Copyright: Forschungszentrum Jülich 2024

Schriften des Forschungszentrums Jülich
Reihe Information / Information, Band / Volume 105

D 82 (Diss. RWTH Aachen University, 2024)

ISSN 1866-1777
ISBN 978-3-95806-782-0

Vollständig frei verfügbar über das Publikationsportal des Forschungszentrums Jülich (JuSER)
unter www.fz-juelich.de/zb/openaccess.



This is an Open Access publication distributed under the terms of the [Creative Commons Attribution License 4.0](https://creativecommons.org/licenses/by/4.0/),
which permits unrestricted use, distribution, and reproduction in any medium, provided the original work is properly cited.

Contents

1	Introduction	7
2	Theoretical background and experimental details	11
2.1	Transmission electron microscope: Theoretical background	11
2.1.1	Parallel illumination vs. scanning mode	12
2.1.2	Electron holography	13
2.1.3	High angle annular dark field imaging	19
2.1.4	Energy dispersive X-ray spectroscopy	22
2.1.5	Convergent electron beam diffraction	24
2.2	Experimental details	25
2.2.1	Lamella preparation	25
2.2.2	Lamella crystalline thickness determination	27
2.2.3	Electron holography	28
2.2.4	STEM and EDX: Strain and chemical composition measurement	32
2.3	Sample description	33
2.3.1	A3162	33
2.3.2	A3777	34
3	FIB damage and its implication for quantification of electron holographic results	37
3.1	FIB damage types and sub-layers	37
3.1.1	Amorphous outer shell	38
3.1.2	Defect-rich crystalline inner shell	39
3.2	Previous handling of FIB damaged (dead) layers	46
3.3	Simulation of the electron holography results	50
3.3.1	Modelling of surface Fermi-level pinning: Case of III-nitride	51
3.3.2	Self-consistent electrostatic potential calculation	56
3.3.3	From electrostatic potential to electron optical phase	64
4	Electrostatic versus diffraction contribution to electron holography: An experimental approach	67
4.1	Overview	67
4.2	Results	67

4.3	Discussion	71
4.4	Summary	72
5	Origin of phase contrast of modulation-doped GaN	75
5.1	Overview	75
5.2	Results	75
5.3	Discussion	78
	5.3.1 Origin of the phase contrast across the GaN doping step . .	78
	5.3.2 Comparison with <i>n</i> -type GaN structures from references . .	81
5.4	Summary	82
6	Quantification of surface effect: Fermi-level pinning by substitutional C	83
6.1	Overview	83
6.2	Results	83
	6.2.1 Single-cycle in-situ annealing	83
	6.2.2 Two-cycle in-situ annealing	84
	6.2.3 Ambient exposure and electron beam irradiation	87
	6.2.4 Self-consistent electrostatic potential calculation: Surface Fermi-level pinning	88
6.3	Discussion	91
	6.3.1 Type of FIB-implanted point defect	91
	6.3.2 Implantation of C _N by FIB	93
	6.3.3 Discussion of the healing process	95
6.4	Summary	96
7	Thermal dynamics of Fermi-level pinning: Substitutional C site switching	99
7.1	Overview	99
7.2	Electron holography results	99
7.3	Data analysis	103
	7.3.1 Time constant analysis	103
	7.3.2 Derivation of activation barrier and diffusion length	104
7.4	Discussion	107
7.5	Summary	108
8	A demonstration on quantification of phase map: Case of (Al,In)N/GaN interface	111
8.1	Overview	111
8.2	Results	111
	8.2.1 Electron holography	111
	8.2.2 High resolution STEM	112

8.3	Self-consistent electrostatic potential calculation	119
8.3.1	Relevant fixed parameters	119
8.3.2	Effect of mean inner potential	120
8.3.3	Effect of electron affinity and polarization	121
8.3.4	Influence of the In composition gradient in (Al,In)N on phase map	123
8.4	Discussion: Origin of the composition gradient	126
8.5	Summary	128
9	Conclusion	129
	Abstract	133
	Acronym list	137
	List of own publications	139
	Bibliography	141
	Acknowledgement	163

Chapter 1

Introduction

Group III-nitride semiconductors and their alloys have gained significant attention due to their remarkable electronic properties, making them materials of choice in present technological applications, including opto-electronic and high power applications. They exhibit a direct bandgap, with an energy of ~ 0.7 eV,[1] ~ 3.4 eV,[2] and ~ 6.1 eV[3] for wurtzite InN, GaN, and AlN, respectively. The wide range of bandgaps provides an opportunity to engineer the emitted light wavelength from infrared to ultraviolet (UV) by utilizing alloys with different compositions.[4]

GaN stands out as the most widely used material among them, offering advantages such as reduced switching losses, higher breakdown voltage, increased stability in high-temperature operations, and improved irradiation hardness, as compared to the standard Si technology.[5] GaN is, for instance, utilized in the fabrication of devices withstanding high voltages such as insulated gate bipolar transistors (IGBTs).[6, 7, 8] These advantages also make GaN and (Al,Ga)N ideal for efficient power conversion applications.[8, 9, 5] Furthermore, the possibility of growing heterostructures consisting of binary and ternary nitrides further expands the range of applications. For instance, in high-electron-mobility transistor (HEMT) based on (Al,Ga)N/GaN heterostructures, the resulting two-dimensional electron gas (2DEG) at the hetero-interface leads to superior high frequency electron transport in the conductive channel.[10, 11]

The operation of these III-nitrides-based devices relies on whether the alloy composition, abruptness of the interfaces, the polarization, as well as the doping profile and consequently, the electrostatic potential distribution, is achieved as intended. Therefore, there is a substantial need for high spatial resolution characterization and mapping of carrier concentrations and related electrostatic potentials. However, accomplishing this is non-trivial and highly challenging:

For instance, doping profiles along the growth direction are commonly measured by the secondary ion mass spectroscopy (SIMS). However, SIMS lacks the lateral

resolution and does not provide information about the active dopant, thus leading to a loss of knowledge regarding the electric properties.

Conventional electrical characterization such as capacitance–voltage (C–V) spectroscopy and Hall measurement can assess the carrier density in semiconductors directly. Nevertheless, these techniques possess restrictions on the size and shape of samples and lack of high spatial resolution.

Scanning probe microscopy (SPM) is a powerful tool in the field of semiconductor physics, allowing for investigation of various properties, including visualizing individual dopants,[12, 13] electrostatic potential mapping,[14, 15, 16] and carrier density measurement.[17] The most widely used techniques include the scanning capacitance microscopy (SCM),[18, 19] the scanning spreading resistance microscopy (SSRM),[20, 21] scattering-type scanning near-field optical microscopy (s-SNOM),[22, 23] and scanning tunneling microscopy (STM).[24, 12, 25, 13, 14, 26, 16] However, all SPM-based techniques are highly surface-sensitive. Therefore, achieving a flat and clean surface is critical, and any artifacts or contamination can affect the accuracy of the measurements. In addition, it may not provide a comprehensive understanding of the bulk properties of a material.

Electron holography, in contrast, can be used to probe the carrier concentration and electrostatic potentials of bulk-like sample (projected in the electron beam direction) with high spatial and energy resolution. Distinct to most conventional transmission electron microscope (TEM) techniques that solely record spatial distributions of image intensity, electron holography enables the direct measurement of the phase change of the electron wavefunction that has passed through the sample. This phase change can then be utilized to retrieve information about local variations in electrostatic potential in the semiconductor at high spatial resolution.[27, 28] Indeed, large amount of efforts has been dedicated to map the electrostatic potential in III-nitrides with electron holography.[29, 30, 31, 32, 33, 34] However, previous studies are mostly qualitative as the influence of amorphized surface layers and defects implanted in the near-surface region during focused ion beam (FIB) preparation process are neglected. As I will demonstrate in this thesis, the defect-induced surface potential on FIB-prepared lamellas greatly influence the phase change of transmitted electron wave, and thus the obtained electrostatic potential. Therefore, a quantitative extraction of electrostatic potential from measured phase maps relies on the precise description of these surface damages.

In a precedent work, it has been successfully demonstrated that by modelling the FIB-induced surface damages as surface Fermi-level pinning effect, the electrostatic potential as well as other electronic features, e.g., polarization changes at III-nitride interfaces, can be quantitatively extracted.[35] In this thesis, utilizing the same

theoretical modelling framework, I push forward the investigation, placing specific emphasis on identifying the type of FIB-induced point defects in GaN as well as their dynamics and reactions upon annealing. This will be applied in a final step to characterize (Al,In)N/GaN interfaces quantitatively.

This thesis is structured as follows: In Chap. 2, the theoretical background of the TEM-related techniques is first introduced, with emphasis on off-axis electron holography. The chapter further describes the details of the experiments and samples used.

In Chap. 3, the formation, implantation, and diffusion process of native point defects as well as extrinsic impurities in GaN are recalled briefly. In addition, it provides a comparison between previous and present approaches in handling the FIB-induced damages. Finally, I present the theoretical methodology of the self-consistent electrostatic potential calculation of III-nitrides, taking the surface Fermi-level pinning into account. Special emphasis is laid on the effects of strain, chemical composition, band alignment, and polarization.

Chapter 4 investigates the conditions for acquiring holograms with negligible dynamic diffraction contrast using off-axis electron holography.

In Chap. 5, the physical origin of the giant enhancement of phase contrast measured across the $n^+ - n$ GaN doping structure is unraveled. The predominant contribution to the phase contrast is shown to arise from the doping dependent screening length of the FIB-induced surface Fermi-level pinning occurring in the defect-rich crystalline inner shell of the TEM lamella. The contribution of the built-in potential is negligible for modulation doping and only relevant for large built-in potentials at e.g. $p - n$ junctions.

In Chap. 6, the thermal healing of FIB-implanted defects in GaN is investigated. The data reveal that healing starts at temperatures as low as about 250 °C. The healing processes result in an irreversible transition from defect-induced Fermi-level pinning near the valence band toward a midgap pinning induced by the crystalline-amorphous transition interface of the TEM lamella. Based on the measured pinning levels and the defect charge states, the dominant defect type is identified to be substitutional carbon on nitrogen sites.

In Chap. 7, off-axis electron holography is utilized to identify point defect dynamics by probing the time and temperature dependence of the surface Fermi-level pinning upon annealing. The methodology is illustrated using FIB-implanted carbon in GaN, where a site switching process of C, from substitutional to interstitial, is found to be responsible for lifting the Fermi-level pinning in the lower part of the

bandgap. The carbon site switching process has an activation barrier energy of 2.27 ± 0.26 eV.

In Chap. 8, the findings from previous chapters are included to probe the polarization changes at the (Al,In)N/GaN interface. This involves a systematic characterization of complete set of relevant parameters, including surface Fermi-level pinning, strain, chemical composition, and lamella thickness etc. A composition gradient along the growth direction is observed within the (Al,In)N layer. This is attributed to the rebuilding of a group III adlayer after growth interruption. On the basis of these measured parameters, a self-consistent electrostatic potential calculation is conducted, using polarization change as a fitting parameter. Through the quantitative comparison between the measurements and the calculated results, a polarization change of -2.2 ± 0.7 mC/m² at the Al_{0.81}In_{0.19}N and GaN interface is unraveled, demonstrating an excellent agreement with the theoretical value.

Chapter 2

Theoretical background and experimental details

2.1 Transmission electron microscope: Theoretical background

The spatial resolution of a microscope is constrained by the Abbe diffraction limit. This limitation indicates that the minimum resolvable distance between two points is approximately half the wavelength of the probing radiation used for imaging, divided by the numerical aperture of the objective lens. Visible light has a wavelength, i.e., typically around 400 to 700 nm, which restricts the minimum resolvable point distance down to about 200 nm. In contrast, inside a Transmission Electron Microscope (TEM), electron exhibits a much shorter wavelength, commonly in the order of picometers, depending on the accelerating voltage. The short wavelength of electron beams allows for much higher resolution, enabling the resolution of finer structures, as the Abbe limit for electron beams is significantly smaller. The abbe limit, however, is not the only factor limiting the resolution for electron microscopy.

As a first-order approximation, electrons with a wavelength of approximately ~ 2 pm (under 300 kV acceleration voltage) would yield an ideal spatial resolution corresponding to a few picometer. However, such a spatial resolution cannot be readily achieved. For a further understanding, I recall the experimental setup of a TEM: The highly-focused electron beam is first generated from a field-emission electron gun (FEG) source. After being emitted from the source, a set of electro-magnetic lens (named as the condenser lens) are employed to shape the electron beam and improve its focus (see Fig. 2.2(a)). Any imperfection or asymmetry in these electro-magnetic lenses can contribute to the distortion of the electron beam, a phenomenon

known as the aberration effect. For instance, spherical aberration (C_s , as shown in Fig. 2.1(a)) occurs when parallel rays of electrons passing through the lens system converge at different points along the optical axis, instead of coming to a single focus. This type of aberration arises because electrons passing through the outer regions of the lens experience a different field compared to those passing through the center, resulting in different focal points. Another type of aberration is the chromatic aberration (C_c , as shown in Fig. 2.1(b)) where the electron beams with different wavelength (or energy) exhibit different focal points.

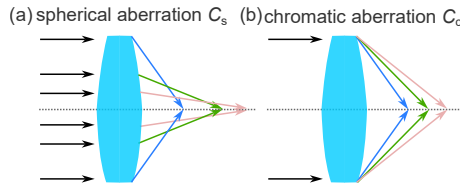


Figure 2.1: Two types of low-order aberration induced by asymmetry of the electron-magnetic lens in TEM: Spherical aberration (a) and chromatic aberration (b).

2.1.1 Parallel illumination vs. scanning mode

A TEM can also work in the scanning transmission electron microscopy (STEM) mode. The key difference between these two techniques lies in the convergence angle of the electron probe at the sample plane. Fig. 2.2 depicts a simplified illumination principle of TEM and STEM: In Fig. 2.2(a), the ray diagram of a TEM is shown where a broad and parallel electron beam is utilized to illuminate the sample. The broad beam illumination has an advantage of allowing access to a relatively large field of view (FOV) and providing highly coherent electron illumination.

Figure 2.2(b) depicts the illumination applied in STEM, where a highly focused electron probe that scans over the sample plane is used. As compared to the illumination in a TEM, the electron beam in STEM has much smaller convergence angle, typically in the range of a few micro to milli-rad. The scanning function is carried out with deflection coils pairs, which enable the deflection of the electron beam in both horizontal and vertical directions on the sample plane. STEM can be performed in conjunction with a various analytical techniques, such as energy-dispersive X-ray spectroscopy (EDX) or electron energy loss spectroscopy (EELS), to unravel the chemical composition and electronic properties of the sample at sub-nanometer scales.[36]

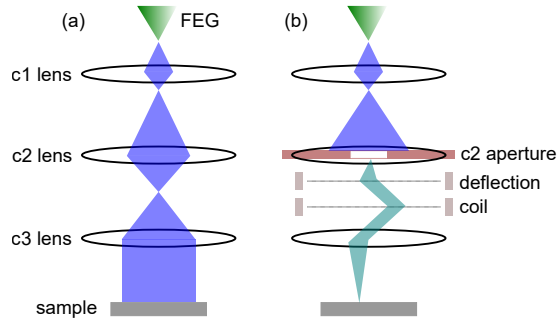


Figure 2.2: A simplified sketch highlighting the different illumination mechanisms of TEM and STEM. (a) Depicts the broad beam illumination applied in TEM, which can be achieved by coupling the strength of c2 and c3 lenses. (b) Illustrates the formation of a highly focused beam applied in STEM. The inserted c2 aperture governs the convergence semi-angle of electron beam. The scan function of STEM is enabled with the deflection coils.

Note that conventional TEM and STEM techniques enable the extraction of intensity of the transmitted electron wavefunction I (i.e., the square of amplitude), whereas the phase information is lost.

2.1.2 Electron holography

Methodology

Electron holography, as an advanced technique based on TEM, offers a distinctive advantage over conventional TEM techniques. It allows direct access to both the amplitude and the phase of the wavefunction of transmitted electrons.[28] In this thesis, off-axis electron holography is used.

Fig. 2.3 depicts the ray diagram of a conventional TEM and an off-axis electron holography after the sample plane. The intermediate and projector lens after the selected-area aperture are neglected for the sake of simplicity. For the conventional TEM (Fig. 2.3(a)), the transmitted electron beam is first focused with the objective lens. The objective aperture is inserted at the back focal plane as a spatial filter, allowing electrons with the appropriate scattering angle to pass and contribute to the image.

As for the off-axis electron holography (Fig. 2.3(b)), the experimental setup is designed in a manner such that a portion of the incoming electron beam is allowed

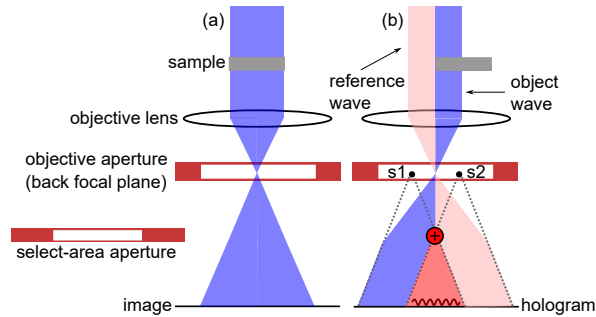


Figure 2.3: Schematic illustration of ray paths in the conventional TEM and off-axis electron holography. The subsequent intermediate and projector lens are omitted in the figure for simplification. (a) Ray diagram of a conventional TEM. The objective aperture is used as a spatial filter for the image-forming electrons. (b) Ray diagram of an off-axis electron holographic setup. A portion of the incoming electron beam, transmits through the sample (the object wave, depicted as the blue ray), while the remaining electrons pass through the nearby vacuum (the reference wave, depicted as the pink ray). With a biased biprism placed at select-area aperture position, the object and reference waves are overlapped and giving rise to a hologram. The virtual sources s1 and s2 for overlapped objective and reference wave are also displayed at the back focal plane, respectively.

to pass through the electron transparent sample (denoted as object wave, represented by the blue ray), while another portion passes the vacuum nearby (denoted as reference wave, depicted as the pink ray). A biased biprism is inserted at the position of the select-area aperture, enabling the overlap of the reference and object wave. Interfering the object and reference wave gives rise to the formation of a hologram containing interference pattern where the recorded intensity distribution $I(r)$ is given as:

$$I(r) = 1 + A^2(r) + 2A(r)\cos(2\pi q_c r + \phi(r)) \quad (2.1)$$

where q_c is the carrier frequency of interference fringes. $A(r)$ and $\phi(r)$ represents the amplitude and phase of the wavefunction, respectively.[37]

An important parameter characterizing the quality of a hologram is the contrast of fringes (FC):

$$FC = \frac{I_{\max} - I_{\min}}{I_{\max} + I_{\min}} \quad (2.2)$$

where I_{\max} and I_{\min} are the maximum and minimum intensities of the interference

fringes, respectively.[38] As a rule of thumb, the higher is the numerical value of FC , the better is the coherence of transmitted electron beam.

Following the acquisition of an object hologram, a reference hologram without sample is obtained under the same optical settings. This step is carried out in order to compensate artifacts that arise due to, e.g., distortions from the projector lens system[39] as well as charging effects induced by the lens and biprism systems. Examples of an object and corresponding reference hologram are displayed in Fig. 2.4(a) and (b), respectively. To retrieve the phase and amplitude information from the hologram, a reconstruction process is required. This process involves two main steps: First, the object and reference holograms undergo a Fourier transformation \mathcal{F} to obtain their corresponding spectra in the reciprocal space, as shown in Fig. 2.4(c). The Fourier transformation of a hologram has three components:

$$\mathcal{F}(I(r)) = \mathcal{F}(1 + A^2(r)) + \delta(q + q_c) \otimes \mathcal{F}(A(r)e^{i\phi(r)}) + \delta(q - q_c) \otimes \mathcal{F}(A(r)e^{-i\phi(r)}) \quad (2.3)$$

where the first term is derived from the Fourier transform of a bright-field TEM image and corresponds to the center peak in the reciprocal space. The two side bands located at $q = -q_c$ and $q = q_c$ are derived by the Fourier transform of wavefunction (i.e., $A(r)e^{i\phi(r)}$) and its conjugate (i.e., $A(r)e^{-i\phi(r)}$), respectively. In the second step, a circular mask is applied to the side band correlated to the carrier frequency q_c , as depicted by the green circle in Fig. 2.4(c). This process deletes all information further away from the masked side band in the reciprocal space. Following the mask process, the side band is displaced to the center of the reciprocal space, followed by an inverse Fourier transformation \mathcal{F}^{-1} . This inverse Fourier transformation step yields a complex image containing both phase and amplitude information. Finally, the distortions arising from the lens and biprism are corrected by performing the complex division of the object and reference complex images.

The phase image (Fig. 2.4(d)) of the transmitted electrons is generated by calculating the arctangent ratio of the imaginary and real parts of the complex image, while the amplitude image is obtained from the square root of the sum of the squares of the imaginary and real parts. It is worth mentioning that the evaluation of the complex wave image utilizing an arc-tan function inevitably limits the phase into a 2π range. Hence, an unwrap algorithm is required to unfold the phase in full range. Note that the phase of the transmitted electrons is determined with respect to that of the (unperturbed) electrons passing through the vacuum. Therefore, the measured phase does not represent the absolute phase of the transmitted electron wavefunction, but rather the phase change/shift $\Delta\phi$.

In the absence of dynamical diffraction and in-plane magnetic fields, the phase

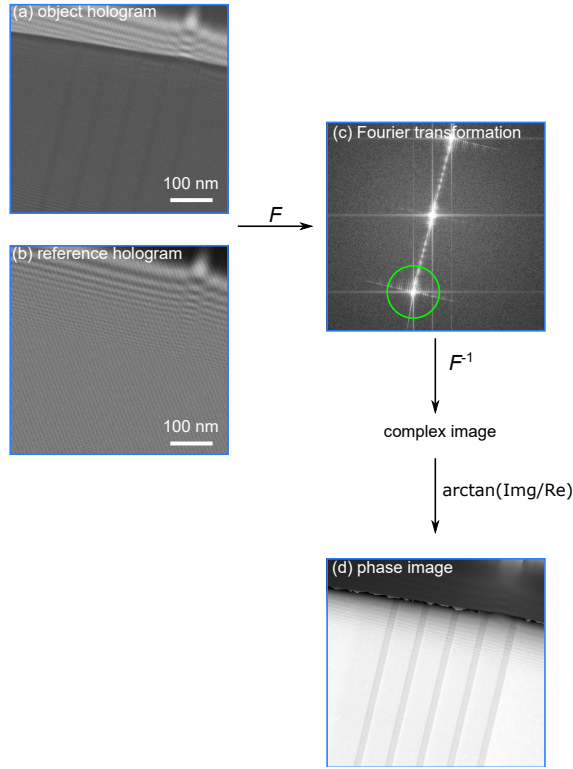


Figure 2.4: (a) Exemplary object hologram obtained in nitride sample. (b) Reference hologram acquired without sample under the identical optical setups. (c) Fourier transformation of the holograms. The side band highlighted by the green circle is chosen and masked for the inverse Fourier transform, which generate a complex image containing both phase and amplitude information of transmitted electrons. (d) Phase image is retrieved by using the arctangent ratio of the imaginary and real parts of the complex image.

change of transmitted electrons $\Delta\phi(x, y, z)$ is given as the integral of electrostatic potential along incoming electron beam direction z within the sample: [40]

$$\Delta\phi(x, y, z) = C_E \int (V_{EP}(x, y, z) + V_{MIP}(x, y, z)) dz \quad (2.4)$$

where C_E is a constant depending on the energy of the incoming electron beam (hence the acceleration voltage). The electrostatic potential can be separated into

two contributions, one is correlated to the Coulomb interaction between core electrons and nucleus (denoted as mean inner potential V_{MIP}), which can be considered as a material constant. Another contribution accounts for the built-in potential as well as externally applied potential (together denoted as V_{EP}). Under the assumptions of (i) uniform sample thickness t , (ii) a constant electrostatic potential distribution along z direction, and (iii) no stray field in the vacuum, Eq. (2.4) is simplified to:

$$\Delta\phi(x, y) = C_{\text{E}}(V_{\text{EP}}(x, y) + V_{\text{MIP}}(x, y))t. \quad (2.5)$$

This equation directly relates the electrostatic potential to the phase change measured from electron holography.

Electron holography artefacts

However, retrieving the phase change of transmitted electrons is not straightforward due to the potential presence of artefacts. The following discussion addresses several notable types of artifacts in electron holography and introduces methods to effectively suppress their influences.

(i) Fresnel fringe: While the contrast originated from the Fresnel effect is beneficial in various TEM applications, as it provides valuable insights into, for instance, the study of grain boundaries,[41] lattice defects,[42, 43] and magnetic domain walls.[44, 45] In the context of electron holography, however, the Fresnel fringes are often viewed as a source of measurement artefacts. For the electron holography using a single biprism, as employed in this thesis, Fresnel fringes are evident. At the edges of the biprism, Fresnel fringes manifest with alternating bright-dark contrast and can be readily observed. A hologram acquired in the vacuum is displayed in Fig. 2.5(a), the enlarged view of the Fresnel fringes occurring at the biprism edges are depicted in Fig. 2.5(b) and (c).

The Fresnel fringes can be reduced by masking their corresponding streaks in the Fourier space. In actual practise, such an operation can be accomplished using line-filters. Examples of the hologram with strong Fresnel fringes (in regions denoted with dotted lines) and the corresponding Fourier transformation are displayed in Fig. 2.6(a1) and (a2), respectively. It can be noticed that these fringes are reflected as a few streaks extending from the center band to the side bands. In contrast, a hologram with reduced intensity of Fresnel fringes is depicted in Fig. 2.6(b1). This is achieved after masking the streaks with a Gaussian-line filter in the Fourier space (Fig. 2.6(b2)).

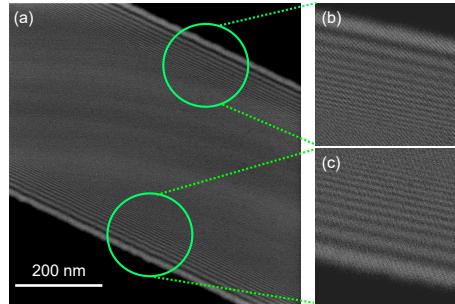


Figure 2.5: (a) Hologram obtained in the vacuum. (b,c) Enlarged views of the Fresnel fringe occurring at the biprism edges

(ii) Electron beam induced charging: When the semiconductor sample is under investigation in TEM, the charging effect arising from the incoming electron beam needs to be considered. Electrons accelerated at high voltages can give rise to the generation of electron-hole pairs and emission of secondary electrons. As a result, the sample can be anticipated to, at least locally, no longer charge neutral. This is known as the electron beam induced charging effect.[37]

Houben *et al.* investigated the charging of Si *p-n* junction in TEM. Their results suggest that, under moderate electron dose illumination (e.g., below $100 \text{ e}\cdot\text{nm}^{-2}\text{s}^{-1}$), only the junction with low doping level (i.e., less than $1 \times 10^{17} \text{ cm}^{-3}$) is significantly influenced from the beam-induced charging.[46] Another work focusing on the charging of a highly doped GaN *p-n* junction during electron holography experiment is carried out by Park *et al.*[47] They found that the built-in potential decreases from 0.51 to 0.32 V after exposing the sample under a high electron dose of $332 \text{ e}\cdot\text{nm}^{-2}\text{s}^{-1}$ for an hour. On the basis of these findings, the artifacts arising from the charging effect can be anticipated to be evident in structures with low doping levels or when the sample is subjected to high electron beam dose illumination.

(iii) Dynamic diffraction: Contrast arising from dynamic diffraction severely hampers the interpretability of the electron holographic results. The dynamic diffraction describes a process in which incoming electrons undergo multiple Bragg scatterings within the crystal. This occurs, if the direction of the incoming electron beam is parallel to the low-order crystal zone axis of the semiconductor. The contrast arising from dynamic diffraction can overlap with the contrast originating from the actual electrostatic potential of the sample. This overlap leads to artificial errors during the reconstruction, which, in turn, distorts the phase and amplitude information of transmitted electrons. As a result, the interpretation of the experimental

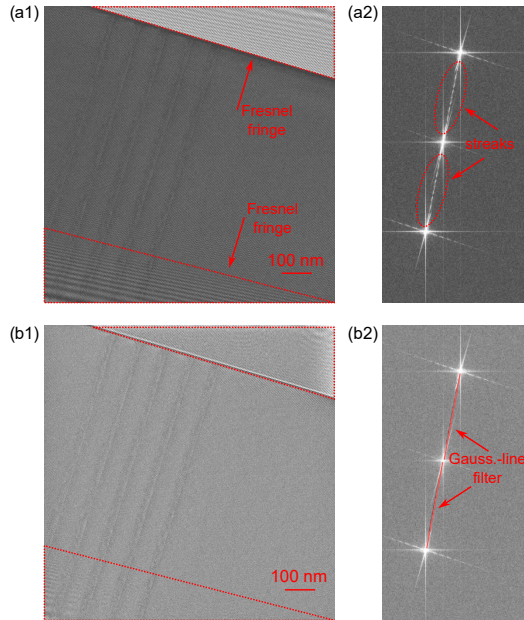


Figure 2.6: (a1) Hologram with strong Fresnel fringes, induced by the biprism, and (a2) the corresponding Fourier transformation of the hologram. (b1) Hologram with reduced Fresnel fringes. This reduction is accomplished by filtering the streaks in the Fourier space, as depicted in (b2).

data becomes challenging. To avoid strong dynamic diffraction, one can adjust the relative orientation between the incoming electron beam and the sample so that the beam is no longer parallel to any major crystallographic axis. A systematic method to suppress the dynamic diffraction across III-nitride heterostructure interface will be discussed in Chap. 4.

2.1.3 High angle annular dark field imaging

Before the discussion on different detectors of TEM/STEM, one needs to recall the fundamental scattering process of electrons by solid: From the energy perspective, the scattering process can be categorized into elastic and inelastic scattering. Elastic scattering involves no loss of energy, while inelastic scattering results in some measurable energy loss, although this loss is typically very small in comparison to the total energy of the incoming electron beam. On the other hand, from the

point of view of coherence of electron wavefunctions, the scattering process can be divided into coherent and incoherent scattering. After scattering with sample, coherently scattered electrons maintain a phase relationship, whereas such in-phase correlation no longer exists for incoherently scattered electrons. In addition, the scattering process can lead to different angular distributions of scattered electrons. On this basis, the scattering process can be classified into forward scattering and back scattering, depending on the angle of scattering with respect to the direct transmitted beam. If an electron is scattered at an angle larger than 90° (an angle less than 90°), it is considered as forward scattered (backward scattered).

Fig. 2.7 depicts a sketch of different types of electrons scattered by thin TEM sample. As a rule of thumb, elastically scattered electrons exhibit a scattering angle in the range of $1\text{-}10^\circ$, at higher angles ($>10^\circ$) elastic scattering becomes more incoherent. Inelastic scattering, on the other hand, is almost always incoherent and typically occurs at very low angles, usually less than 1° . As for the application in TEM/STEM, most of electrons collected is within a scattering angle of less than 5° . [48]

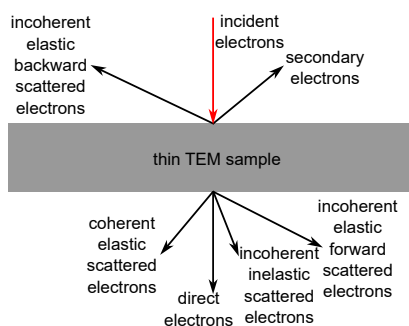


Figure 2.7: A sketch of different types of electrons scattered from a thin TEM sample.

Next, I turn to the detectors utilized in a conventional STEM. Detectors with various collection angles (denoted as θ) are used to collect electrons scattered at different angles. Depending on the collection angles, detectors are categorized as bright field (BF), dark field (DF), and high-angle annular dark field (HAADF) detector.

Fig. 2.8 illustrates different detectors used in STEM. The outer collection angle of BF, and inner collection angle of DF and HAADF detector are denoted as θ_1 , θ_2 , and θ_3 , respectively. The BF detector is applied for collecting the unscattered or weakly scattered electrons with a collection angle less than 10 mrad . [36] The DF detector is

used to collect electrons that are scattered at higher angles, typically ranging from 10 to 50 mrad. Furthermore, the HAADF detector allows the collection of nearly-elastically scattered electrons at an even higher angle of scattering, typically ranging from 50 to 200 mrad.[36] It's worth mentioning that, in contrast to BF images, the electrons forming contrast in HAADF images are primarily incoherent due to Rutherford and thermal diffuse scattering (TDS).[49] The resulting image exhibits a contrast that is directly proportional to the atomic number of the atoms in the sample (known as the Z -contrast). This provides a direct method to distinguish atom species based on their atomic numbers.[50, 51]

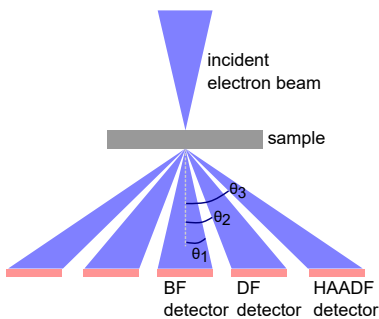


Figure 2.8: Different detectors used in STEM. The outer collection angle θ_1 of BF detector is lower than 10 mrad. As for the DF and HAADF detector, the inner collection angles θ_2 and θ_3 are larger than 10 and 50 mrad, respectively.

At this stage, the formation mechanism of Z -contrast needs to be addressed. The Rutherford cross-section, denoted by σ , quantifies the probability of a charged particle to be scattered by a target nucleus. If the electrons are accelerated at a high voltage, the Rutherford cross-section is reasonably accurate to describe the scattering events between incoming electrons and nuclei within the sample.

To derive the total scattering intensity ($I_{\text{scatt.}}$) between the electrons and nuclei, it is necessary to consider the scattering contributions from both the differential cross-sections of elastic scattering and thermal diffuse scattering, they are given as:[52]

$$\left(\frac{d\sigma}{d\Omega}\right)_{\text{tot}} = \left(\frac{d\sigma}{d\Omega}\right)_{\text{elastic}} + \left(\frac{d\sigma}{d\Omega}\right)_{\text{TDS}} \quad (2.6)$$

with

$$\left(\frac{d\sigma}{d\Omega}\right)_{\text{elastic}} = \frac{4\gamma Z^{1.7} \exp(-2M\theta^2/\lambda^2)}{a_0^2 k_0^2 (\theta^2 + \theta_0^2)^2} \quad (2.7)$$

and

$$\left(\frac{d\sigma}{d\Omega}\right)_{\text{TDS}} = \frac{4\gamma Z^{1.7} (1 - \exp(-2M\theta^2/\lambda^2))}{a_0^2 k_0^2 (\theta^2 + \theta_0^2)^2}, \quad (2.8)$$

respectively. γ is the relativistic factor which has a value of 1.59 at 300 keV and $a_0=0.0529$ nm is the Bohr radius. θ_0 is the characteristic angle of elastic scattering, k_0 is the wavevector, and M is the Debye–Waller factor. λ is the wavelength of the incoming electron, with a value of $\lambda=1.97$ pm at 300 kV. The scattering intensity of electrons can then be obtained by integration of differential cross-section over a range extending from the inner HAADF detector angle (θ_{inner}) to the outer detector angle (θ_{outer}):

$$I_{\text{scatt.}}(\theta) = \int_{\theta_{\text{inner}}}^{\theta_{\text{outer}}} \left(\frac{d\sigma}{d\Omega}\right)_{\text{tot}} d\Omega = \int_{\theta_{\text{inner}}}^{\theta_{\text{outer}}} \frac{4\gamma Z^{1.7}}{a_0^2 k_0^2 (\theta^2 + \theta_0^2)} d\Omega \quad (2.9)$$

Hence, to the first order of approximation, scattering intensity of electrons collected by a HAADF detector is considered to be proportional to the power of ~ 1.7 of the atomic number Z , i.e., $I(\theta) \propto Z^{1.7}$. [51] For this reason, these electrons carry information about variations in material's chemical homogeneity. [51, 53, 54, 55]

2.1.4 Energy dispersive X-ray spectroscopy

Energy Dispersive X-ray Spectroscopy (EDX) is an analytical technique to determine the chemical composition of the sample. In this thesis, EDX is carried out in conjunction with the STEM in order to provide chemical composition mapping at high spatial resolution.

After the collision between the accelerated electrons and solid, the inner shell electrons in the solid can be displaced from their orbits, leaving vacancies. Following, electrons from outer shells will transit to inner shells and fill these vacancies, releasing excess energy in the form of characteristic X-rays. These X-rays are then collected by an EDX detector and analyzed. The analysis results are given as a spectrum of X-ray intensity counts versus their corresponding energies. In this spectrum, each peak corresponds to the characteristic X-rays generated by the specific elements within the sample. [56] An example of EDX spectrum acquired on GaN is displayed in Fig. 2.9. The Ga-L, Ga-K, and N peaks are high-lightened.

The accuracy of EDX analysis depends on a variety of factors, including the incoming electron beam size and intensity, detector conditions, as well as sample's characteristics. [57, 58, 59] For instance, if the electron dose is too high, it can damage the sample and alter its composition, leading to inaccurate results. Such a

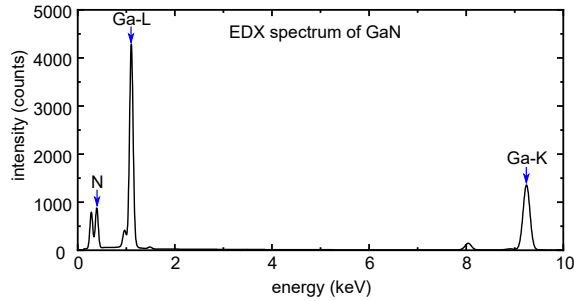


Figure 2.9: EDX spectrum acquired on the GaN layer.

perturbation of sample's characteristics by electrons can be found in various materials, for example, in LaCoO_3 epitaxial layers, oxygen atoms are displaced from their original lattice sites by long and high dose electron exposure.[58] Furthermore, the energy resolution of the detector is of great importance in terms of quantification of the EDX results. With an optimized resolution, the overlap of characteristic peaks in the EDX spectrum can be avoided, thus enabling the identification of correct element species.[59] In addition, X-rays can be absorbed by the materials themselves, particularly in the case of thick TEM samples. This process is referred to as re-absorption. As a result of re-absorption effect, the measured X-ray intensities are influenced not only by the chemical composition but also by factors such as escape depth and the sample's absorption characteristics.

In this thesis, analysis of the EDX results is performed with the Velox software. This software adopts the standard Cliff-Lorimer method (K -factor method) to quantify EDX spectrum. The K -factor method is a semi-empirical method that relates the intensity of an X-ray peak in the spectrum to the weight fraction of elements in the sample.[60] In addition, a correction factor (CF) is introduced into the quantification process to account for the re-absorption process of X-ray by the sample.

Here, a brief description of the workflow involved in the EDX spectrum quantification process is provided: The first step involves the elimination of background radiation and noise. This step is necessary to distinguish the intensity counts that are relevant for peak fitting. The background correction is carried out by fitting a curve to the counts in the selected energy ranges. Once the background is removed, the characteristic peaks are fitted using the ionization cross-section model. Overlapped X-ray peaks are then deconvoluted using a maximum likelihood fit with constraints to ensure non-negativity. Finally, quantitative chemical informa-

tion is obtained using the Cliff-Lorimer method, taking absorption corrections into account. Therefore, the weight fraction of A-B compound C_A/C_B is derived as:

$$\frac{C_A}{C_B} = CF \frac{K_A I_A}{K_B I_B} \quad (2.10)$$

with I_A and I_B being the X-ray intensity accounting for element A and B, respectively.

2.1.5 Convergent electron beam diffraction

In this thesis, the thickness of TEM lamellas is determined through two methods, a direct measurement in scanning electron microscope (SEM) images, and indirectly with convergent beam electron diffraction (CBED). The first method only yields a rough estimation of the thickness of the overall sample due to a rather limited spatial resolution, whereas the latter provides measurement of the crystalline thickness but at a cost of poor sampling due to small probe size.

Although SEM measurements may appear to be straightforward, the accuracy of the measured thickness is questionable due to the presence of common artefacts arising during the sample preparation process. For instance, in lamella prepared by focused ion beam (FIB) milling, the curtaining effect and the amorphization of crystalline material can give rise to misleading measurements and make it challenging to obtain precise thickness data.[61]

In contrast, CBED provides a localized measurement of crystalline thickness with an improved precision down to only a few nanometers.[62, 63] This technique relies on the analysis of spacings between fringes (known as Kossel-Mollenstedt fringes[64]) in the reflection disks.[63] Under two-beam condition, only the (000) and another hkl reflection disk is strongly excited. These two reflection disks contain parallel fringes with alternating bright and dark contrast. The central bright (dark) fringe in (000) (higher order hkl disk) is at the exact Bragg condition (i.e., the excitation error $s=0$). The number of fringes inside reflection disks depends on the thickness of the crystal and increases by one if the thickness increases by one extinction length. The spacing between central and the other i^{th} fringes corresponds to the deviation from the Bragg diffraction angle ($\Delta\theta_i$). Hence, the excitation error s_i for the i^{th} fringe is derived as:

$$s_i = \lambda \frac{\Delta\theta_i}{2\theta_B d_{\text{plane}}^2} \quad (2.11)$$

where θ_B is the Bragg angle of the hkl -plane. d_{plane} is the interplanar spacing between hkl planes in real space.

The direct interpretation of thickness from Eq. (2.11) requires the knowledge of extinction distance of the material ε_g , which is not always explicitly defined. Therefore, the so-called graphic method is used to retrieve the crystalline thickness information.[63] This method is based on the extrapolation of the equation of thickness t and ε_g which is given as:

$$\frac{s_i^2}{n^2} + \frac{1}{\varepsilon_g^2 n^2} = \frac{1}{t^2} \quad (2.12)$$

where n is a fitting integer starting from 1. When data points can be reasonably fitted in a linear manner, the intercept and slope of the fitting line are then proportional to the thickness t and extinction distance ε_g , respectively.

2.2 Experimental details

2.2.1 Lamella preparation

In this thesis, a dual-beam focused ion beam FIB milling system (model FEI Helios NanoLab 400S FIB-SEM) is employed to prepare TEM lamellas. An example illustrating a workflow for TEM lamella preparation by FIB is displayed in Fig. 2.10. Before milling, a protective layer is first deposited onto the surface of bulk semiconductor by 5 kV electron beam and with a dose of 6.4 nA (Fig. 2.10(a)). Note that the protective layer deposited with electron beam is rather thin. Thus, another 2 μm protective layer is deposited with Ga^+ ion beam at 30 kV and with a dose rate of 0.77 nA (Fig. 2.10(b)). In general, a variety of chemical species, such as carbon, tungsten, and platinum, etc., can be used as the protective layer. For all the lamellas investigated in this thesis, only the carbon protective layer is utilized. Following the deposition of protective layer, the lamella is trenced along its cross-sectional surfaces, undercut, and lifted out of the bulk semiconductor, as shown in Fig. 2.10(c), (d), and (e), respectively.

The parameters and procedures used during the thinning and polishing process depend on the specific experimental demands, whether it be a thick lamella for electron holography measurements or a thinner lamella for high-resolution STEM measurements.

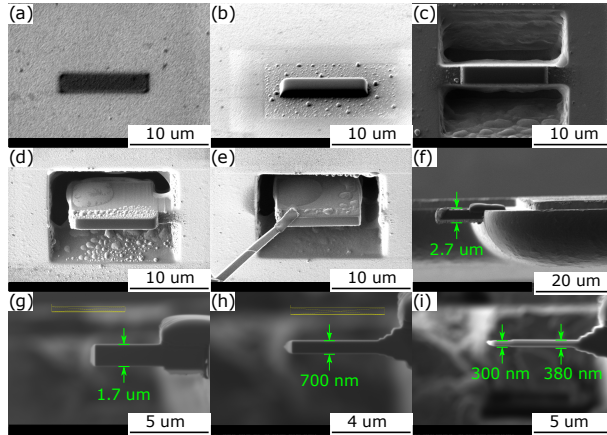


Figure 2.10: The workflow of lamella preparation by FIB. (a) The C protective layer is first deposited with electron beam, and then with ion beam (b). (c)-(e) Illustrate the trench, undercut, and lift-out processes. (f)-(h) Display the different thinning steps that progressively reduce the lamella thickness. In (i), the final TEM lamella geometry is shown, intentionally exhibiting two different thicknesses.

(i) Regarding the electron holographic investigation, the incoming 30 kV Ga^+ ion beam, with a dose of 0.77 nA, is applied for the first thinning step (Fig. 2.10(f)). At this step, the lamella is thinned down to approximately 1700 nm with a grazing angle of $\pm 2^\circ$ with respect to the Ga^+ ion beam (Fig. 2.10(g)). Further thinning is carried out using the Ga^+ ion beam, maintaining the same accelerating voltage but with lower currents of 0.40 nA and 0.24 nA, respectively, at a tilt of $\pm 1.5^\circ$. This thinning process continues until the lamella thickness reaches approximately 700 nm (Fig. 2.10(h)). The last thinning step involves a lower ion dose of 83 pA at 30 kV with a tilt of $\pm 1.2^\circ$. After the thinning process, the lamella thickness is typically within the range of 200-400 nm.

The final polishing process is carried out utilizing a 5 kV Ga^+ ion beam with a dose rate of 16 pA. The choice of a low current during the final polishing process is based on the trade-off between improved time-efficiency and reduced surface damage. A TEM lamella prepared with two different thickness is displayed in Fig. 2.10(i). It should be addressed that, unlike other lamellas prepared for conventional TEM measurements, no further thinning or cleaning (e.g., cleaning with Ar plasma or nano-milling with 0.9 kV Ga^+ ion beam) is carried out to the lamella to avoid alteration of the surface condition.

(ii) As for the STEM measurements, the lamella is initially thinned down to 170 nm using 30 kV Ga^+ ion beam, with a progressively decreasing current ranging from 0.40 nA to 83 pA. Following this step, an additional thinning stage is carried out at 16 kV with an ion dose of 50 pA to further reduce the thickness to the lower 100 nm range while minimizing damage to the lamellas. At the final polishing stage, a 5 kV accelerating voltage with an ion dose of 15 pA is used, with the lamellas oriented $\pm 5^\circ$ relative to the incoming Ga^+ ion beam.

Following the FIB-milling process, further thinning and cleaning of lamella surface is accomplished with the NanoMill TEM sample preparation system (model 1040, Fischione Instruments). The milling voltage is set at 0.9 kV, the lamella is tilted at $+10^\circ$ and -8° with respect to the incoming Ga^+ ion beam. The total milling duration at each angle is approximately 20 minutes. Before each session of STEM measurement, the lamella is cleaned with for 5-7 minutes utilizing Ar gas inside a plasma cleaner (model 1020, Fischione Instruments).

2.2.2 Lamella crystalline thickness determination

Convergent electron beam diffraction CBED measurement is carried out to determine the thickness of crystalline core of FIB-prepared lamellas.[63] The CBED experiments are accomplished with the TEM (model FEI Tecnai G2 F20).[65] Practical experimental considerations involve the control of electron dose as well as ensuring precise two-beam conditions. Due to the fact that the electron beam is highly focused to provide a proper convergent angle in CBED measurement, controlling beam intensity is critical to prevent damage to the lamella as well as the camera. In the actual experimental setup, intensity weakening is accomplished by utilizing a condenser aperture (c2) with a smaller radius (e.g., 70 μm) in conjunction with a larger spot size of the incoming electron beam.

Furthermore, the precise two-beam condition is established as follows: Using GaN lamella as an example, first, the lamella is tilted along the $[0002]$ Kikuchi band until only (0000) and (0002) reflections are strongly excited. Next, to enhance the number of Kossel-Moellenstedt fringes, the lamella is further tilted along the $[1\bar{2}10]$ direction so that another reflection (e.g., (0004) or (0006)) is excited and at the two-beam condition. The resulting CBED disks are recorded with a camera (model UltraScan 1000P, a $2\text{K}\times 2\text{K}$ charge-coupled digital camera). The exposure time is set at 1 s as a compromise between enhanced fringe contrast and a safe dose to the camera. The crystalline thickness of lamella is derived using the graphic method (see Eq. (2.12)).

The simulation of CBED patterns is accomplished with the software Dr.Probe based on multislice calculation.[66] The parameters of microscope are set to be close to those used during actual experiment: The electron source exhibits a size of 0.04 nm and the electron beam undergoes an acceleration voltage of 300 kV. The semi-convergence angle of the probe is configured as 5 mrad due to the parallel illumination. The maximum collection angle of the detector is 100 mrad.

2.2.3 Electron holography

Conventional electron holography

Off-axis electron holography experiments are carried out with an image-corrected electron holography TEM (FEI Titan G2 60-300 HOLO, FEI instrument) operated at 300 kV.[67] During the experiment, the upper biprism is biased at 100-120 V as a trade-off between a relative large field-of-view (FOV) and a high contrast of the interference patterns. To enhance the coherence of the incoming electrons, the beam is adjusted to an elliptical shape.[68] This elliptical illumination is achieved by adjusting the stigmator on the condenser lens such that the minor axis of the ellipse is parallel to the biprism. As a rule of thumb, an ideal experimental condition is manifested when the interference patterns exhibit a contrast in the vacuum of at least 40%. To minimize the contrast from the dynamical diffraction, the lamella is tilted away from the $[10\bar{1}0]$ zone axis. A vacuum region is always present adjacent to the lamella in the FOV to generate the unperturbed reference wave.

Holograms are acquired using a $4K \times 4K$ direct electron detector (model K2 summit, Gatan). The single-frame image acquisition is achieved with a total exposure time of 8-12 s. The stack image is acquired with 20-25 frames of single-frame images, each undergoing an exposure time of 1-2 s. After the acquisition of each object hologram, a reference hologram is obtained in the nearby vacuum by the same lens settings with the lamella moving away. The reconstruction of holograms is accomplished with the plugin Holowerks in the Digital Micrograph software.

Tilt series

In this thesis, the purpose of performing the tilt series experiment is to establish an orientation with suppressed influence of dynamic diffraction. The precision of tilt series results relies on the establishment of accurate control of the tilt angles. To achieve this, the crystallographic axis of the lamella has to be oriented exactly parallel to the corresponding tilt axis of the holder. A picture of the front part of

the conventional double-tilt holder (model FEI instrument) along with the installed grid is shown in Fig. 2.11. The tilt of the holder is enabled about the alpha (a) and beta (b) axis, illustrated as the horizontal and vertical black dotted lines in the figure, respectively. An enlarged sketch of the TEM grid with the attached lamella (blue rectangle) is displayed on the right. Therefore, to establish the precise tilt control for the lamella, the two major crystallographic axes $[0001]$ and $[1\bar{2}10]$ need to be in parallel with the holder tilt axis a and b , respectively.

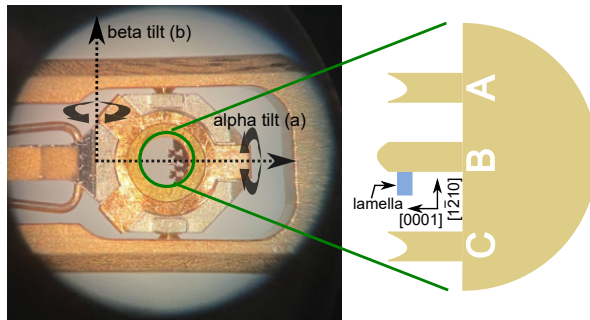


Figure 2.11: The front part of the double-tilt holder with a sketch of the installed TEM grid. The holder can tilt around axis alpha (a) and beta (b) (black dotted lines). On the right the attachment of the lamella (blue rectangle) to the grid is sketched. The precise tilt of the lamella can only be achieved when the crystal axes $[0001]$ and $[1\bar{2}10]$ are parallel to the holders' tilt axes a and b , respectively.

During the experiment, the tilt angles are calibrated to 0° when the lamella's $[10\bar{1}0]$ zone axis is oriented parallel to the electron beam. The a tilt angles vary from 3.8° to 9.8° , in steps of 1° . The orientation of the lamella is further corroborated with the comparison between experimental CBED patterns and simulated ones.

In-situ annealing experiment

For the in-situ annealing experiment, a double-tilt heating holder (model 652, Gatan) is used. A picture of the holder mounted on the support stage is displayed in Fig. 2.12. The resistive heating of the TEM grid is achieved through a furnace. The power supply and temperature control is accomplished with a hot stage power supply unit (model 628, Gatan). This control unit provides an advantage of fast temperature ramping.

The enlarged high-temperature part of the heating holder is shown in Fig. 2.13. The TEM grid is positioned in direct contact with the furnace for a better heat-

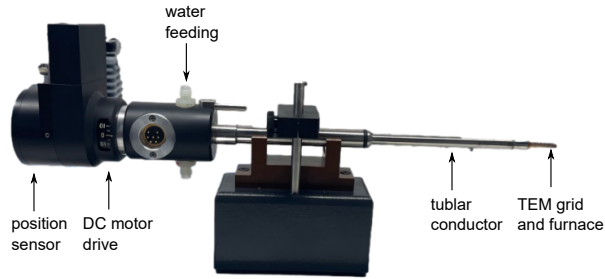


Figure 2.12: Double-tilt heating holder (Gatan Model 652) used for in-situ annealing electron holographic experiment. Some important components are highlighted.

ing efficiency. The resistive heating of the furnace is enabled via two electrodes. The furnace is made of the made of refractory metal tantalum, providing high-temperature strength and resistance to welding to most solid-state materials.

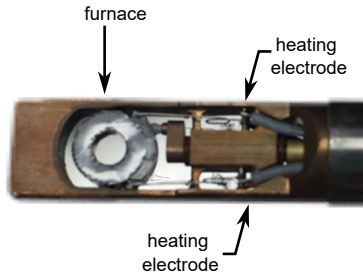


Figure 2.13: The high-temperature part of the Gatan Model 652 double-tilt heating holder. The resistive heating is achieved via two electrodes.

In the course of in-situ annealing experiment, some practical considerations need to be taken into account: First, the temperature of the lamella is measured using a platinum thermocouple, which is welded in direct contact with the furnace body. Therefore, the indicated temperature is that of the furnace rather than the lamella. In practice, the actual temperature of the lamella can be anticipated to be lower than that of the furnace due to the heat drain to crossheads and the reduced thermal conductivity between the lamella and the TEM grid, as well as between the TEM grid and the furnace.

Second, it has been consistently observed that the biprism biased at a high voltage (V_{bip}) is more susceptible to the instability arising from elevated temperatures.

Therefore, as a trade-off between a desired FOV, a high fringe contrast, and the stability of the instrument, a V_{bip} of 70 V is applied. Nevertheless, even under an optimized V_{bip} , the thermal-induced instability can still be clearly observed as the reduced fringe contrast. Figure 2.14(a) and (b) compares the holograms acquired in vacuum at room temperature and elevated temperature (i.e., 490 °C), respectively. In Fig. 2.14(a), a fringe contrast of 44.04% is found. In contrast, the fringes in Fig. 2.14(b) are visibly more noisier, and a reduced fringe contrast of 22.61% is derived.

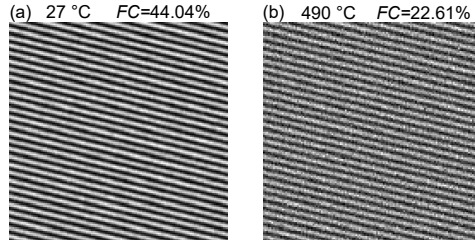


Figure 2.14: Holograms acquired in vacuum at 490 °C (a) and 27 °C (b) under an optimized V_{bip} of 70 V. The fringe contrast for holograms acquired at 27 °C and 490 °C is found to be 44.04% and 22.61%, respectively.

Third, the thermal-induced lattice expansion needs to be addressed. Due to this reason, the diffraction condition may vary at different temperatures, which, in turn, gives rise to different dynamic diffraction contrast. In order to suppress the contrast arising from dynamic diffraction, the lamella is tilted within a range of $\pm 1^\circ$ about the a tilt axis at different temperatures.

Next, I turn to the temperature profiles applied in the in-situ annealing experiment. A plot of the annealing temperatures against time is illustrated in Fig. 2.15. Two annealing cycles with an identical temperature profile are carried out. The only difference between them is that the second annealing cycle (red lines) is conducted 11 hours later after the completion of first cycle (black lines). It should be addressed that during this discontinuation between two annealing cycles, the lamella is kept inside the microscope chamber under room temperature and the TEM gun valve is closed. In both cycles, the temperature rises gradually from room temperature (27 °C) to the maximum 490 °C at a step of 50 °C and then abruptly go back to room temperature. Each temperature is held constant for 30 minutes to ensure that the lamella is sufficiently heated and the microscope recovers to a stable condition. After the stabilization of the microscope, a hologram free from dynamic diffraction contrast is acquired under the identical optic settings among all temperatures.

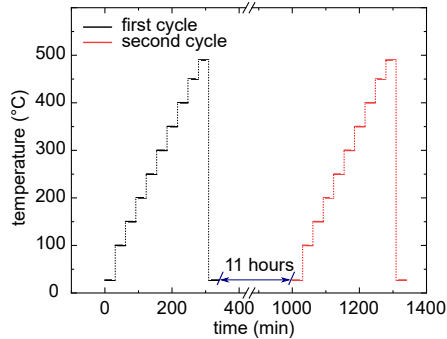


Figure 2.15: Annealing temperature versus time profile for the in-situ annealing experiment. The single-cycle annealing experiment ends after the first cycle (black lines), whereas the two-cycle annealing experiment continues until the end of the second cycle (red lines). The time discontinuation between the first and second annealing cycle is about 11 hours. In both cycles, the temperature gradually rises from 27°C to 490°C at a step of 50°C. 30 minutes of holding time has been applied on each temperature point in order to reach the sufficient annealing of lamella and stable microscope conditions.

2.2.4 STEM and EDX: Strain and chemical composition measurement

The STEM measurements are carried out with a (spherical) aberration-corrected microscope FEI Titan G2 80-200 CREWLEY operated at 200 kV.[69] A HAADF detector is used to collect electrons scattered at an angular range of 70-250 mrad. A 70 μm diameter condenser aperture (c2) is selected to form a probe with a convergence angle of 24.7 mrad on the sample plane. The lamella is oriented in a manner such that the incoming electron beam is exactly parallel with the $[10\bar{1}0]$ axis. Image stacks are recorded with a size of 20 frames, each with a size of 2048×2048 pixels. A dwell time of 200 ns is applied on each pixel. The auto drift correction is enabled to reduce the influence of sample drift and scan distortions. The crystal axis of the investigated lattice constant is kept in parallel with the raster-scan direction to minimize the scan distortion and the fly-back error.[70] After the acquisition, each stack is drift-corrected frame integration (DFCI), averaged, and aligned using the Velox software.

Utilizing the EDX detector installed on the same microscope, the chemical element maps are acquired on 2048×2048 pixels HAADF image. For a medium FOV of $1 \times 1 \mu\text{m}$, the collection of X-ray lasts 20 minutes. The analysis of the EDX results

is accomplished with the Velox software.

The strain is determined with two methods: The first method relies on analyzing lattice constants in real space.[71, 72] The central positions of intensity peaks in HAADF images, representing the atomic columns, are determined from atomic-resolved HAADF images with a field of view of less than 12×12 nm using the peak pair analysis (PPA) algorithm.[73] The distance between each position corresponds to half of the lattice constant. For the calibration, the lattice constant measured at the substrate are considered as the unstrained reference.

The second method is based on analyzing the spacing between diffraction reflections in reciprocal space. This is achieved with HAADF images acquired at a larger field of view of 46×46 nm. The distances between lattice fringes in real space are reflected as spacings between diffraction reflections in reciprocal space. This method uses the geometric phase analysis (GPA) algorithm,[74] implemented with the FRWtool plugin in Digital Micrograph software.[75] As recommended in literature,[76] a mask with size of 0.5 nm^{-1} is applied on the diffraction reflection (0002) and (1210) in the reciprocal space for the strain analysis.

2.3 Sample description

2.3.1 A3162

The investigated A3162 GaN/(Al,In)N/GaN heterostructure was grown by metalorganic vapor phase epitaxy (MOVPE) at 740°C on a *c*-plane freestanding GaN Sumitomo substrate. The sample is composed of five pairs of 31 nm (Al,In)N and 105 nm GaN (Si doped $8 \times 10^{17} \text{ cm}^{-3}$) layers, which are deposited on a 560 nm GaN buffer layer (Si: $3 \times 10^{18} \text{ cm}^{-3}$). Starting from the one close to the substrate, the five pairs of (Al,In)N/GaN are labelled as (Al,In)N/GaN #1-#5, respectively. The heterostructure is capped by a $1 \mu\text{m}$ GaN layer (Si: $3.5 \times 10^{18} \text{ cm}^{-3}$). Note that the GaN cap and adjacent GaN interlayer is called "doping step" structure throughout this thesis. Within the ternary (Al,In)N layers, an indium composition of $19.15 \pm 0.5\%$ was determined by high resolution x-ray diffraction (HRXRD) measurements.[77] A sketch of the sample structure is illustrated in Fig.2.16(a), the growth direction [0001] points from right to left.

In Fig.2.16(b), the silicon concentration profiles throughout sample measured by secondary ion mass spectrometry (SIMS) is displayed. The nominal donor concentration (N_d) $3 \times 10^{18} \text{ cm}^{-3}$ of buffer layer is applied for the calibration of the Si profile. The calibrated donor concentration of GaN cap and interlayers are determined

as $3.5 \times 10^{18} \text{ cm}^{-3}$ and $7.7 \times 10^{17} \text{ cm}^{-3}$, respectively. It's not possible to precisely determine the donor concentrations for unintentional doped (Al,In)N layers with SIMS.[78] Hence, it is assumed they are at the same doping level as adjacent GaN layers.

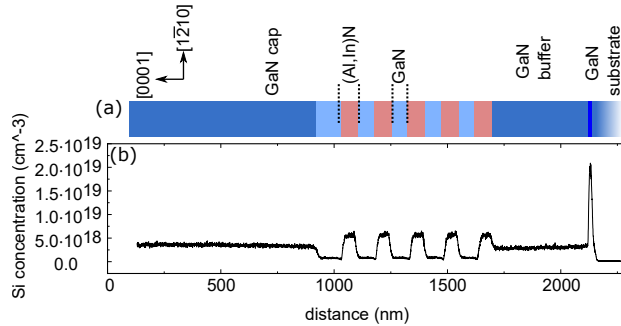


Figure 2.16: (a) Sketch of sample A3162 which composes of five pairs of 31 nm (Al,In)N and 105 nm GaN (Si doped $8 \times 10^{17} \text{ cm}^{-3}$) layers that are deposited on a 560 nm GaN buffer layer (Si: $3 \times 10^{18} \text{ cm}^{-3}$). The heterostructure is capped by a 1 μm GaN (Si: $3.5 \times 10^{18} \text{ cm}^{-3}$). Within the (Al,In)N layers an indium composition of $19.15 \pm 0.5\%$ was determined by high resolution x-ray diffraction measurements. (b) Si concentration profile through out sample measured by SIMS. Doping concentrations are calibrated by the Si intensity measured on buffer layer.

2.3.2 A3777

Sample A3777 comprises a 700 nm thick GaN layer grown by metal organic vapor phase epitaxy (MOVPE) on top of a *c*-plane free-standing hydride vapor phase epitaxy (HVPE)-grown GaN substrate (Fig. 2.17). The MOVPE-grown GaN epilayer exhibits a Si doping of $5 \times 10^{19} \text{ cm}^{-3}$ in the first 20 nm (δ -doped like layer) followed by $3 \times 10^{18} \text{ cm}^{-3}$ in the remaining layer.[35] No dislocations or stacking faults were detected and scanning tunneling spectroscopy is in agreement with thermally activated Si dopants without compensating defects.[79, 80]

Tab.2.1 and Tab.2.2 summarize the thickness of TEM lamellas extracted from sample A3162 and A3777 along with their corresponding labellings, respectively. The values denoted with a * symbol indicate that the thicknesses are measured solely using SEM, hence represent the overall lamella thickness. The values without * symbol indicate the crystalline thickness, as measured from CBED.

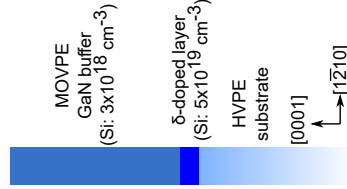


Figure 2.17: A sketch of 700 nm thick GaN layer grown by metal organic vapor phase epitaxy (MOVPE) on top of a *c*-plane free-standing GaN substrate. The epitaxial layer exhibits a Si doping of $5 \times 10^{19} \text{ cm}^{-3}$ in the first 20 nm (δ -doped like layer), followed by $3 \times 10^{18} \text{ cm}^{-3}$ in the remaining layer.

chapter	lamella thickness (nm)
4	350*
5	188±6(L1),220±7(L2),243±8(L3),257±6(L4),262±10(L5),280*(L6), 292±8(L7),320±7(L8),325±7(L9),331±6(L10),343±8(L11),348±4(L12), 353±8(L13),380*(L14)
6	339±8(B1),353±12(B2),300*(C1),330*(C2)
7	362±5(360 °C),344±6(390 °C),341±5(420 °C),361±8(450 °C)
8	188±6(electron holography), 70-120*(STEM and EDX)

Table 2.1: Thickness information of lamellas extracted from sample A3162. The value denoted with (without) * symbol indicates the overall thickness measured from SEM (crystalline thickness measured from CBED).

chapter	lamella thickness (nm)
6	278±2(A1),363±6(A2)

Table 2.2: Thickness information of lamellas extracted from sample A3777.

Chapter 3

FIB damage and its implication for quantification of electron holographic results

3.1 FIB damage types and sub-layers

It has been approximately three decades since off-axis electron holography technique was applied to map the electrostatic potential within semiconductor.[81, 82] In the early stage, the lamella preparation was typically accomplished through mechanical polishing.[81] However, this preparation method led to limited precision in achieving uniform lamella thickness, which further posed challenges in the quantitative interpretation of electron holographic results. Later, FIB was introduced as the primary TEM lamella preparation technique due to its advantages of time-efficiency and providing precise control over the thickness and flatness of the semiconductor lamella.[83] Despite the improved control over lamella thickness, however, sputtering of semiconductor by highly energetic particles inevitably brings damages to the near surface region of lamella.[84, 85, 61, 86, 87, 88]

FIB damage can manifest in primarily two forms on lamellas: First, a structurally damaged amorphous outer shell can develop on the surface of the lamella. The thickness of this layer is influenced by a few factors, including the type of milling ions, the accelerating voltage as well as the dose rate.[86, 87] Second, below the amorphous outer shell, a structure-intact but defect-rich crystalline inner shell arises due to high concentration of implanted point defects.[88, 35, 89, 90] Figure 3.1 illustrates the structure of the FIB-prepared lamella and the corresponding terminology of damaged sub-layers.

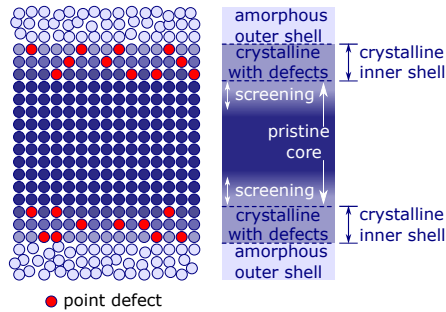


Figure 3.1: The FIB-induced pristine crystalline core, defect-rich crystalline inner shell, and amorphous outer shell structure. The FIB-implanted point defects are represented with red spheres.

Note that in previous studies, there has been a lack of consistent languages for the terminology of these FIB-induced sub-layers. The defect-rich crystalline inner shell along with the resulting screening region are treated as one single layer and named as "dead layer" or "inactive layer" etc.[91, 92, 89, 93, 90, 34] In this thesis, the FIB-induced sub-layers are unambiguously defined as the pristine crystalline core, the defect-rich crystalline inner shell, and the amorphous outer shell.

3.1.1 Amorphous outer shell

To begin with, the properties of amorphous outer shell will be examined. The electronic influence arising from the amorphous outer shell has been comprehensively studied from both theoretical perspectives and experimental findings.[84, 94, 92, 93] For semiconductors, this outer shell is anticipated to exhibit metal-like properties, establishing a charge flow circuit on the lamella surface, hence effectively screening the surface potential into the vacuum. This is supported by the absence of fringing fields in the vacuum near the lamella during experiments.

The metal-like properties stem from the fact that a multitude of diverse bonding structures concerning length, angle, involved species is formed in the amorphous outer shell. This variety of bonding states gives rise to a broad distribution of density of states, gradually closing the bandgap (known as Urbach tails).[95] At the interface between the amorphous outer shell and crystalline semiconductor, in conjunction with a high diversity of point defects, this results in a wide density of states distribution throughout the bandgap, with the charge neutrality level located in the center. This fact is known to induce a Fermi-level pinning at the midgap

position.[96] The existence of midgap pinning in the vicinity of amorphous adatom clusters is further substantiated by the scanning tunneling microscopy (STM) measurements on III-nitride surfaces.[97] It is important to note that for the as FIB-prepared lamella, the pinning arising from the amorphous outer shell cannot directly affect the pristine crystalline core due to the presence of the crystalline inner shell in between (see Fig. 3.1). However, if the pinning from the inner shell is removed, the amorphous shell is expected to provide the subsequent pinning. This can take place, for instance, when the point defects within the defect-rich crystalline inner shell are electrically passivized or fully healed.

The thickness of the amorphous outer shell can be accurately determined by subtracting the overall lamella thickness measured from the SEM by the crystalline thickness determined from the convergent beam electron diffraction (CBED) technique. The thickness of the amorphous outer shell is commonly found to be in the range of a few to a dozen nanometers for III-nitride semiconductor systems,[35, 34, 90, 33] depending on the milling voltage and the hardness of the semiconductor.

3.1.2 Defect-rich crystalline inner shell

The characteristics of the defect-rich crystalline inner shell exhibit a significant correlation with the type and concentration of the implanted point defects. To the first order approximation, the implantation profile of point defect can be considered to directly associate to the stopping power (s) and the stopping cross-section (ϵ_s). The former is a fundamental parameter defined as the rate of energy loss of the incident ion per unit length while it travels within the host material.[98, 99] The stopping cross-section (ϵ_s) evaluates the average energy loss of the incident ion per recoiling event in each atomic monolayer (ML).[98, 100] Utilizing these two parameters, one could estimate after travelling how many monolayers an ion would fully dissipated its kinetic energy to the surrounding host atoms.

Implantation of point defects and impurities

The stopping and range of ions in matter/transport of ions in matter (SRIM/TRIM) software can be used to compute numerically the stopping power and cross-section of a specific ion's implantation in semiconductor materials. This software allows for an invaluable understanding of the two critical parameters characterizing FIB-induced point defects: The type of created point defect and the ion's implantation profile.[101]

Here, as a demonstration, the SRIM/TRIM calculation is carried out for GaN. Due to the fact that the thickness of lamella is slightly reduced only in the final polishing step during FIB process, it can be assumed that the implantation of point defects primarily takes place during this specific step. In addition to the type of host material, the most critical simulation parameters include the acceleration voltage of the incoming ion and its incidence angle. During the final polishing, the Ga^+ ion, exhibiting a dose of 16 pA, is accelerated at 5 kV and enters the host material at an incidence angle of 5° (i.e., 85° relative to the surface normal).

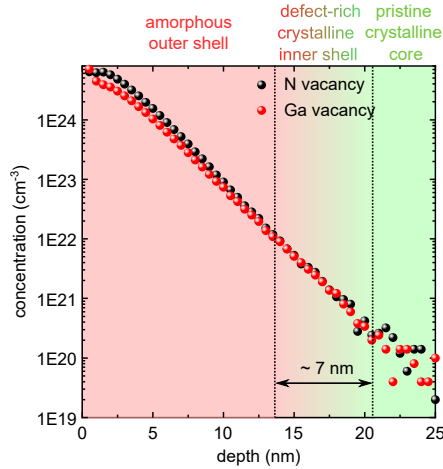


Figure 3.2: Simulated implantation profile for Ga and N vacancy in GaN. The simulation parameters are taken as the final polishing step during FIB: The Ga^+ (with a dose of 16 pA) is accelerated at 5 kV and enters the host material at 5° . This simulation is performed with the SRIM/TRIM software.[101]

Figure 3.2 illustrates the exemplary FIB-induced implantation profiles of N (black sphere) and Ga vacancies (red sphere) in GaN, as calculated from SRIM/TRIM software: The amorphous outer shell (depicted in red background) is anticipated to form if the concentration of vacancies is higher to that of Ga/N atoms (specifically, $1 \times 10^{22} \text{ cm}^{-3}$). In this case, the amorphous outer shell exhibits a thickness of $\sim 13 \text{ nm}$. In the pristine crystalline core (depicted in green background), on the other hand, the concentration of the vacancies is expected to be about two orders of magnitude lower than that of Ga/N atoms. Within this framework, the defect-rich crystalline inner shell (region depicted in color gradient) is a transition region between the amorphous outer shell and the pristine core, exhibiting a thickness of $\sim 7 \text{ nm}$.

Types of point defects in GaN

At this stage, various types of point defects and impurities potentially present in GaN will be introduced. Native point defects in GaN includes, i.e. Ga vacancy (V_{Ga}), N vacancy (V_{N}), N interstitial (N_{i}), Ga interstitial (Ga_{i}), N antisite (N_{Ga}), and Ga antisite (Ga_{N}).^[102] Extrinsic impurities, for instance carbon, which serves as the chemical source for the protective layer, can be unintentionally implanted in GaN during the FIB process.

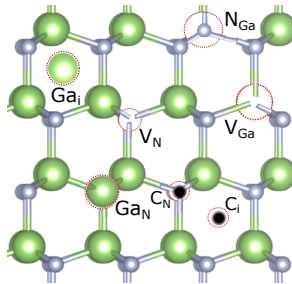


Figure 3.3: A schematic illustration of vacancies, interstitials and antisites native defects along with carbon impurities in wurtzite GaN. The green, grey, and black spheres stand for gallium, nitrogen, and carbon atom, respectively.

Fig. 3.3 depicts the different types of point defects in GaN. The GaN crystal is oriented slightly away from the $[1\bar{2}10]$ zone axis for a better visibility. The big green spheres, small grey, and small black spheres represent gallium, nitrogen, and carbon atoms, respectively.

Diffusion of point defects

Diffusion of point defects is considered as a thermally activated process in which the concentration gradient within the crystal tends to decrease.^[103] The diffusion of point defect can be achieved via several paths in GaN.^[104, 105] For example, in case of a N vacancy, two types of atomic migration paths are expected due to crystallographic symmetry considerations (see Fig. 3.4). The nitrogen and gallium atoms are represented with small grey and large green spheres, respectively. The vacancy on nitrogen lattice site is circled in black dotted line. Energy favorable paths for the vacancy to diffuse are denoted as A and B. Path A describes the migration of the vacancy, specifically, the movement of one of the first nearest neighboring (NN) nitrogen atoms that are located in the same plane perpendicular

to the [0001] axis, jumping into the vacancy position. In contrast, for migration path B, the migration occurs through a lattice site exchange between the vacancy and an out-of-plane nitrogen atom. A third potential path C (not shown here) involves the migration with a second nearest neighbor out-of-plane nitrogen atom by utilizing the hexagonal channel. However, such a path is commonly energetic unfavorable.[105]

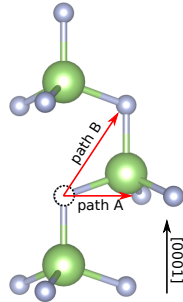


Figure 3.4: Possible migration paths of a nitrogen vacancy in the wurtzite structure GaN. Nitrogen and gallium atoms are depicted as small grey and large green spheres, respectively. The vacancy in the nitrogen lattice site is marked by black dotted line. Migration path A describes the migration process between vacancy and a first nearest neighboring in-plane nitrogen atom. Another migration path B involves the vacancy and a first nearest neighboring out-of-plane nitrogen atom.

Next, I turn to derive the some important parameters characterizing the diffusion of point defects. By adopting the harmonic transition state theory, the jump rate Γ of a single atom is described as:[105]

$$\Gamma_i = \Gamma_{0,i} e^{-\frac{\Delta G_i}{k_B T}} \quad (3.1)$$

where i denotes a migration path. The prefactor $\Gamma_{0,i}$ is the attempt frequency, ΔG_i is the Gibbs free energy of migration, k_B is the Boltzmann constant, and T is the temperature. $\Gamma_{0,i}$ is calculated within harmonic transition state theory .[106] For the sake of simplicity, this prefactor is approximated by a characteristic frequency, such as Einstein and Debye frequency.[107] A reasonable approximation of $\Gamma_{0,i}$ can then be taken as a typical phonon frequency, i.e., 10^{13} s^{-1} . The free Gibbs free energy of migration ΔG_i is expressed by:

$$\Delta G_i = \Delta H_i + p\Delta V_i - T\Delta S_i \quad (3.2)$$

where ΔH_i denotes the enthalpy of migration, ΔV_i is the migration volume, and

ΔS_i is the migration entropy. For the system studied in this thesis (i.e., TEM under high vacuum), term $p\Delta V_i$ is estimated to be zero. The migration entropy is usually in the range of 1 to $2k_B$, hence the term $T\Delta S_i$ has a minor contribution to the Gibbs free energy and can be disregarded.[107] Only the enthalpy term ΔH_i is required for the calculations of jump rate of point defects. In most of cases, the term ΔH_i is approximated as migration barrier energy E_b which is defined as the minimum energy an atom has to overcome on its reaction path to an adjacent site.[104]

Figure 7.4 illustrates the migration of nitrogen vacancy to an out-of-plan nitrogen lattice site. The nitrogen vacancy is represented by a red sphere. For such a process, the migration barrier is 4.3 eV.[104] It's worth mentioning that Eq. (3.1) has often been applied for the estimation of annealing temperatures at which a certain type of point defect becomes mobile. At such a temperature, the jump rate of defect is approximated as $\Gamma = 1 \text{ s}^{-1}$.

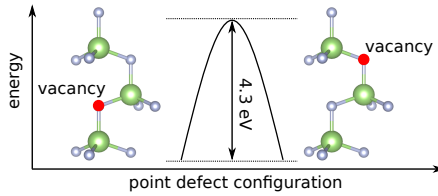


Figure 3.5: The migration barrier of a V_N (marked with the red sphere) to exchange position with an out-of-plane nitrogen atom. The diffusion barrier is 4.3 eV.[104]

With the knowledge of migration barrier energy E_b (hence the jump rate Γ) and migration paths, the diffusion coefficient D is derived as:

$$D = 0.5 \sum_i \xi_i \Gamma_i |\bar{\lambda}_i|^2 \quad (3.3)$$

where ξ_i is the factor accounting for the multiplicity of equivalent migration paths, $\bar{\lambda}_i$ is the displacement length of jump. Note that the diffusion coefficient D is dependent on a few parameters, including temperature, attempt frequency, and crystallographic structure etc.

Theoretical computations of migration barrier energy for various types of native point defects in wurtzite GaN have been performed by Limpijumnong *et al.* and Kyrtzos *et al.*[104, 105] The work of Limpijumnong is based on first-principle DFT calculations, whereas Kyrtzos employs DFT in conjunction with the climbing image

nudged elastic band method as well as the dimer method. Their results are summarized in Tab. 3.1. In general, defect type with low barrier, e.g., gallium interstitials and gallium vacancies, could easily diffuse at room temperature.[104] In contrast, defects with higher barrier are more likely to remain unless a high annealing temperature is reached. Note that the results from two authors are comparable, except for the values of Ga_i^{1+} and V_N^{1+} .

Defect	Charge state	Barrier (eV)[104]	Barrier (eV)[105]
Ga_i	+3	0.9	0.7
	+2	≤ 0.9	1.1
	+1	≤ 0.9	1.6
N_i	+3	1.4	1.7
	+2	2.5	2.1
	+1	2.1	2.1
	0	2.4	2.4
	+1	1.6	1.9
V_N	+3	2.6	2.7
	+1	4.3	2.9
V_{Ga}	-3	1.9	2.1

Table 3.1: Migration barriers for native point defects in wurtzite GaN.[104, 105]

At this stage, it is necessary to examine the migration barrier energy of extrinsic impurities in wurtzite GaN. The particular focus is on carbon, given its role as the protective layer during the FIB process. Utilizing DFT with the climbing image nudged elastic band method, Kyrtsos *et al.* investigates diffusion paths of carbon interstitials (C_i) with different charge states in *n*-type GaN.[105]

Depending on the relative positions between the nitrogen and carbon atoms, three types of C_i are distinguished, labelled as s_1 , s_2 , and s_3 , as displayed in Fig. 3.6. The carbon and nitrogen atoms are depicted as black and grey spheres, respectively. Ga atoms are illustrated as green spheres. The diffusion of C_i is accomplished either through switch between different types of split interstitial within a unit cell, or through jumping of one type of split interstitial to an equivalent position in another unit cell. Table 3.2 summarizes the migration barrier energies of carbon interstitials. The findings indicate that E_b of C_i falls into a range from 1.6 eV to 4.4 eV, depending on the charge states, initial/final configuration of C_i split interstitial, and migration path. In particular, the highest migration barrier energy is found in the +1 charge state associated with s_1/s_1 migration within hexagonal channel, whereas the lowest value is observed in the +2 charge state associated to the in-plane migration.

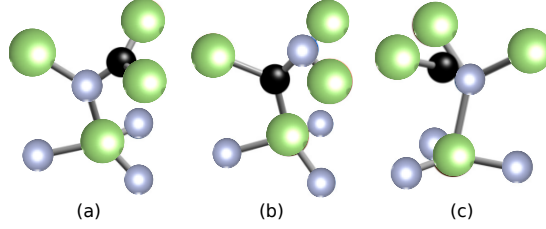


Figure 3.6: Three types of split interstitials between carbon atom (black sphere) and nitrogen atom (grey sphere). Ga atoms are illustrated as spheres in green color. Type (a), (b), and (c) are named as split s_1 , s_2 , and s_3 , respectively. Adapted from literature.[105]

migration path	initial /final	barrier (eV) $q=-1$	barrier (eV) $q=0$	barrier (eV) $q=+1$	barrier (eV) $q=+2$
A: First NN out-of-plane	s_i/s_i		2.5	2.6	2.0
	s_j/s_j	2.9	2.6	2.6	2.0
	s_i/s_j	2.9	2.3	2.6	2.0
B: First NN in [0001] plane	s_i/s_i	2.8	2.5	2.4	1.8
	s_j/s_j	3	3	2.6	1.6
	s_i/s_j	3	3	2.6	1.6
C: Second NN out-of-plane	s_i/s_i		4.0	4.4	
	s_j/s_j				
	s_i/s_j		4.0	4.3	

Table 3.2: Migration barrier energies for carbon interstitials with different charge states in wurtzite GaN.[105] A, B, and C represents the migration between out-of-plane first nearest-neighbor, in-plane first nearest-neighbor, and out-of-plane second nearest-neighbor atom jumps through hexagonal channels, respectively. In all cases except for the +2 charge state, s_i/s_j refers to s_1/s_2 . In the case of +2 charge state, s_i represents to s_3 .

Electronic properties of point defects

The possibility of the occurrence of a specific type of point defect can be assessed through its formation energy E^f , [108] which represents the amount of energy required to create the defect from a perfect crystal lattice. The detailed description of the calculation for the formation energy is beyond the scope of this thesis, here, only an introductory discussion is given following the formalism mentioned in the

literature: [109, 110, 111]

$$E^f(X^q) = E_{\text{tot}}(X^q) - E_{\text{tot}}(\text{bulk}) - \sum_i n_i \mu_i + qE_{\text{F}} + E_{\text{corr}} \quad (3.4)$$

where $E_{\text{tot}}(X^q)$ is the total energy derived from a super-cell calculation containing the defect type X with charge state q . $E_{\text{tot}}(\text{bulk})$ is the total energy of the same and perfect crystal without any defect. The integer n_i indicates the number of atoms of type i (host atoms or impurity atoms) that have been added to ($n_i > 0$) or removed from ($n_i < 0$) the super-cell to form the defect, and the μ_i are the corresponding chemical potentials of these species. Hence, $n_i \mu_i$ is the energy addition or subtraction for the system. The chemical potential for charges is represented by that of the electrons, which translates to the Fermi-level energy denoted as E_{F} . [111] E_{corr} is a correction term that accounts for finite sampling effect on shallow point defects.

In conjunction with Eq. (3.4), a few studies have utilized DFT to investigate the formation of point defects in wurtzite III-nitride binaries. [108, 112, 105, 113, 114, 115] The formation energies of native point defect and some impurities under Ga-rich condition from the literature have been summarized in the Fig. 3.7(a) and (b), respectively. The valence band edge corresponds to $E_{\text{F}}=0$ eV. The slope represents different charge states, i.e., for negative slope negatively charged and vice versa (see Eq. (3.4)). Within the bandgap, the colored symbols denote the charge transfer levels (CTL) where the charge state of a point defect changes.

It should be noted that in semiconductors, when the concentration of point defects is equal to or higher than that of dopants, the Fermi-level becomes pinned at the corresponding charge transfer level of the point defect. Assuming the concentration of point defects follows an exponential decay, the pinning is anticipated to be confined within a thin layer on the surface of the lamella.

3.2 Previous handling of FIB damaged (dead) layers

From literature, [94, 116, 91, 117, 92, 89, 93, 118, 119, 120, 90] a wide spread of handlings of FIB damaged layers can be found. In earlier studies, researchers observed that the measured phase contrast across the Si p - n junctions is always lower than the theoretical prediction. In addition, the measured value is revealed to approach theory more closely as the thickness of the lamella increases. Rau *et al.*

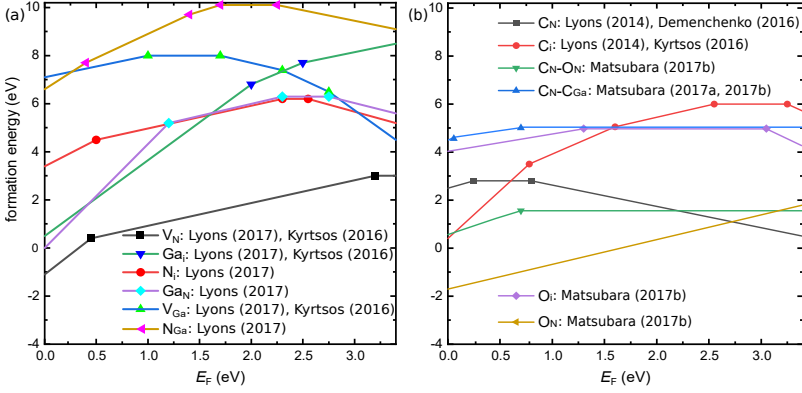


Figure 3.7: (a) Formation energies of native point defect in GaN given as a function of Fermi energy E_F under Ga-rich condition. The slope reflects the charge state, according to Eq. (3.4). The changes in the slope indicate the energy of charge transfer levels that are also marked with symbols. (b) Formation energies of extrinsic impurities in GaN. Summarized from literature.[108, 112, 105, 113, 114, 115]

were the first to propose that the formation of electrically dead layer on the lamella surface, a consequence of the FIB milling process, is at the origin of the observed discrepancy.[94] They also proposed a methodology to estimate the thickness of the dead layer: By plotting the measured phase contrast across the p - n junction on lamellas with different thickness against their respective thickness, the intercept of the linear extrapolation at the point where the phase contrast diminishes to null indicates the thickness of the dead layer t_{dead} . Based on this approximation, the electron optical phase change measured from TEM lamella (see Eq. (2.5)) is straightforwardly transformed to:

$$\Delta\phi(x, y) = C_E(V_{EP}(x, y) + V_{MIP}(x, y))(t_{\text{crystal}} - t_{\text{dead}}). \quad (3.5)$$

More recently, it was observed that for some semiconductor systems, e.g., p^+ - p [90] and n^+ - n GaN doping step,[29] the measured phase contrast is larger than expected. The enhancement in phase contrast cannot be explained by employing Eq. (3.5), as it always yields a reduced value. Therefore, attempts have been made to develop a comprehensive model that enables the elucidation of underlying physics behind the "apparent" contradictory observations concerning p - n junctions and doping structures.[120, 90, 119] Among these modellings, the one centered on surface Fermi-level pinning is recognized as a promising solution for resolving this matter.[120, 90]

Somodi *et al.* utilized a finite-element calculation to assess the effect of surface states of TEM lamella on phase contrast measured across the Si p - n junction.[120] Using an arbitrary surface Fermi-level pinning, located at 0.7 eV above the Fermi-level in the bulk, the trend of change in the measured phase contrast, as a function of lamella thickness, was reproduced. Nevertheless, due to the lack of knowledge of the surface state of actual TEM lamella, these results are rather qualitative. A similar attempt to quantify the phase map measured from FIB-prepared GaN lamella was carried out by Amichi *et al.*[90] The authors made the assumption of an arbitrary surface Fermi-level pinning at the midgap position, specifically 1.7 eV above the valence band. However, using such arbitrary surface pinning, the phase contrast across the p^+ - p GaN doping step cannot be reproduced using the dopant concentration determined from SIMS.

With the development of advanced TEM techniques and improvements in numerical computation methods, the nature of the dead layer has been experimentally investigated in greater detail:[116] Utilizing electron holography in conjunction with three-dimensional (3D) tomography technique, Wolf *et al.* probed the surface Fermi-level pinning in FIB-prepared Si and Ge p - n junctions. For the Si p - n junction (Fig. 3.8(a)), they measured an upward (downward) band bending in the n -type (p -type) layer, suggesting the pinning within the bandgap. For the Ge p - n junction (Fig. 3.8(b)), a pronounced downward bending was revealed on both p -type and n -type layers. This implies the surface Fermi-level pins at a position in close vicinity to the conduction band edge. Nevertheless, such a tomographic electron holographic measurement requires not only advanced experimental techniques, but also complicated data analysis. Furthermore, the tomographic technique can only be applied to materials with isotropic electronic properties, hence cannot be used to study semiconductors such as wurtzite III-nitrides.

The first quantitative calibration of FIB-induced surface damage on semiconductor was carried out by Wang *et al.*[35] A surface Fermi-level pinning of 0.69 ± 0.2 eV above the valence band was revealed on III-nitride lamella. This is accomplished by comparing the measured phase change profile across a doping structure with that derived from the self-consistent electrostatic potential calculation, taking the surface effects into consideration. In specific, the FIB-induced surface Fermi-level pinning is modelled by a surface state, which exhibits a Gaussian distribution of states, located at the interface between the amorphous outer shell and the crystalline semiconductor. The charge neutrality level of surface states is set to the center of the Gaussian distribution.[121] A schematic illustration of the cross-sectional view of modelled lamella is displayed in Fig. 3.9.

Some details of this approach need to be addressed: First, the physical presence

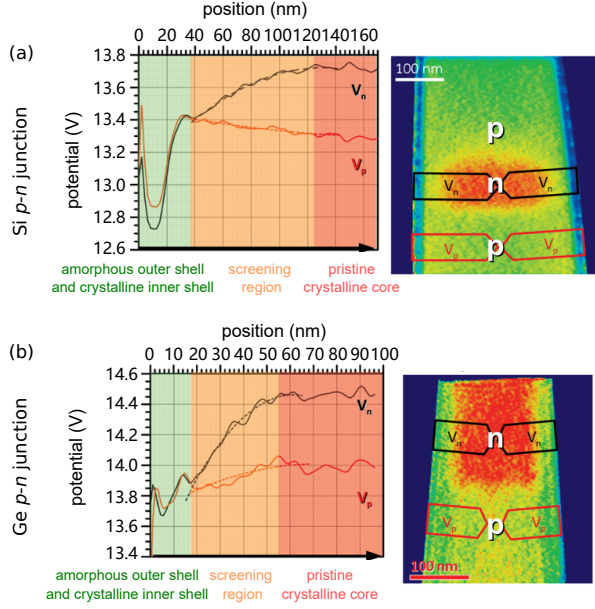


Figure 3.8: (a,b) Reconstructed 2D potentials profiles of two FIB-prepared needles, a Si needle with $p-n-p$ junction and a Ge needle with $p-n$ junction, respectively. The line profile acquired in the p and n layers are marked with red and black lines, respectively. The corresponding FIB-induced damaged layers, as well as the pristine crystalline core, are denoted. In the screening region of the Si junction, an upward and downward band bending is revealed in the p and n layers, respectively. In the Ge junction, both layers exhibit a downward band bending. Adapted from literature.[116]

of both the amorphous outer shell and defect-rich crystalline inner shell is not included, only their electronic influence is characterized by different values of surface Fermi-level pinning. Specifically, the pinning level from the defect-rich inner shell is used as a fitting parameter, whereas the amorphous outer shell is assumed to provide a midgap pinning, if the pinning from inner shell is absent. Furthermore, due to the experimental inability of distinguishing between defect-rich crystalline inner shell and the pristine crystalline core through CBED measurements, the modelled lamella is expected to be slightly thicker compared to the actual one.

Even though the numerical value of the surface Fermi-level pinning was successfully determined by Wang *et al.* There still exist some open questions: The first one is related to the reproducibility of the revealed surface pinning position. Would

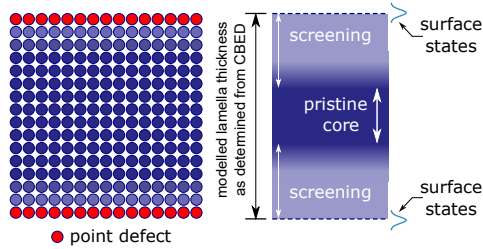


Figure 3.9: Approach to model the FIB-induced lamella structure, as adapted in this thesis. The physical presence of the amorphous outer shell and defect-rich inner shell is neglected. Their electronic influence is characterized by the Fermi-level pinning at the interface between the lamella and vacuum.

the III-nitride lamellas prepared using a same set of FIB parameters demonstrate a comparable surface condition, thereby resulting in a similar surface Fermi-level pinning? The second question is linked to the physical origin responsible for surface pinning. In particular, the inquiry focuses on identifying the type of point defect that causes the surface to be pinned at this particular position. Third, given that Wang’s experiment took place at room temperature, there is an interest in exploring the dynamics of surface Fermi-level pinning during annealing. The ultimate goal is to examine whether the damages induced by FIB can be healed through the annealing process. In this thesis, I am dedicated to answering these open questions, following Wang’s approach.

3.3 Simulation of the electron holography results

At this stage, I turn to the physical details and mathematics of the approach introduced by Wang *et al.*[35] The content of this section is structured as following: First, I examine the band bending induced by surface Fermi-level pinning. Then, the methodology for the self-consistent electrostatic potential calculation, as well as the treatment of surface Fermi-level pinning, is provided. In addition, the electronic properties of III-nitrides relevant for the calculation, along with their strain dependence, are introduced. Finally, a method for deriving the phase change map from the electrostatic potential is presented, along with a discussion on the mean inner potential.

3.3.1 Modelling of surface Fermi-level pinning: Case of III-nitride

Depending on the relative position between the surface states' charge neutrality level and the Fermi-level in the bulk semiconductor, the surface energy bands bend either upward or downward. In absence of external electric fields, this surface band bending can be qualitatively defined by the condition that the charge in the space-charge region (SCR) just compensates the net charge of the surface states so that the overall charge neutrality condition is met.[122] Note that in the context of this thesis, terms "space-charge region" and "screening region" are used in an interchangeable manner.

In the following, I discuss the different types of band bending arising from both donor- and acceptor-type surface states exemplarily for a n -type semiconductor, as shown in Fig. 3.10. Note that the same framework is applied for p -type semiconductors in analogy. The semiconductor surface is at spatial position $x=0$ nm.

In case of charged acceptor-type surface states with a charge transfer level positioned below the Fermi-level, the surface charge neutrality condition is fulfilled only if the bands bend upward and hence the majority carriers (electrons for the n -type material) are depleted in the SCR. Only ionized donors are left to compensate negatively charged surface states. Depending on the magnitude of the upward band bending (and thus depending on the energy position and density of states of the surface states), the surface of semiconductor is either depleted (Fig. 3.10(a1) and (a2)), or if the energy bands are bent upward enough that the top of the valence band lies near or above the Fermi-level,[123] the semiconductor is in an inverted state (Fig. 3.10(b1) and (b2)). An inversion layer is present if the minority carrier concentration exceeds the majority carrier concentration in SCR. Vice versa, if the donor-type surface states are charged, the surface band bends downward and majority carriers are accumulated in a SCR to compensate the positive surface states (accumulation layer in Fig. 3.10(c1) and (c2)).

Next, I turn to the quantitative description of band bending as a function of distance to the surface (i.e., x direction) and as a function of the surface potential ϕ_{surf} , following the formalism introduced by Seiwatz and Green.[124] This formalism adopts an analytical one-dimensional solution to the Poisson equation, taking into account standard parabolic band approximations for electrons and holes as well as thermal ionization of dopants. At any given point x inside the semiconductor material, the potential ϕ_x is defined as:

$$\phi_x = \frac{E_F - E_i(x)}{e} \quad (3.6)$$

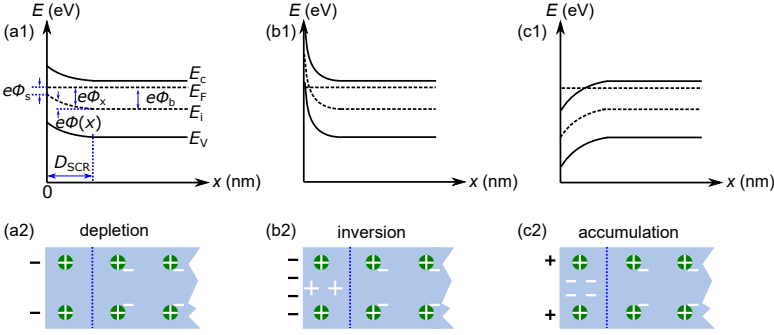


Figure 3.10: A schematic presentation of possible space-charge region types at the surface of a n -type semiconductor material. The surface is positioned at $x=0$ nm. E_C , E_F , E_i and E_V denote the conduction band minimum, Fermi-level, intrinsic level and valence band maximum, respectively. In (a1), the space-charge region width is denoted as D_{SCR} . The magnitude of band bending is derived as the difference between potential energy in bulk material and that at the surface, i.e., $e \cdot \phi_{surf} = e \cdot (\phi_b - \phi_s)$. Figure (a2) illustrates the depletion space-charge region where the band bends upward with small magnitude due to low surface states concentration, or due to the energy position of the surface states being close to the Fermi-level. Thus, majority carriers (i.e., electrons) are depleted from space charge region. Figure (b1) and (b2) represents the band diagram of a space-charge region where the bands bend upward so that the valence band edge is higher than Fermi-level at near surface region due to higher surface states concentration, or due to the energy position of the surface states being away from Fermi-level. In this case, not only electrons are expelled from the near surface region, leaving behind ionized (positively charged) donors, but also minority carriers start to accumulate in the SCR. The spatial distribution of carriers is schematically shown in (b2) where a high concentration of negatively charged acceptor-type surface states is found at the surface while positive charges accumulates at near surface region to preserve charge neutrality (i.e., inversion). (c1) depicts the condition of an electron layer at the surface due to downward band bending to compensate for the positively charged donor-type surface states, as shown in (c2).

where E_F is the Fermi energy. $E_i(x)$ is defined in such a way that the difference between E_C and E_i remains constant throughout the semiconductor, and E_i is equivalent to the intrinsic Fermi energy of the semiconductor in the deep interior of the neutral bulk. e is the elementary charge with a positive sign. Utilizing this definition of ϕ_x , the potential difference between the surface and the neutral bulk

can be defined as:

$$\phi_{\text{surf}} = \phi_{\text{b}} - \phi_{\text{s}} \quad (3.7)$$

where ϕ_{surf} is also known as the surface potential. Seiwatz and Green introduced a dimensionless quantity u to derive ϕ_{x} : [124]

$$u = u_{\text{x}} = e \cdot \frac{\phi_{\text{x}}}{k_{\text{B}}T} \quad (3.8)$$

where T is the temperature and k_{B} is the Boltzmann constant. Utilizing the dimensionless quantity u , the Poisson equation is written as:

$$\frac{d^2u}{dx^2} = -e \cdot \frac{\rho(u)}{\epsilon\epsilon_0k_{\text{B}}T} \quad (3.9)$$

where $\rho(u)$ is the total charge concentration given by:

$$\rho(u) = e \cdot (N_{\text{D}}^+ - N_{\text{A}}^- + p_0 - n_0) \quad (3.10)$$

with N_{D}^+ and N_{A}^- being the concentration of ionized donor and acceptor, respectively. n_0 is the concentration of free electrons and p_0 is the concentration of free holes. The explicit formulation of carriers concentrations and their dependence on the parameter u will be described in the following. ϵ and ϵ_0 is the semiconductor's relative permittivity and the vacuum permittivity, respectively. Note that the subscript x of parameter u is neglected for the sake of simplicity in the following. The differential equation Eq. (3.9) can be solved by multiplying the factor du/dx on both sides of the equation, followed by an integration over x . Furthermore, according to the derivation law, the second order differential term is written as:

$$\frac{du}{dx} \frac{d^2u}{dx^2} = \frac{1}{2} \frac{d(\frac{du}{dx})^2}{dx}. \quad (3.11)$$

Hence, the equation 3.9 is expressed as:

$$\frac{d(\frac{du}{dx})^2}{dx} = -2e \cdot \frac{\rho(u)}{\epsilon\epsilon_0k_{\text{B}}T} \frac{du}{dx}. \quad (3.12)$$

The differential equation can be integrated from a point x_{b} deep in the bulk material to a point x close to the surface:

$$\left(\frac{du}{dx}\right)^2|_{x_{\text{b}}} - \left(\frac{du}{dx}\right)^2|_x = -\frac{2e}{\epsilon\epsilon_0k_{\text{B}}T} \cdot \int_{u_{\text{x}}}^{u_{\text{b}}} \rho(u)du. \quad (3.13)$$

Since the electrostatic potential is regarded as constant deep inside bulk material,

the term $(\frac{du}{dx})^2|_{x_b}$ is null. Therefore, the Eq. (3.13) can be solved as:

$$\frac{du}{dx} = \pm \sqrt{\frac{2e}{\epsilon\epsilon_0 k_B T} \cdot \int_{u_x}^{u_b} \rho(u) du}. \quad (3.14)$$

Now, the electric field ϵ_x is transformed as a function with the u parameter:

$$\epsilon_x = -\frac{d\phi}{dx} = -\frac{k_B T}{e} \frac{du}{dx} = \pm \frac{k_B T}{e} \sqrt{\frac{2e}{\epsilon\epsilon_0 k_B T} \cdot \int_{u_x}^{u_b} \rho(u) du}. \quad (3.15)$$

The general expression of charge concentration $\rho(u)$ has been provided in Eq. (3.10). Here, I give the explicit definition of charge constituents in a semiconductor material. First, the concentration of free electrons (n_0) and holes (p_0) is given by:[125]

$$n_0 = N_C \frac{2}{\sqrt{\pi}} F_{\frac{1}{2}} \left(\frac{E_F - E_C}{k_B T} \right) \quad (3.16)$$

and

$$p_0 = N_V \frac{2}{\sqrt{\pi}} F_{\frac{1}{2}} \left(\frac{E_V - E_F}{k_B T} \right), \quad (3.17)$$

respectively. N_C and N_V are the effective density of states of the conduction band and valence band, respectively, which are in parabolic band approximation give by:

$$N_C = 2(2\pi m_{\text{eff,C}} \frac{k_B T}{h^{\frac{3}{2}}})^{\frac{3}{2}} \quad (3.18)$$

and

$$N_V = 2(2\pi m_{\text{eff,V}} \frac{k_B T}{h^{\frac{3}{2}}})^{\frac{3}{2}}. \quad (3.19)$$

The Fermi-Dirac integral F_j is given by:

$$F_j(\eta) = \int_0^\infty \frac{x^j}{1 + \exp(x - \eta)} dx. \quad (3.20)$$

Other contributions to the total charge concentration are the ionized donors (N_D^+) and acceptors (N_A^-):

$$N_D^+ = N_D (1 + 2\exp[\frac{E_F - E_D}{k_B T}])^{-1} \quad (3.21)$$

and

$$N_A^- = N_A (1 + 2\exp[\frac{E_A - E_F}{k_B T}])^{-1}, \quad (3.22)$$

respectively, where E_D (E_A) is the donor (acceptor) ionization energy level and N_D (N_A) is the respective dopant concentration. These four charge concentrations can each be expressed as a function of parameter u :

$$n_0(u) = \frac{2}{\sqrt{\pi}} N_C F_{\frac{1}{2}}\left(u - \frac{E_{C,\text{bulk}} - E_{i,\text{bulk}}}{k_B T}\right), \quad (3.23)$$

$$p_0(u) = \frac{2}{\sqrt{\pi}} N_V F_{\frac{1}{2}}\left(\frac{E_{V,\text{bulk}} - E_{i,\text{bulk}}}{k_B T} - u\right), \quad (3.24)$$

$$N_D^+(u) = N_D \left(1 + 2\exp\left[u - \frac{E_{D,\text{bulk}} - E_{i,\text{bulk}}}{k_B T}\right]\right)^{-1}, \quad (3.25)$$

and

$$N_A^-(u) = N_A \left(1 + 2\exp\left[\frac{E_{A,\text{bulk}} - E_{i,\text{bulk}}}{k_B T} - u\right]\right)^{-1}, \quad (3.26)$$

respectively. In these equations, $E_{D,\text{bulk}}$ ($E_{A,\text{bulk}}$) stands for the donor (acceptor) ionization energy deep inside the neutral bulk material. $E_{i,\text{bulk}}$ is the energy of bulk intrinsic Fermi-level. Inserting the Eq. (3.23)-Eq. (3.26) into Eq. (3.15), yields:

$$\begin{aligned} \varepsilon_x(u_x) = & \pm \frac{k_B T}{e} \frac{1}{\lambda_d} \cdot \left\{ \frac{N_D}{n_i} \ln \left[\frac{1 + \frac{1}{2} \exp((E_{D,\text{bulk}} - E_{i,\text{bulk}})/(k_B T) - u_x)}{1 + \frac{1}{2} \exp((E_{D,\text{bulk}} - E_{i,\text{bulk}})/(k_B T) - u_b)} \right] \right. \\ & + \frac{N_A}{n_i} \ln \left[\frac{1 + \frac{1}{2} \exp(u_x - (E_{A,\text{bulk}} - E_{i,\text{bulk}})/(k_B T))}{1 + \frac{1}{2} \exp(u_b - (E_{A,\text{bulk}} - E_{i,\text{bulk}})/(k_B T))} \right] \\ & - \frac{1}{F_{\frac{1}{2}}((E_{V,\text{bulk}} - E_{i,\text{bulk}})/(k_B T))} \cdot \left[\frac{2}{3} F_{\frac{3}{2}}((E_{V,\text{bulk}} - E_{i,\text{bulk}})/(k_B T) - u_b) - \right. \\ & \left. \left. \frac{2}{3} F_{\frac{3}{2}}((E_{V,\text{bulk}} - E_{i,\text{bulk}})/(k_B T) - u_x) \right] \right. \\ & \left. + \frac{1}{F_{\frac{1}{2}}((E_{i,\text{bulk}} - E_{C,\text{bulk}})/(k_B T))} \cdot \left[\frac{2}{3} F_{\frac{3}{2}}(u_x - (E_{C,\text{bulk}} - E_{i,\text{bulk}})/(k_B T)) - \right. \right. \\ & \left. \left. \frac{2}{3} F_{\frac{3}{2}}(u_b - (E_{C,\text{bulk}} - E_{i,\text{bulk}})/(k_B T)) \right] \right\}^{\frac{1}{2}} \end{aligned} \quad (3.27)$$

where the Debye length λ_d and the intrinsic carrier concentration n_i are given as:[124]

$$\lambda_d = \sqrt{\frac{\varepsilon \varepsilon_0 k_B T}{2e^2 n_i}} \quad (3.28)$$

and

$$n_i = N_C \frac{2}{\sqrt{\pi}} \cdot F_{\frac{1}{2}}\left(\frac{E_i - E_C}{k_B T}\right), \quad (3.29)$$

respectively. It should be noted that, with an assumption of 2D surface charge (sheet charge), the Debye length λ_d can be approximated as the width of SCR D_{SCR} , as illustrated above in Fig. 3.10. After obtaining the electric field as a function of parameter u_x , it's possible to derive the potential ϕ_x near the surface as a function distance from the semiconductor's surface x with a known surface potential:

$$\phi_x = - \int_s^x \varepsilon_{x'}(u_{x'}) dx'. \quad (3.30)$$

The difficulty in solving this integral is that value of u_x (and hence the electric field ε_x) is only known at the surface of the semiconductor, i.e., for $x'=s$. Therefore, the integral cannot be solved analytically. However, a numerical solution is obtained by applying an iterative formula give by:[126]

$$u_{x_{i+1}} = u_{x_i} - \frac{e}{k_B T} \varepsilon_{x_i}(u_{x_i}) \cdot \frac{x-s}{i_{max}}. \quad (3.31)$$

Starting at the surface where $u_s = u_{x_0}$ is known, one can iteratively determine u_x (and thus the band bending $\phi(x) = \phi_b - \phi_x = kT/e(u_b - u_x)$) at an arbitrary position x within the semiconductor.

It should be addressed that the above-mentioned one-dimensional solution is utilized as an educational estimation of the initial potential values for the three-dimensional problem. In practical applications, the surface potential is often undefined. In addition, the large divergence of the three-dimensional potential can give rise to a higher surface potential compared to the one-dimensional case.[127] Therefore, the next section will introduce a numerical method for solving the Poisson equation and continuity equations for electrons and holes within the semiconductor in three dimensions.

3.3.2 Self-consistent electrostatic potential calculation

Methodology

A self-consistent electrostatic calculation is utilized to compare electron holographic experimental results and to obtain a quantitative electrostatic potential mapping.[121] This approach ensures a rigorous and consistent analysis, enabling a reliable comparison between the experimental data and the calculated electrostatic potentials.

According to the Poisson equation, the curvature of electrostatic potential at a

given position $\phi(x, y, z)$ is expressed as:

$$\Delta\phi(x, y, z) = \frac{-e}{\epsilon\epsilon_0} \times [(p_0(x, y, z) - N_A^-) + (N_D^+ - n_0(x, y, z)) - \text{div}(\vec{P})] \quad (3.32)$$

where $p_0(x, y, z)$ and $n_0(x, y, z)$ describe the total hole and electron concentration as defined by Eq. (3.17) and (3.16), respectively. Note that the polarization \vec{P} contains the spontaneous and piezoelectric component arising from the wurtzite crystal structure of group III-nitride but does not include contributions from the permittivity *epsilon*. Hence, the electrostatic potential change is dependent on the charge distribution and change in polarization, built-in potentials, as well as surfaces states.

Next, I turn to the continuity equations for electrons and holes. Assuming a time-invariant charge distribution, the continuity equations for electrons and holes are given by:

$$\nabla \cdot \vec{J}_n - eR = 0 \quad (3.33)$$

and

$$\nabla \cdot \vec{J}_p + eR = 0, \quad (3.34)$$

respectively. eR is the generation or recombination rate. \vec{J}_n and \vec{J}_p are the current density for electrons and holes, respectively. Note that \vec{J}_n and \vec{J}_p is separated into drift and diffusion terms:[128]

$$\vec{J}_n = e \cdot (\mu_n n(x, y, z) \vec{E} + D_n \nabla n(x, y, z)) \quad (3.35)$$

and

$$\vec{J}_p = e \cdot (\mu_p p(x, y, z) \vec{E} - D_p \nabla p(x, y, z)), \quad (3.36)$$

respectively. μ_n (μ_p) is the mobility and D_n (D_p) is the diffusion coefficient of electrons (holes) in the material. Inserting Eq. (3.35) and Eq. (3.36) into Eq. (3.33) and Eq. (3.34), respectively, and utilizing the relation $\vec{E} = -\nabla\phi$, the continuity equations become

$$\nabla \cdot (D_n \cdot \nabla n(x, y, z) - \mu_n \cdot n(x, y, z) \cdot \nabla\phi) - R = 0 \quad (3.37)$$

and

$$\nabla \cdot (D_p \cdot \nabla p(x, y, z) + \mu_p \cdot p(x, y, z) \cdot \nabla\phi) - R = 0. \quad (3.38)$$

Equations (3.32), (3.37), and (3.38) comprise a system of three coupled partial differential equations that are generally unsolvable through analytical methods.[128] To perform numerical computations, it is pivot to employ appropriate discrete

equations to approximate these differential equations. In this thesis, Selberherr's discretization method, which directly substitutes the differential operators with their corresponding discrete operators, is adapted.[121]

At this stage, the modelling of surface effect needs to be addressed. The charged surface defects are treated as a two-dimensional (2D) sheet charge, i.e., it is assumed that on the material surface, the charges (originating from surface defects) distribute homogeneously on the surface and with a negligible thickness dependence. Here, a surface charge distribution σ is modelled as a Gaussian distribution with a unit of $(\frac{e}{\text{cm}^2\text{eV}})$ which is integrated from the surface charge neutrality level E_{CNL} to E_{F} , in analogy to Feenstra's treatment.[129] Furthermore, the boundary condition at the vacuum/semiconductor interface is described as the change of electric displacement vector at the interface between vacuum \vec{D}_{vacuum} and material $\vec{D}_{\text{material}}$ surface according to:

$$\vec{n} \cdot (\vec{D}_{\text{vacuum}} - \vec{D}_{\text{material}}) = \vec{n} \cdot (\epsilon_0 \vec{E}|_{\text{vacuum}} - (\epsilon\epsilon_0 \vec{E}|_{\text{material}} + \vec{P})) = \sigma \quad (3.39)$$

where the \vec{n} is the surface normal vector. Along the normal vector in x -direction, applying the relationship for isotropic media (hence isotropic polarization), which is represented as $\vec{D} = -\epsilon\epsilon_0 \cdot \nabla\phi$, this boundary condition for the electrostatic potential ϕ can be derived as:[121]

$$\vec{n} \cdot (\vec{P}_{\text{material}} - \vec{P}_{\text{vacuum}}) + \epsilon_0\epsilon \frac{\partial\phi}{\partial x}|_{\text{material}} - \epsilon_0 \frac{\partial\phi}{\partial x}|_{\text{vacuum}} - \sigma = 0. \quad (3.40)$$

Notably, this equation can be further discretized by employing difference operators.[121] This boundary condition also applies at the interface between two different semiconductor layers. In this case, the terms associated with the vacuum in Eq. (3.40) are substituted with those of another semiconductor layer. In this manner, the polarization difference at the interface between two semiconductors is treated as fixed sheet charge.

Moreover, a built-in potential V_{bi} can develop at the interface between two semiconductor layers due to the Fermi-level alignment under thermal equilibrium condition. This V_{bi} can be determined by the workfunction (Φ_{WF}) difference between both layers, with Φ_{WF} being defined as following:

$$\Phi_{\text{WF}} = \frac{E_{\text{C}} - E_{\text{F}} + \chi}{e} \quad (3.41)$$

with χ being electron affinity.

Finally, the successive over-Relaxation newton method is implemented as the nu-

merical iterative method.

Relevant parameters

At this stage, I turn to several parameters relevant to the self-consistent electrostatic potential calculation.

(i) Polarization: It is well-known that binary wurtzite III-nitrides exhibit a low-symmetry crystal structure.[130, 131] This unique crystal structure allows wurtzite nitrides to exhibit a spontaneous polarization component even without strain. Furthermore, the lattice constants of binary nitrides and their compounds differ significantly.[131] Therefore, when nitride heterostructures are grown along the [0001] polar axis, a piezoelectric polarization component can appear given the considerable lattice mismatch between layers. As a result, it can be anticipated that the functionality of nitride device will be strongly influenced by the strain (and therefore polarization) at the interface. For example, the polarization-induced high concentration of fixed charge carriers (i.e., dipoles) in high electron mobility transistor (HEMT) facilitates the high current transportation. [132, 133, 134, 135] On the other hand, in electro-optical devices, the polarization is often considered as detrimental, for instance, the efficiency of recombination process is reduced due to spatial separation of electron and holes wavefunctions (known as the Stark effect).[136, 137]

To derive the polarization in wurtzite III-nitride semiconductors, the knowledge of the polarization constants is required. These constants play a critical role in determining the magnitude and direction of the polarization in the material.[138, 139, 140, 141] Here, I examine the polarization effect following the procedure outlined by Dreyer *et al.*[140] In general, the total polarization of a wurtzite nitride layer along [0001] axis is expressed as:

$$\vec{P}_{\text{tot}} = \vec{P}_{\text{sp}} + \vec{P}_{\text{pz}} = \vec{P}_{\text{sp}} + (\varepsilon_{\text{xx}} + \varepsilon_{\text{yy}})e_{31} + \varepsilon_{\text{zz}}e_{33} \quad (3.42)$$

where the term \vec{P}_{sp} represents the spontaneous polarization. ε with different subscript stands for the strain along respective direction, e_{31} and e_{33} are the corresponding piezoelectric polarization constants. Due to mix of reference structures, the direct derivation of \vec{P}_{sp} of different materials may be problematic.[141] Thus, a better approach is to use the effective spontaneous polarization \vec{P}_{eff} where the polarization from a unstrained reference structure is subtracted from the value of investigated structure.[142] It has been suggested by Dreyer *et al.* that, by choosing

a hexagonal structure as reference, the correction is circumvented and the difference of \vec{P}_{sp} of layers is straightforwardly derived from the difference of $\vec{P}_{\text{eff}}^{(\text{H.ref})}$. [140]

Next, I turn to the piezoelectric polarization component \vec{P}_{pz} in the Eq. (3.42). The accurate calculation of the piezoelectric component relies on the precise determination of the piezoelectric constant e_{33} and e_{31} . In some studies, a so-called improper piezoelectric constant e_{31}^{imp} is utilized. [137, 143, 144] However, the calculation of e_{31}^{imp} neglects the influence of the in-plane lattice mismatch. The in-plane lattice mismatch can significantly influence the piezoelectric behavior and must be carefully considered. [145] Dreyer *et al.* implements a proper piezoelectric constant e_{31}^{prop} taking into account the strain effect. [140] Note that such a strain-dependent complication does not exist on e_{33} .

Finally, by taking these arguments into consideration, the total polarization of a wurtzite layer is derived as: [140]

$$\vec{P}_{\text{tot}} = \vec{P}_{\text{eff}}^{(\text{H.ref})} + (\varepsilon_{\text{xx}} + \varepsilon_{\text{yy}})(e_{31}^{\text{prop}} - \vec{P}_{\text{eff}}^{(\text{H.ref})}) + \varepsilon_{\text{zz}}e_{33}. \quad (3.43)$$

(ii) Bandgap energy: Another relevant parameter for the self-consistent electrostatic potential calculation is the bandgap energy E_{g} . It's well-known that E_{g} does not only depend on the chemical composition but also on the strain states and values. [146] Furthermore, for III-nitride semiconductors, the bandgap of a ternary compound A_xB_{1-x} cannot be simply interpolated from the values of its binary constituent (i.e., through Vegard's law). The non-linear effect needs to be accounted by inserting an extra bowing parameter b into the conventional linear interpolation: [147]

$$E_{\text{g}}^{A_xB_{1-x}} = xE_{\text{g}}^A + (1-x)E_{\text{g}}^B - bx(1-x) \quad (3.44)$$

with E_{g}^A and E_{g}^B being the bandgap of binary constituent A and B , respectively.

The bowing parameter b for III-nitride semiconductors varies depending on the composition. [131] For instance, (Al,Ga)N compounds exhibit a nearly constant bowing parameter with a value falling into a relatively small range between 0.8 eV to 1 eV, for a various compositions. [148, 149, 150] In contrast, for the ternary compound containing indium, a widespread of values in bowing factor is found in the literature. For example, (In,Ga)N has a large scatter of values in the range from $b=1.2$ eV to 3 eV even with only a few percentage change in indium concentration. [151, 150, 152] As for the (Al,In)N compounds, the values spread even wider: From the experimental data and theoretical calculations, the bandgap

bowing parameter changes from a low value of 2.4 eV for compound with high indium content to more than 10 eV for compound with low indium content.[131, 153, 154, 155]

For the nominal $\text{Al}_{0.81}\text{In}_{0.19}\text{N}$ layer studied in this thesis, the bowing parameter is derived based on the theoretical work by Pela *et al.*[150] They apply first-principles calculations within the density functional theory (DFT) with the LDA-1/2 approach to accurately determine the bandgap of ternary nitride alloys. Their findings suggest that for $\text{Al}_{1-x}\text{In}_x\text{N}$ layer with $x=0.15-0.19$, the bowing parameter b exhibits a composition-dependent relationship expressed as $b = 3.4 \cdot (1 - x) + 1.2$.

Next, I focus the influence of strain on E_g . Deformation or change in shape of semiconductors, can significantly impact their electronic band structure.[131] Thus, the lattice mismatch in a III-nitride heterostructure induce changes in its bandgap energy, thus affecting its optical and electronic properties.[146, 156, 131, 157, 158] To the first order approximation, strain shifts the absolute positions (i.e., relative to the vacuum energy) of the valence-band maximum (VBM) and the conduction-band minimum (CBM), resulting in a change in the bandgap energy.

The effects of strain on the band structures of III-nitrides has been computed utilizing deformation potentials.[158] These deformation potentials are a set of coefficients that describes how the band structure responds to a strain perturbation. For a quantitative study of the strain effects across the III-nitrides interface, e.g., $(\text{Al},\text{In})\text{N}/\text{GaN}$, the deformation potential of constituent binary nitride are required. However, experimentally determined deformation potentials for nitride materials can exhibit significant variation, making it challenging to rely solely on experimental values for accurate predictions. As a result, theoretical values based on bandgap-corrected first-principles approaches, which often involve hybrid functionals, are commonly adapted.[146] The values of deformation potentials of binary nitrides used in this thesis are listed below in Tab. 3.3.

Binary	$a_{cz} - D_1$ (eV)	$a_{ct} - D_2$ (eV)	D_3 (eV)	D_4 (eV)
AlN	-1.36	-12.35	9.17	-3.72
GaN	-6.07	-8.88	5.38	-2.69
InN	-3.64	-4.58	2.68	-1.78

Table 3.3: Deformation potentials of wurtzite AlN, GaN, and InN obtained from DFT with HSE functionals.[146]

In case of wurtzite materials, the derivation of E_g relies on three top-most valence band edges, which correspond to the heavy hole (HH), light hole (LH), and crystal-field split-off band (CH).[159] The corresponding transition energies from the CBM

to these bands are denoted E_A , E_B , and E_C , respectively. Assuming the biaxial strain condition, the transition energies under strain is expressed as:[146]

$$E_{A/B} = E_{A/B}(0) + \varepsilon_{zz}(a_{cz} - D_1) + 2\varepsilon_{xx}(a_{ct} - D_2) - (\varepsilon_{zz}D_3 + 2\varepsilon_{xx}D_4) \quad (3.45)$$

and

$$E_C = E_C(0) + \varepsilon_{zz}(a_{cz} - D_1) + 2\varepsilon_{xx}(a_{ct} - D_2), \quad (3.46)$$

where the $E_{A/B}(0)$ and $E_C(0)$ are the transition energies between CBM to LH/HH and to CH valence band under unstrained condition, respectively. The lowest value of these three transition energies represents the bandgap energy relevant for free charge carriers at room temperature.

The influence of hydrostatic strain on E_g has been investigated by Rinke *et al.* through DFT calculations.[157] Their results indicate that, in the strain range of ± 0.02 , the bandgap energy is considered to vary linearly with the logarithm of change in volume and a coefficient a_V , i.e., $a_V \cdot \ln(V/V_0)$. For binary nitride AlN, GaN, and InN, a_V takes value of -9.8 eV, -7.6 eV, and -4.2 eV, respectively.[157]

(iii) Electron affinity χ also plays a role in the self-consistent electrostatic potential calculation. In a simplified physical picture, χ is described as the energy required to move an electron from the CBM to the vacuum near the surface of the material. Therefore, χ is defined as the energy difference between the CBM and the vacuum energy at the surface, i.e., $\chi = E_{\text{vac}} - E_C$. [160]

Electron affinity of group III-nitrides has been experimentally measured by several techniques such as UV-photoemission spectroscopy (UPS), scanning photoelectron spectroscopy (PES), and conductive AFM I-V characteristics.[161, 162, 163, 164] Nonetheless, the experimental measured values scatters over a large range, for instance, χ measured on GaN ranges from 2.1 to 4.26 eV[161, 165] as compared to a value of 3.86 eV calculated with DFT.[166] The inconsistency in electron affinity measurements is attributed to the fact that these experiments are highly sensitive to surface conditions, surface orientation and the type and concentration of surface states. Therewith, surface contamination, adsorbates, and surface reconstruction can affect the electron affinity measurement, leading to variations in the results.

As for the (Al,In)N investigated in thesis, a few studies about its electron affinity has been performed: Schulz *et al.* conducted combined photoluminescence excitation (PLE) spectroscopy and tight-binding (TB) theoretical model to study the band edge of $\text{Al}_{1-x}\text{In}_x\text{N}$ with x ranging from 0.082 to 0.170 grown by metal organic chemical vapor deposition (MOCVD).[154] Their results revealed that at the GaN/ $\text{Al}_{1-x}\text{In}_x\text{N}$ interface, the band offset is highly dependent on the composition of ternary layer. At the lattice-match condition (i.e., $x=0.17-0.19$), the conduction

band offset is determined as 0.2 eV which implies an electron affinity of 3.9 eV for the $\text{Al}_{0.82}\text{In}_{0.18}\text{N}$ layer. Another similar system $\text{Al}_{0.83}\text{In}_{0.17}\text{N}$ grown by MOCVD has been investigated by Akazawa *et al.*[167] The authors applied X-ray photoelectron spectroscopy (XPS) on the 2.5 nm thin layer and identified a 0.9 to 1.0 eV conduction band offset at the (Al,In)N/GaN interface (i.e., an electron affinity of about 3.2 eV for the ternary (Al,In)N layer). Using the same XPS technique, Jiao *et al.* carried out investigations on the molecular beam epitaxy (MBE)-grown $\text{Al}_{1-x}\text{In}_x\text{N}/\text{GaN}$ heterostructures with varying composition.[168] Their results suggest a valence band offset of 0.15 and 0.12 eV, hence an electron affinity of 3.45 and 3.48 eV for $x=0.17$ and 0.18, respectively. Wang *et al.* performed XPS and PL to study the band offset at MOCVD-grown $\text{Al}_{1-x}\text{In}_x\text{N}/\text{GaN}$ quantum wells structure and compare the results with the First-principle calculation.[169] They concluded a conduction band offset at the interface of 0.6 eV which translates to 3.5 eV as the electron affinity of (Al,In)N layer. By utilizing the unified hybrid density functional theory, Tsai *et al.* conducted calculations on the electron affinity of zincblende (110) and wurtzite (10 $\bar{1}$ 0) nitride surfaces.[170] After taking the strong non-linearity dependence of band edge on compositions into consideration, they proposed that for the lattice-match (Al,In)N, the electron affinity stays in the range of 3 eV to 3.2 eV.

The above-mentioned values of x of (Al,In)N with close to lattice-match composition have been summarized and plotted in Fig. 3.11. In this thesis, I use the intermediate electro affinity values of 3.5 eV and 4.1 eV for the ternary (Al,In)N and GaN layers, respectively.

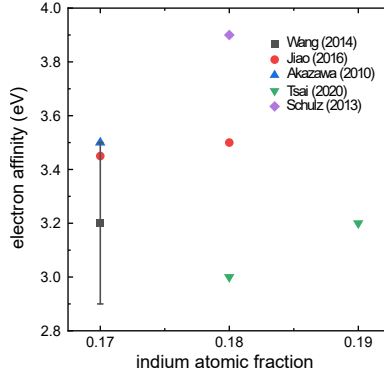


Figure 3.11: Summary of the electron affinity values of $\text{Al}_{1-x}\text{In}_x\text{N}$ (with $x=0.17$ -0.19) found in literature.[154, 167, 168, 169, 170]

3.3.3 From electrostatic potential to electron optical phase

For a lamella with uniform thickness and constant electrostatic potential along thickness direction, the relationship between electron optical phase and electrostatic potential is given by Eq. (2.5). In this equation, the total electrostatic potential is separated as two contributions, i.e., V_{EP} and V_{MIP} . The former term represents the electrostatic potential which acts on free charge carriers and which arises from effects such as doping and polarization. The term V_{MIP} is a material-dependent property and it describes the electrostatic potential energy experienced by an electron as it travels through crystal lattice. It is defined as the average Coulomb potential within the crystal with the zero point of potential chosen in the vacuum at infinite distance from the crystal.[171]

From theoretical side, V_{MIP} can be computed utilizing various approaches such as DFT and tight-binding models.[172, 173, 174, 175, 176] In an intuitive physical picture, V_{MIP} is expressed as the superposition of the forward scattering factors of atoms i in the unit cell of volume V_C neglecting bonding effect:[173]

$$V_{MIP} = \frac{\hbar}{2\pi m e V_C} \sum_i f_{el}^i(0) \quad (3.47)$$

where \hbar is the Plank constant, m is the electron mass, and $f_{el}^i(0)$ is the elastic atomic scatter factor.

Theoretical studies have been carried out to investigate the V_{MIP} values of binary III-nitride compounds: Utilizing DFT calculations, Kruse *et al.* estimate V_{MIP} of 16.82 V, 14.23 V, and 17.35 V for the zincblende structure GaN, AlN, and InN, respectively.[177] Another calculation provides values of 16.89 V, 15.88 V, and 18.9 V for the corresponding wurtzite binaries[176] (which are the values used for the self-consistent electrostatic potential calculation throughout this thesis since all semiconductor crystallized in the wurtzite structure).

From experimental side, techniques such as electron holography have been employed to measure V_{MIP} of semiconductor materials.[177, 178, 179] However, concerning binary group III-nitride semiconductors, existing studies focus only on measuring V_{MIP} of GaN. For instance, using electron holography, Wong *et al.* measured a V_{MIP} of 16.67 ± 0.3 V for wurtzite GaN.[180]

Moreover, to date, neither a theoretical nor an experimental study has been conducted on V_{MIP} values for ternary III-nitride alloys. Therefore, interpolating V_{MIP} from values of constituent binaries to determine V_{MIP} for III-nitride alloys has to

be treated with caution. This is due to the fact that the electronic properties of ternary nitride compound, e.g., bandgap energy as well as spontaneous polarization, often exhibit a non-linear dependence on its alloy composition.[147, 143, 144] Hence, a bowing factor needs to be incorporated into the linear interpolation to accurately predict the electronic properties of a ternary nitride alloy.[144] However, due to the lack of relevant studies, the potential bowing effect of V_{MIP} is neglected in this thesis.

Determination of V_{MIP} for strained structures, such as epitaxial layers, appears to be more challenging due to the fact that V_{MIP} is anticipated to be strongly influenced by the unit cell volume. At present stage, there is neither a theoretical nor an experimental study that directly investigates the influence of strain on V_{MIP} . Therefore, as a simplified approximation, the change of V_{MIP} due to strain is assumed to be straightforwardly proportional to the change in volume of unit cell V_C , i.e., the density of atoms. In case of wurtzite nitride semiconductors, V_{MIP} under strained condition is expressed as:

$$V_{\text{MIP}}^{\text{strained}} = V_{\text{MIP}}^{\text{unstrained}} \cdot \frac{a_0^2 c_0}{a^2 c} \quad (3.48)$$

with a_0 (a) and c_0 (c) being unstrained (strained) lattice constant along $[\bar{1}\bar{2}10]$ and $[0001]$ direction, respectively.

Chapter 4

Electrostatic versus diffraction contribution to electron holography: An experimental approach

4.1 Overview

The contrast arising from the dynamic diffraction significantly distorts the phase maps measured by electron holographic experiments. Therefore, the reliable and quantitative extraction of the electrostatic potential can only be accomplished when the dynamic diffraction is effectively suppressed. In this chapter, an experimental methodology for optimizing the lamellas' orientation with respect to negligible dynamic diffraction is discussed.

4.2 Results

The GaN/(Al,In)N/GaN heterostructure #2 from bulk sample A3162 (see Chap. 2 for details) is investigated in a tilt series experiment. In the actual TEM measurement, the tilt angles (as the read-out from the piezo-stage of the TEM holder) are given with respect to the lamella orientation relative to the TEM holder. Therefore, these tilt angles are not necessarily corresponding to the actual orientation of the lamella (called absolute orientation in the following, i.e., absolute with respect to the incoming electron beam). The read-out tilt angles can be calibrated to absolute values by a quantitative comparison between simulated CBED patterns and

the experimental ones. In this chapter, the simulation of CBED patterns is carried out with the multislice software Dr. Probe.[66]

Figure 4.1 illustrates the comparison between the calculated CBED patterns (displayed in false color) and experimental ones obtained on GaN layers (displayed in grey scale). The major Kikuchi bands $[0002]$ and $[000\bar{2}]$ as well as some low-order reflections are highlighted. The CBED patterns move parallel and transverse to these major Kikuchi bands with the TEM holder's a and b tilt angle (see Fig. 2.11), respectively. For the CBED patterns illustrated in Fig. 4.1(a), only the (0000) reflection (i.e., corresponding to the direct electron beam) is strongly excited. In contrast, in Fig. 4.1(b), the (0000) , (0002) , and (0004) reflections are all excited. The matching between simulated and measured CBED patterns is accomplished by the systematical alignment between the $[0002]$ and $[000\bar{2}]$ Kikuchi bands, and superimposition of the low-order reflections. The absolute orientations of lamella in (a) and (b) are calibrated as $a=6.80^\circ$, $b=1.45^\circ$ and $a=6.80^\circ$, $b=0.60^\circ$, respectively. The tilt angles present in the following content are all calibrated to the absolute values following the same method.

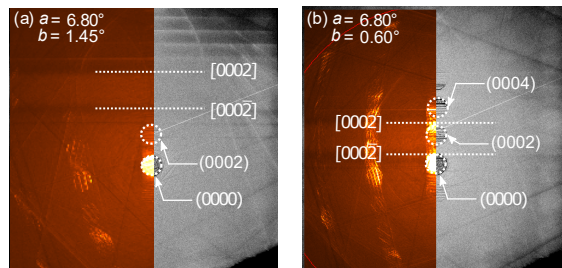


Figure 4.1: Measured CBED patterns (displayed in grey scale) and their best fit simulation (displayed in false color). In (a), the best agreement is found for $a=6.8^\circ$ and $b=1.45^\circ$, whereas $a=6.8^\circ$ and $b=0.60^\circ$ corresponds to the lamella orientation shown in (b). The matching is accomplished by the systematical alignment between the $[0002]$ and $[000\bar{2}]$ Kikuchi band and the superimposition of the low-order reflections.

Figure 4.2 illustrates the tilt series results: The phase change profiles and amplitude profiles across the GaN/(Al,In)N/GaN heterostructure are plotted against corresponding a tilt angles. Figure 4.2(a1) and (a2) report the phase change profiles and amplitude profiles acquired with the nearly edge-on lamella orientation (i.e., $b=0.60^\circ$), respectively. The ternary (Al,In)N layer exhibit lower values in phase compared to the adjacent GaN layers, primarily due to a lower mean inner potential V_{MIP} . Notably, the relative phase difference between the adjacent GaN

and (Al,In)N layers fluctuates significantly. This fluctuation can also be observed in the corresponding amplitude profiles displayed in Fig. 4.2(a2). In addition, two prominent peaks at the interfaces of the heterostructure can be noticed in the amplitude profiles. On the basis of these observations, it is concluded that all the phase change maps acquired with $b=0.60^\circ$ are strongly influenced by the dynamic diffraction. Hence, it is not possible to accurately retrieve the electrostatic potential information from the data acquired under such conditions.

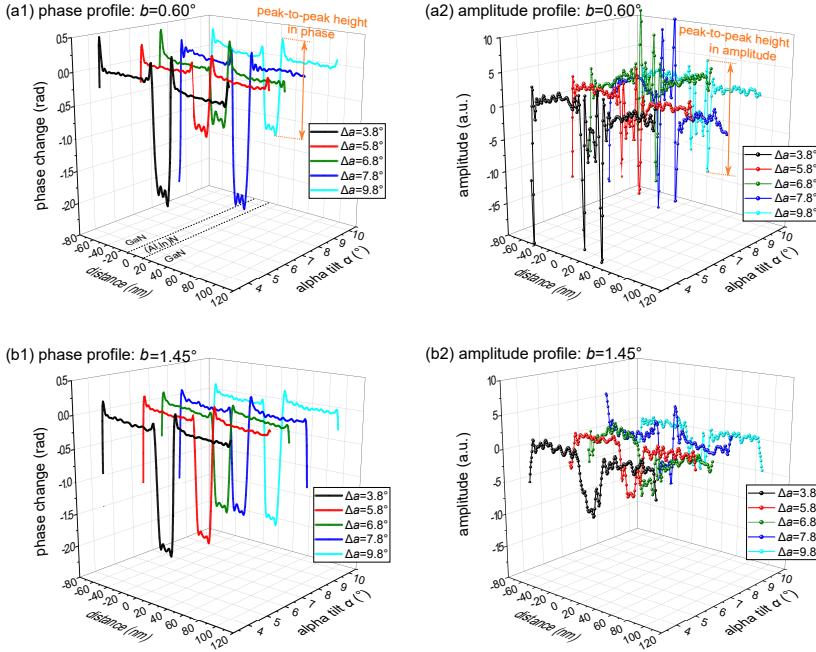


Figure 4.2: Phase change profiles and amplitude profiles extracted from GaN/(Al,In)N/GaN heterostructure. (a1,a2) Represent the phase and amplitude profiles acquired with a tilt angle ranging from 3.8° to 9.8° at nearly edge-on orientation (i.e., $b = 0.60^\circ$), respectively. The fluctuation of both phase and amplitude profiles are evident. The phase change profiles and amplitude profiles obtained with $b = 1.45^\circ$ and a ranging from 3.8° to 9.8° are shown in (b1) and (b2), respectively. In this case, the amplitude and phase profiles are nearly independent of the tilt.

In contrast, the phase change profiles and amplitude profiles obtained with a same set of a tilt angles, but with $b=1.45^\circ$, i.e., slightly off the edge-on orientation, are displayed in Fig. 4.2(b1) and (b2), respectively. The most prominent feature is that

the difference in phase between GaN and (Al,In)N layers is nearly constant, independent of the a tilts, as shown in Fig. 4.2(b1). Moreover, the amplitude profiles do not show strong peaks at the interface of heterostructure. Therefore, it is concluded that the data acquired with $b=1.45^\circ$ exhibit negligible dynamic diffraction.

In order to quantify the influence of the dynamic diffraction, the magnitudes from the positive to negative peak occurring at the hetero-interface, labelled as the peak-to-peak height in phase/amplitude (see Fig. 4.2(a1,a2)), are extracted. Figure 4.3(a) and (b) depict comparisons of the peak-to-peak height in phase (black spheres and dashed line) and in amplitude (red spheres and dashed line) for different a tilt angles with $b=0.60^\circ$ and $b=1.45^\circ$, respectively.

For data acquired at $b=0.60^\circ$, i.e., with strong dynamic diffraction (Fig. 4.3(a)), the peak-to-peak height in phase fluctuates strongly between 2.46 to 1.18 rad as a increases from 3.8° to 9.8° . An average value of 1.71 ± 0.55 rad is determined. The rather large error is attributed to the contrast arising from dynamic diffraction. A correlated trend is observed in the corresponding peak-to-peak height in amplitude, which exhibits a strong fluctuation between 17.87 to 27.93 a.u. for a between 3.8° to 9.8° .

Figure 4.3(b) displays the data acquired at $b=1.45^\circ$ (i.e., with suppressed dynamic diffraction): The peak-to-peak height in phase remains in a range between 1.63 to 2.20 rad with different a tilt angles. The average peak-to-peak height in phase is calculated as 1.95 ± 0.22 rad, exhibiting significantly less fluctuation in comparison to the data shown in Fig. 4.3(a). In addition, the corresponding peak-to-peak height in amplitude only slightly varies from a minimum value of 6.61 a.u. to a maximum value of 11.92 a.u. Note that the fluctuation in peak-to-peak heights in phase and amplitude are no longer correlated.

On the basis of these observations, important conclusions are drawn: In case of $b=0.60^\circ$, the strong dynamic diffraction manifests as the widespread distribution of values in peak-to-peak height in phase. This is correlated with the same fluctuation in peak-to-peak height in amplitude. In contrast, with $b=1.45^\circ$, the fluctuation of peak-to-peak height in phase and amplitude is greatly suppressed and no correlation is observed. Furthermore, by relating these findings with the CBED patterns shown in Fig. 4.1, it can be summarized that strong dynamic diffraction across the III-nitride interface occurs if low-order reflections are strongly excited. Conversely, dynamic diffraction is significantly reduced if only the (0000) reflection is excited.

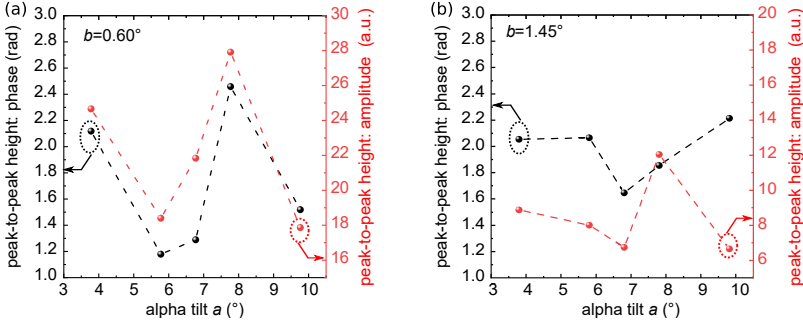


Figure 4.3: (a,b) The peak-to-peak height extracted from the phase change profiles and amplitude profiles for $b=0.60^\circ$ and 1.45° with various a tilt angles, respectively.

4.3 Discussion

Earlier studies reported that a tilt angle of $a=(1.5^\circ-2^\circ)$ about the $[1\bar{2}10]$ axis, coupled with an edge-on orientation (i.e., $b=0^\circ$), leads to a minimal dynamic diffraction condition across the (In,Ga)N/GaN interface.[181, 182] In another study, Denaix *et al.* applied an even smaller a tilt angle (e.g., 0.3°) about the $[1\bar{2}10]$ axis (while maintaining an edge-on orientation) to avoid dynamic diffraction across the GaN/AlN interface.[183]

Based on the angles provided in literature, I simulated the corresponding CBED patterns. Figure 4.4(a), (b), and (c) are simulated under edge-on lamella orientation and with $a=0.3^\circ$, 1.5° , and 2° , respectively. The most prominent observation is that many low-order reflections are strongly excited.

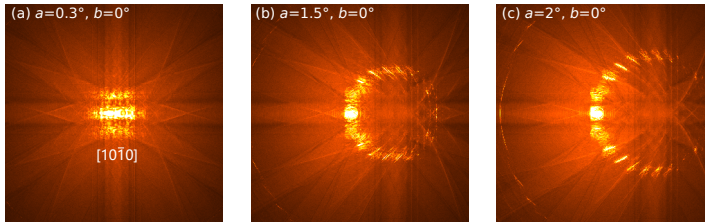


Figure 4.4: Simulated CBED patterns with tilt angles exhibiting suppressed dynamic diffraction contrast, as derived from literature.[181, 182, 183]

These results appear to be in contradiction to the tilt angles presented in this thesis. In particular, in these previous studies, there was no tilt about the $[0001]$ axis

needed, unlike in the case presented in this chapter where a tilt angle $b=1.45^\circ$ is necessary to effectively minimize the dynamic diffraction. This apparent discrepancy can be anticipated to be related with the lack of a precise determination of the absolute lamella orientation in literature.

Ideally, for the wurtzite III-nitride semiconductor lamella, the [0001] and $[1\bar{2}10]$ axes should be parallel to the holder's a and b tilt axes (see Fig. 2.11), respectively. Such an alignment ensures that the read-out from the TEM holder's piezo-stage accurately corresponds to the actual tilt angle of the lamella. However, in practical applications, achieving this ideal alignment condition is particularly challenging:

The first issue arises during lamella preparation, the side surface of the lamella is rather rough as it is lifted straightforwardly from the bulk sample. As a result, during welding of the lamella to the TEM grid, this rough surface may cause the lamella to misalign from the desired lamella orientation. This is a rather common misalignment effect occurring during FIB process.

During installation of the grid on the TEM holder, a fine alignment between the grid with the holder's tilt axis can be challenging. The difficulty arises from the application of washers on top of the grid, which can be anticipated to cause slight movement of the grid below.

The piezo-stage exhibits finite precision in tilt angle. The backlash of the stage caused by piezo drift can also lead to inaccurate read-out, especially when tilting with fine steps.

On the basis of aforementioned misalignments between the lamella and the grid as well as between the grid and the TEM holder, which results in unknown offsets in the angle read-outs in the first place, tilting the lamella in one direction can be expected to be accompanied by a tilt in another direction, leading to the discrepancy between actual lamella orientation and the read-outs from piezo-stage.

4.4 Summary

Dynamic diffraction distorts the phase map measured by electron holographic experiments, thus hampering quantitative extraction of electrostatic potential information. In this chapter, the peak-to-peak heights at the (Al,In)N/GaN hetero-interface in obtained tilt series results are extracted to quantify the influence of dynamic diffraction. It is found that when the lamella is close to the edge-on orientation, i.e., $b=0.60^\circ$, strong dynamic diffraction occurs. This lead to a strong

and correlated fluctuation in peak-to-peak height in phase and amplitude. An average peak-to-peak height 1.71 ± 0.55 rad is found. In contrast, when the lamella is oriented off the edge-on orientation, i.e., $b=1.45^\circ$, the dynamic diffraction is negligible and an average peak-to-peak height with less fluctuation, i.e., 1.95 ± 0.22 rad, is revealed. By relating these findings with CBED patterns, it is concluded that the occurrence of strong dynamic diffraction across the III-nitride hetero-interface is more likely when low-order diffraction reflections are strongly excited.

By examining the tilt angles achieving the suppressed dynamic diffraction in III-nitride heterostructure from literature and comparing them with simulation, it is found that the data in literature should be greatly influenced by the dynamic diffraction. The fact that the dynamic diffraction is absent in these studies can be related to the potential misalignments of lamella.

The approach introduced in this chapter is applied to all other electron holographic experiments present in this thesis to avoid dynamic diffraction.

Chapter 5

Origin of phase contrast of modulation-doped GaN

5.1 Overview

In this chapter, some unique, surprising, and intriguing properties of the phase change maps acquired on the n - n^+ doping step will be elucidated:

First, it will demonstrate that the phase contrast across the doping step is (a) larger than the expected value (without the assumption of the surface pinning) and (b) that it is independent of the lamella thickness.[35, 29, 30, 31, 32] Both observations are in contrast to earlier studies on p - n junction, where the phase contrast is always smaller than theoretical values, and increases with lamella crystalline thickness.[94, 116, 91, 117, 92, 89, 93, 184, 185, 186, 187, 188, 119] This apparent contradiction can be resolved and perfectly understood in the framework of the surface pinning model described in Chap. 3 and the interplay of the screening of the built-in potential and surface potential.

A part of the content of this chapter has been published in Ultramicroscopy with DOI:10.1016/j.ultramic.2024.114006.[189]

5.2 Results

14 lamellas with different thicknesses (labelled as L1-L14) are prepared and investigated (bulk sample A3162, for details see Chap. 2). An example of a phase map derived from a hologram acquired across GaN doping step is displayed in Fig. 5.1(a). The investigated lamella L4 exhibits a crystalline thickness of 257 ± 6 nm as measured by CBED. The [0001] growth direction points to the right. The GaN layer

with lower donor concentration exhibits a darker contrast. The corresponding phase change profile, averaged over 500 nm width, is plotted in Fig. 5.1(b). The difference in phase across the doping step, denoted as $\Delta\phi_{\text{junction}}$, is found to be 0.40 ± 0.02 rad. Figure 5.1(c) reports the $\Delta\phi_{\text{junction}}$ values measured from various lamellas with crystalline thicknesses ranging from 188 to 380 nm (black spheres). Additional data points (marked with blue triangles) are attached for comparison and will be examined in Chap. 7.

A linear fit (blue line) reveals a weak slope of $(2.0\pm 1.3)\times 10^{-4}$ rad/nm with an intercept of 0.33 ± 0.04 rad. The large intercept as well as the weak slope indicate an almost thickness independent phase contrast across the doping junction.

For quantitative interpretation of the measured phase change profiles, self-consistent electrostatic potential calculations are carried out, taking the presence of a surface Fermi-level pinning E_{pin} of the TEM lamellas into consideration. It is recalled that the FIB preparation results in a lamella consisting of a pristine core, covered by a defect-rich crystalline inner shell and an amorphous outer shell, as described in Chap. 3 and in Ref.[190] The Fermi-level pinning has been shown to arise from a FIB-induced near surface implantation of carbon on nitrogen sites in the inner shell.[190] The quantitative analysis of the measured phase change profiles is based on a two-step process, as described in Chap. 3.[35]

In Fig. 5.1(b), the measured phase change profile across GaN doping step is compared with calculated results, using E_{pin} as a fitting parameter. The red and blue lines represent calculated phase change profiles with a surface Fermi-level pinning of 0.69 and 0.59 eV above the valence band edge (E_V), respectively, while the green dashed line is derived assuming no pinning states at the surface, i.e., only bulk conditions.

With the presence of pinning states at the surfaces of the lamella, the phase contrast and $\Delta\phi_{\text{junction}}$ increase with E_{pin} shifting toward E_V . The best agreement between the experimental phase change profile shown in Fig. 5.1(b) and the calculated result is found for $E_{\text{pin}}=0.69\pm 0.10$ eV above the valence band. In order to provide a feeling for the accuracy of E_{pin} a second simulation with a pinning level 0.1 eV closer to E_V is illustrated.

The same analysis was performed for all lamellas. Figure 5.2 illustrates the derived pinning levels E_{pin} vs. crystalline thickness (ranging from 188 to 380 nm) for all investigated 14 lamellas (red spheres). The values derived from the additional data points are also shown (blue triangles). A linear fit to the data reveals a constant average Fermi-level pinning energy independent of the lamella thickness

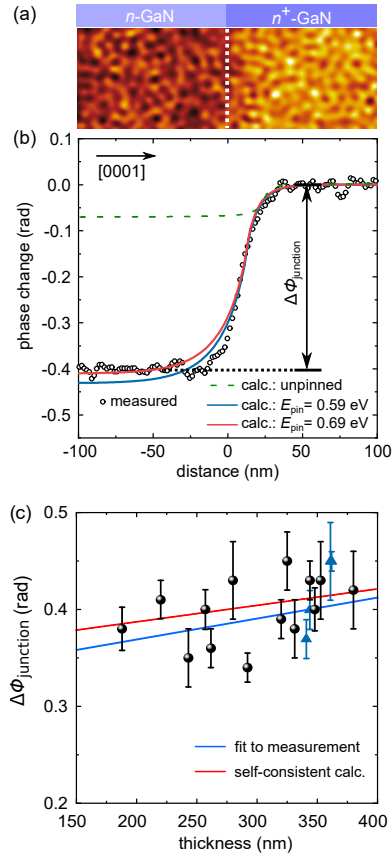


Figure 5.1: (a) Phase map across an n - n^+ GaN doping step. The n -GaN layer exhibits a darker contrast. (b) Phase change profile extracted from the phase map averaged over a width of 500 nm. The n - n^+ interface is positioned at 0 nm. The phase contrast across the doping step $\Delta\phi_{\text{junction}}$ is 0.4 rad. (c) $\Delta\phi_{\text{junction}}$ versus crystalline thickness of the measured lamellas. The blue line represents a linear fit, whereas the red line is obtained from self-consistent electrostatic simulations. Additional data points represented by blue triangles will be examined in Chap. 7.

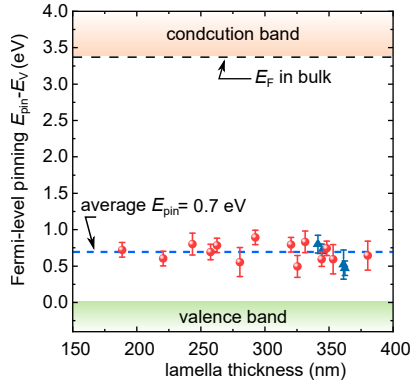


Figure 5.2: Energy position of the Fermi-level pinning E_{pin} vs. crystalline thickness derived from all investigated FIB-prepared lamellas. An average E_{pin} of 0.70 ± 0.13 eV above the valence band is revealed with no detectable thickness dependence. Additional data points denoted by blue triangles from Chap. 7 are added for comparison.

with negligible slope $[(-1.2 \pm 5.5) \times 10^{-4} \text{ eV/nm}]$. The average value of E_{pin} of 0.70 ± 0.13 eV.

5.3 Discussion

5.3.1 Origin of the phase contrast across the GaN doping step

In order to gain more insight into the origin of the phase contrast as well as interplay between lamella thickness and phase contrast across GaN doping step, I turn to the calculated cross-sectional electrostatic potential maps of lamellas with thickness of 330 nm (Fig. 5.3(a1)) and 260 nm (Fig. 5.3(b1)). The surface Fermi-level is set to be pinned at the averaged value of 0.70 eV above the valence band edge (see Chap. 3 for details about the modelling of the surface states). The modelled Fermi-level pinning takes place at the interface between vacuum and the lamella. The potential profiles extracted along the $[10\bar{1}0]$ electron beam direction at the positions of the blue (red) dashed and solid lines are shown in Fig. 5.3(a2) (Fig. 5.3(b2)) below. Note that, here, the incident electron beam direction points here from left to right.

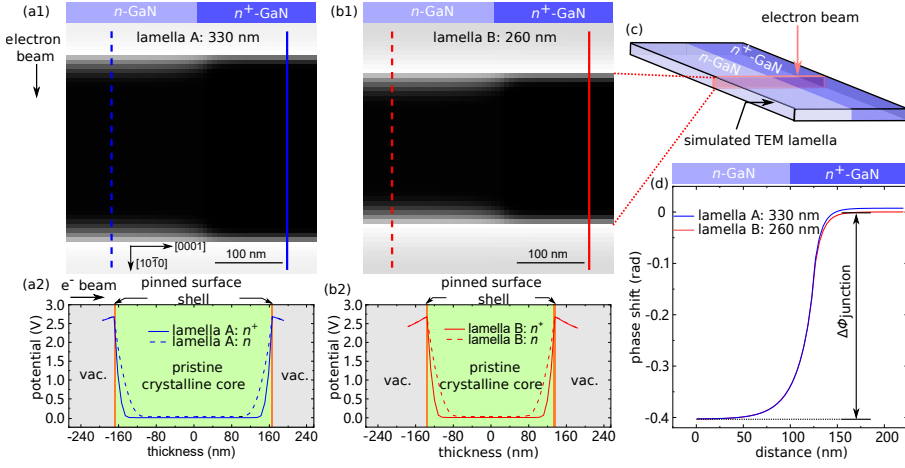


Figure 5.3: (a1, b1) Simulated cross-sectional electrostatic potential maps of the same GaN doping step for TEM lamellas with a thickness of 330 nm (a1) and 260 nm (b1). (a2) Potential profiles extracted along the respective vertical dashed and solid lines in (a1). The vacuum and pristine crystalline core are visualized with grey and green background color, respectively. (b2) Same as (a2) but extracted from (b1). (c) Sketch of a TEM lamella of the n - n^+ GaN doping step showing the spatial positions of the potential maps in (a1, b1). (d) Comparison of phase profiles calculated for lamellas with a crystalline thickness of 260 nm (red line) and 330 nm (blue line).

The potential maps and line profiles reveal that the main potential difference between the n and n^+ -doped GaN layers is found near the surfaces of the TEM lamella where the Fermi-level is pinned (vertical orange lines in Fig. 5.3(a2) and (b2)). In this region, the surface potential is screened by the displacement and re-distribution of free charge carriers. Since the screening length is exponentially decreasing with carrier concentration [191, 13], the extend of the screening region is significantly different for the n and n^+ -GaN layer, i.e. ~ 63 vs. ~ 32 nm, respectively. In contrast, in the pristine crystalline core of the lamella the potential is almost identical for the different doping levels, since the built-in potential difference between the n and n^+ -GaN layers is only 30 meV.

The potential profiles illustrate well that the largest contribution to the difference in potential and thus the phase contrast is the screening region where screening of the surface potential takes place. This leads to phase contrasts in the order of 0.38 rad across the doping step. In contrast, the phase contrast stemming from the built-in potential in the pristine crystalline core is only 0.03 rad for the 330 nm-thick lamella.

For the 260 nm thick lamella (Fig. 5.3(b2)), the built-in phase contrast is 0.02 rad, while the phase contrast induced by the screening in the depletion layer is unchanged at 0.38 rad. Thus, the built-in potential-induced phase contrast is so small that it can be almost neglected, and the predominant contribution to the phase contrast across the doping step arises from different (doping-dependent) screening lengths of the surface potential. This observation is reflected in Fig. 5.3(d) where the corresponding phase profiles integrated through the whole lamella thickness, extracted from lamella A (blue line) and B (red line) are compared. Despite lamella A is 70 nm ($\sim 27\%$) thicker than lamella B, $\Delta\phi_{\text{junction}}$ is only 0.01 rad ($\sim 2.6\%$) higher.

The solid red line in Fig. 5.1(c) illustrates the calculated $\Delta\phi_{\text{junction}}$ as a function of crystalline thickness. The thickness dependence is weak and almost linear and agrees well with the experimental data points. This supports further the above physical conclusions, that for doping modulations the screening is governing the electron optical phase contrast.

This situation can be anticipate to change, if large built-in potentials occur, such as in p - n junctions or at heterointerfaces. Then the screening and the built-in potential interact and need to be considered together. The result maybe that the contribution of the built-in potential to the electron optical phase difference is counteracted by the contribution of the screening of the surface potential. Thereby a phase difference is obtained, which is always smaller than expected without surface potentials and dead shell layers.

Finally, the defect-rich crystalline inner shell is rather thin in this case. Its' thickness can be estimated its thickness by taking into account an average thickness of the amorphous shell of 9 nm and a depth of about 15 nm, where the FIB-induced defect concentration falls below the doping concentration (see Chap. 3). This yields a thickness of about 6 nm where no screening occurs yet, as all dopants will be compensated. Hence, the material will be fully pinned and not contribute to the electron optical phase contrast. Only deeper inside the lamella screening occurs and dominates the phase contrast. Since in this case the defect rich inner crystalline shell is rather thin as compared to the lamella thickness, it is sufficient to approximate its effect on the potential as a surface Fermi-level pinning.

Hence, it is concluded that the quantitative analysis of phase differences measured by electron holography using FIB-prepared TEM lamellas, requires the consideration of more than simply a dead layer.[91, 92, 89, 93, 192, 193, 88, 194, 185, 186, 187, 31, 117, 195, 188] Instead, as discussed in Chap. 3, an amorphous outer shell, an defect-rich inner crystalline shell, and an underlying depletion region within the pristine crystalline core screening the surface potential need to be considered and

evaluated for every material investigated. In particular one needs to understand the physics of FIB-induced point defects and their charge transfer levels, which determine the Fermi-level pinning.

5.3.2 Comparison with n -type GaN structures from references

The analysis methodology and self-consistent electrostatic potential calculation can be applied to earlier published data, too. The aim is to assess if a E_{pin} value similar to that unraveled in this chapter, and therefore a similar surface condition, can be identified. However, the choice of examples is not straightforward, primarily because of the uncertainty associated with the lamella preparation process in literature. Using a different FIB preparation process, such as employing different protection layers, applying heavier ion sources and higher ion voltage,[92] can be anticipated to give rise to lamellas with different surface conditions. Therefore, the following discussion is restricted to n -type GaN layers prepared using a FIB process with parameters similar to those applied in this chapter.

(i) The data set closest to my experimental parameters is that of Yamamoto *et al.*,[29] where a protective carbon layer was used. Utilized the phase-shift electron holography in conjunction with a multiple biprism setup, Yamamoto *et al.* measured the phase contrast across the interface between n^+ -type GaN (Si: $5 \times 10^{18} \text{ cm}^{-3}$) and n -type GaN (Si: $5 \times 10^{17} \text{ cm}^{-3}$) layer. In the course of lamella preparation, following the application of a carbon protective layer on the bulk sample at room temperature, the lift-out and thinning process were executed at 130 K. The lift-out and initial thinning were performed using Ga^+ at 40 kV, whereas the final polishing was conducted at 5 kV. The resulting lamella exhibits a final thickness of 350 nm.

The phase contrast across the n^+ - n GaN layers was measured as $0.55 \pm 0.03 \text{ rad}$. In contrast, theoretical predictions yield a value of 0.14 rad (derived from a Poisson solver software, Aestimo, without considering surface Fermi-level pinning).[196] Taking surface pinning into account, my analysis methodology yields the best fit for a surface Fermi-level pinning of $0.84 \pm 0.2 \text{ eV}$ above E_V . This pinning value is in line with E_{pin} unraveled on my GaN doping steps. The slightly higher energy of E_{pin} may be attributed to other uncertainties occurred during FIB process.

(ii) Another relevant study was conducted between unintentional-doped GaN layer and n -type GaN substrate (Si: $3 \times 10^{19} \text{ cm}^{-3}$) by Boley *et al.*[197] The phase contrast between these two GaN layers was measured as 0.59 rad with an uncertainty of roughly 0.03 rad (as visually estimated from the figure in literature). During the

self-consistent electrostatic potential calculation, the structure is simulated assuming GaN cap with a *n*-type doping of $5 \times 10^{17} \text{ cm}^{-3}$, as it is the donor concentration generally found in the unintentional-doped GaN layer.[198] With a surface Fermi-level pinning of $\sim 0.55 \text{ eV}$ above the valence band, the calculated phase contrast is found to be in good agreement with the measured value. In this case, the derived E_{pin} is in good accordance with values revealed on GaN doping step in this chapter.

5.4 Summary

In this chapter, the underlying physical origin of the significant enhancement of the phase contrast observed across GaN doping steps, in contrast to theoretical predictions, is unraveled by combining off-axis electron holography data with self-consistent electrostatic potential calculations. This analysis incorporates consideration of the surface Fermi-level pinning. Some important conclusions are drawn:

(i) The predominant contribution to the phase contrast is shown to arise from the doping dependent screening length of the FIB-induced surface Fermi-level pinning occurring in the defect-rich crystalline inner shell (below the outer amorphous shell). This near surface screening region remains unchanged for lamellas with different thicknesses, resulting in an almost constant phase contrast vs. thickness. The contribution of the built-in potential is almost negligible, since its value is too small for modulation doping and only relevant for large built-in potentials at e.g. *p-n* junctions. Thus, the weak built-in potential of GaN doping steps adds only a small thickness dependence to the phase contrast.

(ii) A surface Fermi-level pinning of 0.7 eV above the valence band edge is revealed on as FIB-prepared lamellas by comparing the phase change profile derived from theoretical calculations and experimental data. Hence, it is concluded that by following a same procedure in the course of FIB process, lamellas with a similar surface condition (hence a consistent value in E_{pin}) can be produced. By applying the same method to the FIB-prepared *n*-type GaN structures present in other studies, similar values in surface Fermi-level pinning are identified.

In the upcoming chapter, the results of in-situ annealing electron holographic experiment will be studied. Through the examination of these results, the type of FIB-implanted point defects responsible for inducing the observed Fermi-level pinning will be elucidated.

Chapter 6

Quantification of surface effect: Fermi-level pinning by substitutional C

6.1 Overview

In this chapter, thermal healing of FIB-implanted defects in GaN is investigated by off-axis electron holography. The data reveal that healing starts at temperatures as low as about 250 °C. The healing processes lead to an irreversible transition from defect-induced Fermi-level pinning near the valence band toward a midgap pinning induced by the crystalline-amorphous transition interface. Based on the measured pinning levels and the defect charge states, the dominant defect type is identified as substitutional carbon on nitrogen sites.

A part of the content of this chapter has been published in Applied Physics Express with DOI:10.35848/1882-0786/ad163d.[190]

6.2 Results

6.2.1 Single-cycle in-situ annealing

Four TEM lamellas, denoted as A1 and A2 (extracted from bulk sample A3777), B1 and B2 (extracted from bulk sample A3162), are studied. For the sample details see Chap. 2. Exemplary amplitude and phase map extracted from a GaN δ -doped layer on lamella A1 at 500 °C, are displayed in Fig. 6.1(a) and (b), respectively. The spatial resolution of the phase maps is 3.6 nm, as derived from the spacing of

the interference fringes. In order to suppress the dynamic diffraction contrast, the lamellas were tilted with a rotation axis perpendicular to the interface layers. The phase profiles were extracted only in regions without diffraction contrast. The sign convention is assumed such that the region with higher n doping concentration appears to be brighter in phase map. From the obtained phase maps, profiles along the [0001] growth direction by integration along the perpendicular $[1\bar{2}10]$ direction are extracted. An example phase profile is overlaid on the phase map in Fig. 6.1(b) (yellow line). The most prominent feature is the pronounced phase peak at the position of the δ -doped like layer (at spatial position 0 nm). Across such a homostructure, no traces of polarization changes or strain can be present and thus only doping governs the phase changes.[35, 199, 200]

Next, I focus on the changes of the electron optical phase between the different layers as a function of annealing temperature. The temperature is increased in steps of typically 50°C, and each temperature is maintained for 30 minutes to ensure that the lamella reaches thermal equilibrium, and the microscope returns to a stable condition. Figure 6.2(a) illustrates an overview of the temperature-dependent changes of the phase profiles acquired from lamella A1. The phase change difference $\Delta\varphi_{\text{peak}}$ between the δ -doped GaN layer and remaining MOVPE-grown GaN buffer is found to increase first from 0.30 rad at RT to 0.38 rad at an annealing temperature of 250-300°C. At higher temperatures, the intensity decreases again down to 0.25-0.28 rad. After cooling down back to RT, an irreversible decrease of the intensity of the phase peak down to 0.14 rad occurred. The reproducibility of this behaviour has been experimentally confirmed across all four lamellas as illustrated in Fig. 6.2(b).

Note, the GaN pseudosubstrate exhibits a pronounced temperature evolution of the phase in Fig. 6.2(a) as well. However, this evolution varies significantly for different lamellas and hence for different substrate locations. The variability points to variations in free carrier concentrations within the substrate, attributed to v-shaped defects and threading dislocations.[201] Therefore, I focus on the MOVPE buffer and the adjacent δ -doped layer, only.

6.2.2 Two-cycle in-situ annealing

To investigate the reversibility of the observed thermal-induced effects, an additional annealing cycle is applied to lamella B1, subsequent to the first annealing cycle. Both cycles undergo an identical annealing temperature profile, which involves a gradual temperature increase from room temperature (27°C) to a maximum of 490°C, followed by an abrupt cooling-down to room temperature. The

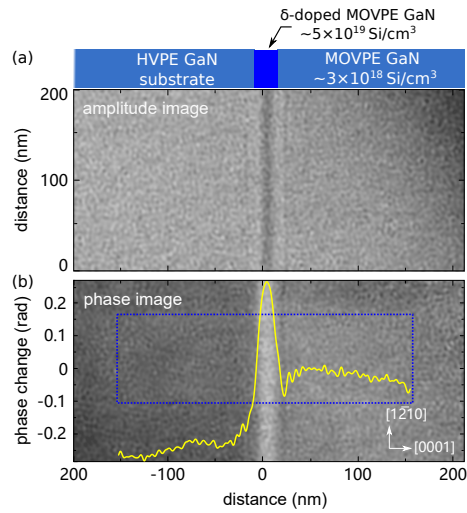


Figure 6.1: (a) Amplitude and (b) electron phase maps of lamella A1 recorded at 500°C , reconstructed from 25 single holograms obtained by off-axis electron holography. The vertical contrast line at the substrate (left)-MOVPE-grown GaN (right) interface at 0 nm stems from a δ -doped like layer. The overlaid phase profile in (b) is extracted from a region free from dynamic diffraction contrast, marked by a blue dotted rectangle. Adapted from K.Ji *et al.* 2024 Appl. Phys. Express 17 016505.[190]

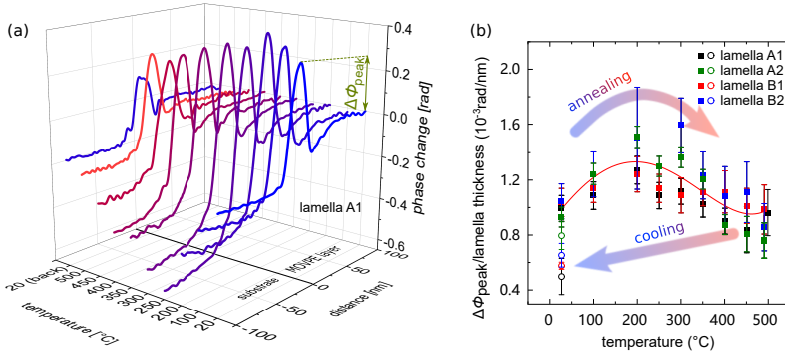


Figure 6.2: (a) Electron phase profiles extracted in [0001] growth direction at different annealing temperatures. The delta-doped layer is at spatial position 0 nm, where a phase peak appears. Distances larger (smaller) than zero correspond to the MOVPE-grown GaN layer (pseudosubstrate). (b) Reproducibility of the temperature dependent evolution of the phase peak height ($\Delta\phi_{\text{peak}}$ marked in (a)) normalized using the lamellas' crystalline thickness. Below (above) $\sim 250^\circ\text{C}$, the phase difference increases (decreases). Adapted from K.Ji *et al.* 2024 Appl. Phys. Express 17 016505.[190]

second annealing cycle is conducted 11 hours after the completion of the first cycle. During this interruption between the two annealing cycles, the lamella is kept inside the microscope chamber at room temperature with TEM gun valve closed.

The phase profiles extracted at different annealing temperatures from the second annealing cycle are depicted in Fig. 6.3(a). To highlight the temperature-dependence of $\Delta\phi_{\text{peak}}$, data measured from the second annealing cycle (black symbols) are reported in Fig. 6.3(b). Before the onset of the second annealing cycle, $\Delta\phi_{\text{peak}}$ at room temperature remains at 0.20 rad, essentially the same value as measured after the completion of the first cycle. In contrast to the results from the first annealing cycle (see Fig. 6.2(b)), $\Delta\phi_{\text{peak}}$ from the second annealing cycle progressively increases with rising temperature. From annealing temperatures of 100°C to 400°C , $\Delta\phi_{\text{peak}}$ rises from 0.22 to 0.28 rad. At the highest annealing temperature of 490°C , $\Delta\phi_{\text{peak}}$ reaches 0.32 rad, closely resembling the value obtained at the same temperature during the first annealing cycle. Following the cooling-down stage, $\Delta\phi_{\text{peak}}$ returns to 0.20 rad, effectively the same as the value measured before the second annealing cycle. These results suggest that, during the second annealing cycle, no irreversible effects have occurred anymore. All irreversible healing took place in the first annealing cycle.

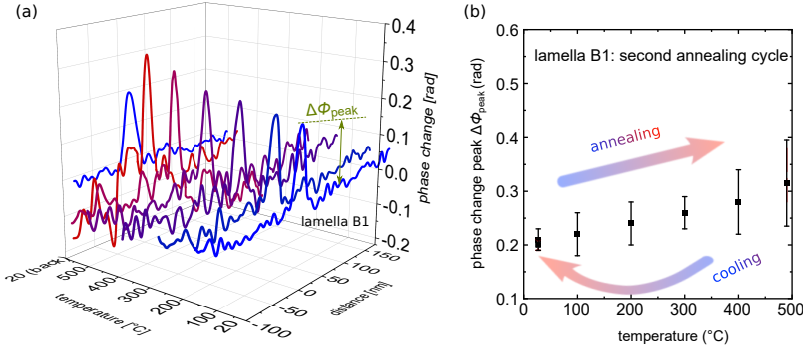


Figure 6.3: (a) Phase profiles extracted from GaN δ -doped layer on lamella B1, at different annealing temperatures for the second annealing cycle. (b) $\Delta\phi_{\text{peak}}$ extracted from the second annealing cycle versus annealing temperatures.

6.2.3 Ambient exposure and electron beam irradiation

At this stage, it is necessary to examine if non-thermal effects can contribute to the change in $\Delta\phi_{\text{peak}}$ during in-situ annealing experiment. These effects include air exposure and electron beam induced damage. Air exposure is a concern due to the fact that specific types of ambient adsorbates can generate surface states within the bandgap of GaN, giving rise to Fermi-level pinning at the semiconductor surface.[202] The electron beam-induced damage also needs to be considered since in-situ annealing experiments are time-consuming, with the entire measurement session lasting more than 8 hours, involving at least 2 hours of electron beam irradiation on the lamella. During this period, the beam-induced damage may accumulate and alter the measured phase change.[203]

Air exposure: From the initial stages of lamella preparation in the FIB chamber to the TEM measurements, despite the majority of the time the lamella is maintained within a vacuum desiccator, exposure to the ambient environment inevitably occurs during, for instance, the transfer of the lamella after the FIB process and during lamella installation on the TEM holder. For GaN, air exposure can reduce the density of pinning states and shifts the pinning levels toward the band edges, which is associated with water adsorption and dissociation, passivating intrinsic and extrinsic states in bandgap.[80] In addition, oxygen adsorbates can develop and cover the lamella surface.[204] Oxygen adsorption can create extrinsic surface states within the fundamental bandgap of III-nitride materials.[202] Therefore, it is important to determine whether the measured phase can be influenced by exposure to air.

To study the impact of ambient exposures, the experiment is designed as follows: The lamella C1 is initially installed on the TEM holder and kept under ambient conditions, which takes approximately 10 minutes. Subsequently, the holder is inserted into the TEM column, and a hologram is acquired. After the acquisition, the holder is removed from TEM, and the lamella is exposed to the ambient environment again for a specified time period. Throughout the experiment, the TEM setup and lamella orientation are maintained identical among all measurements. The evolution of $\Delta\phi_{\text{peak}}$ with respect to the corresponding air exposure duration is depicted in Fig. 6.4(a). It is evident that $\Delta\phi_{\text{peak}}$ displays effectively negligible dependence on exposure time, as all data points falling within a range from 0.38 to 0.42 rad. It is important to note that, in actual practise, the total time of ambient exposure before the insertion of the lamella into the TEM chamber would be no more than 15 minutes. Therefore, it can be concluded that ambient exposure of TEM lamellas within a relatively short duration does not influence the phase measured by electron holographic experiments.

Electron beam induced damage: The influence of electron beam induced damage is investigated on lamella C2. In this experiment, the electron dose is maintained at a relatively low level within the range of 16 to 23 $\text{e} \cdot \text{nm}^{-2}\text{s}^{-1}$ (corresponding to the electron dose applied for the electron holographic experiments). Following about a dozen minutes of experimental condition improvement (such as beam alignment and lamella tilting), the first hologram is acquired at 0 minute, after which the lamella remains stationary and is continuously exposed to the same dose of the electron beam.

In Fig. 6.4(b), $\Delta\phi_{\text{peak}}$ extracted from lamella C2 is plotted against the electron irradiation time. Notably, the values remain nearly constant regardless of the exposure time. Based on this observation, it is reasonable to neglect the influence of electron beam-induced effects during the in-situ annealing measurement.

6.2.4 Self-consistent electrostatic potential calculation: Surface Fermi-level pinning

The quantitative analysis of the in-situ annealing experimental outcomes is accomplished with the help of the self-consistent electrostatic potential simulations, using the surface Fermi-level pinning E_{pin} as a fitting parameter,[35, 205] for calculation details see Chap. 3.

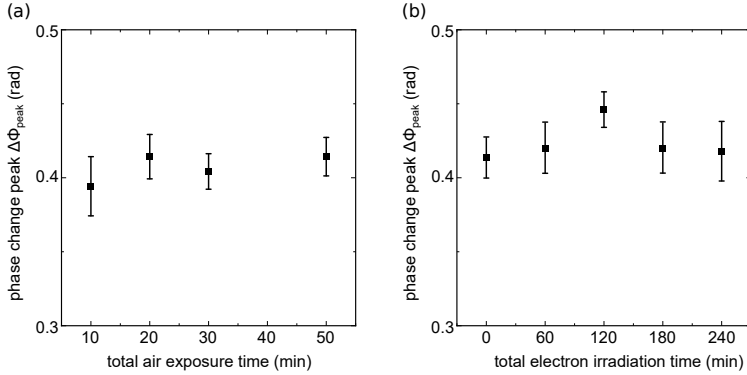


Figure 6.4: (a) $\Delta\phi_{\text{peak}}$ vs. air exposure time for lamella C1. (b) $\Delta\phi_{\text{peak}}$ vs. electron irradiation time for lamella C2 (b). These data suggests that neither air exposure nor electron beam irradiation alters the phase change measured on GaN.

Single-cycle annealing

To begin with, the simulated phase profile of the single-cycle annealing experiment is discussed. Figures 6.5(a,b) compare the measured temperature dependent phase profiles (colored symbols) with simulated ones (solid lines), illustrated exemplarily for lamella A1.

(i) In the low temperature regime (Fig. 6.5(a)) the best agreement is found for almost unchanged pinning levels close to E_V . Thus, the increase in the phase peak height is solely due to the thermal increase of the free carrier concentration, i.e. by thermal activation of the Si dopants. This effect is taken into account for all further simulations and all temperatures.

(ii) In the high temperature regime (Fig. 6.5(b)), i.e., for 300, 400, and 500 °C, the best agreement is obtained for pinning levels E_{pin} shifting toward the conduction band edge with temperature, reaching an energy position of $E_V + 2$ eV, i.e. somewhat above midgap position.

(iii) After cooling down back to room temperature, the pinning level remains above midgap.

Figure 6.5(c) illustrates the temperature dependence of the pinning levels E_{pin} . The data of all included lamellas agree quantitatively and reveal an overall increase of E_{pin} from ~ 0.6 eV in the as prepared state to ~ 2.3 eV at 500 °C. The pinning level remains at the high value of ~ 2 eV. Table 6.1 summarizes the pinning levels

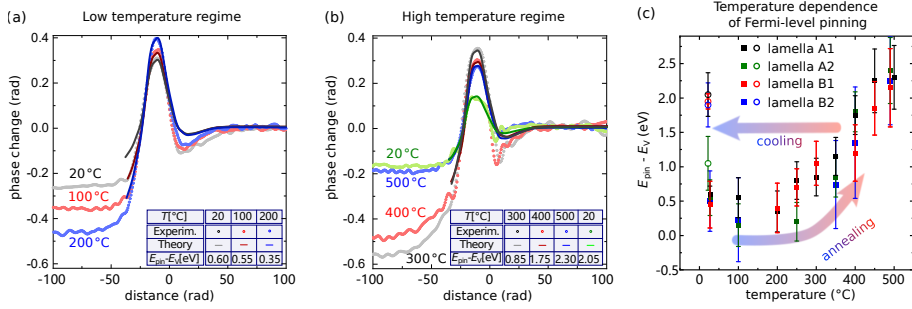


Figure 6.5: (a, b) Comparison of experimental (symbols) and simulated (lines) electron phase profiles for lamella A1 in (a) the low temperature ($\leq 250^\circ\text{C}$) and (b) the high temperature regime ($\geq 250^\circ\text{C}$). The data after cooling back to room temperature is added in (b). (c) Temperature dependence of the pinning level E_{pin} , obtained by fitting simulated phase profiles to measured ones. The data points acquired after annealing and cooling to room temperature (open symbols) are shifted by -5°C for clarity. Adapted from K.Ji *et al.* 2024 Appl. Phys. Express 17 016505.[190]

before and after annealing for all lamellas, corroborating the reproducibility of our findings.

lamella	E_{pin} at RT before annealing (eV)	E_{pin} at RT after annealing (eV)
A1	0.60 ± 0.12	2.05 ± 0.32
A2	0.55 ± 0.26	1.05 ± 0.39
B1	0.45 ± 0.34	1.95 ± 0.11
B2	0.50 ± 0.44	1.90 ± 0.32
weighted average	0.57 ± 0.05	1.90 ± 0.22

Table 6.1: Room-temperature Fermi energy pinning levels relative to E_V at the surfaces of as-prepared and 500°C -annealed TEM lamellas.

Two-cycle annealing

Next, the results from the two-cycle annealing experiment for lamella B1 will be addressed. For comparison, Fig. 6.6(a) depicts the phase profiles extracted from the *first* annealing cycle (symbols), along with their corresponding best-fit calculated profiles (solid lines). The fitting parameter E_{pin} is found to shift towards the midgap position as the temperature increases. In Fig. 6.6(b), the results of the

second annealing experiment are presented. In this case, E_{pin} is found to remain constant.

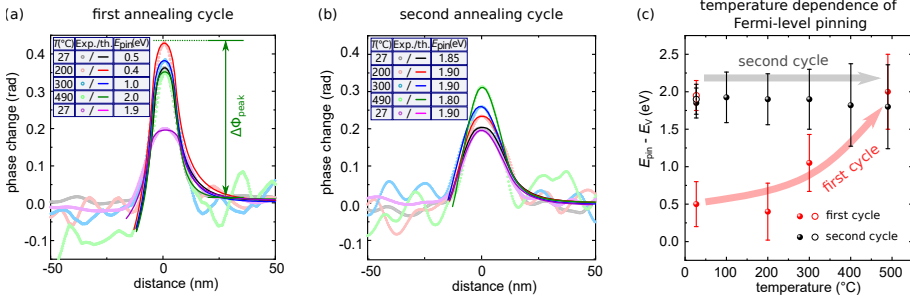


Figure 6.6: (a, b) Comparison of experimental (symbols) and simulated (lines) electron phase profiles of δ -doped GaN layer for lamella B1, during the first annealing phase cycle (a) and the second annealing cycle (b). (c) The temperature dependence of the pinning level E_{pin} relative to valence band edge, which is determined by fitting simulated phase profiles to the measured ones.

A comprehensive comparison of the dynamics of E_{pin} during the first (red symbols) and second (black symbols) annealing experiments is illustrated in Fig. 6.6(c). Notably, prior to the first annealing (i.e., as FIB-prepared surface), E_{pin} exhibits a value of 0.5 ± 0.3 rad above the valence band edge. At highest annealing temperature 490 °C, E_{pin} reaches $E_V + 2$ eV and remains high after cooling-down to room temperature. In contrast, in the course of the second annealing cycle, E_{pin} exhibits negligible dependence on the temperature and remains constant at $\sim E_V + 1.9$ eV. Therefore, it can be concluded that the thermal-induced irreversible shift in E_{pin} take place during the first annealing cycle, only. During the second annealing cycle, the increase of $\Delta\phi_{\text{peak}}$ is solely due to the increased ionization of dopants with temperature, resulting in no difference in E_{pin} before and after annealing.

6.3 Discussion

6.3.1 Type of FIB-implanted point defect

Before an in-detail discussion of the origin of the thermal-induced shift of E_{pin} can be carried out, the underlying physics responsible for the surface Fermi-level pinning at ~ 0.6 eV above valence band of the as FIB-prepared GaN lamellas needs to be elucidated, first.

Fig. 6.7(a) illustrates the crystalline core, the inner shell, and the outer shell structure of the FIB-prepared TEM lamella. Such a structure implies that if defects are present in the inner shell, their induced pinning affects the electrostatic potential of the core. In the case of no defects occurring in the inner shell, the midgap pinning at the amorphous-crystalline interface is instead relevant (for details see Chap. 3). This can occur, for instance, if the defects in the defect-rich crystalline inner shell layer are healed (see Fig. 6.7(b)).

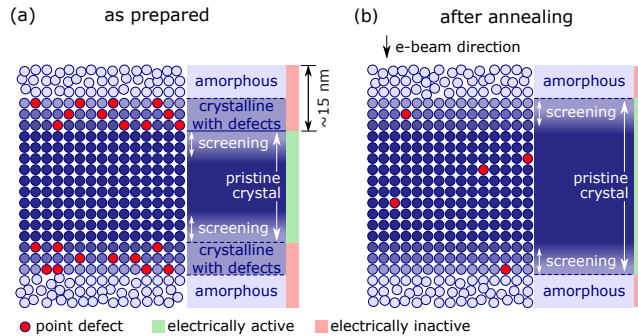


Figure 6.7: Cross-sectional schematic view of the different FIB-induced shell layers of a TEM lamella in the as-prepared (a) and annealed state (b). FIB preparation results in an amorphous shell layer (light blue circles) covering a crystalline core (dark blue circles). In the as-prepared state (a) the crystalline layer directly below the amorphous outer shell (mid blue circles) contains a large concentration of FIB-induced point defects (red circles), leading to a Fermi-level pinning near the valence band and thus a surface potential. This defect-rich inner shell is electrically inactive (red zone). The surface potential is screened by the free charge carriers in the following defect-free pristine crystal region (green zone). (b) After annealing the defects in the defect-rich layer healed, restoring the pristine crystal and only the amorphous outer shell induces a surface potential with midgap Fermi-level pinning. Adapted from K.Ji *et al.* 2024 Appl. Phys. Express 17 016505.[190]

This raises the question of the dominant type of point defect within the defect-rich inner shell. The defect type can be identified using the (i) the pinning level of about 0.6 eV above E_V measured on n -type GaN layer prior to annealing, and (ii) the derived type of charge transfer level: For n -type GaN surface, pinning can only be achieved by a defect that exhibits a charge transfer towards a negative charge state in the bandgap. The simplest one is the (0/-) charge transfer level. Based on these two criteria, different types of point defects are assessed:

First, the intrinsic point defects, i.e. V_{Ga} , V_N , N_i , Ga_i , N_{Ga} , and Ga_N , have

only charge transfer levels involving positive charge states in the lower half of the bandgap (see Fig. 3.7 in Chap. 3).[102, 206] Notably, the V_N suggested previously as the origin of the surface Fermi-level pinning on GaN lamella,[35] has (+/3+) charge transfer level at 0.7 eV, which however cannot pin the Fermi energy for n -type GaN as outlined above.[104] Hence, intrinsic point defects cannot be at the origin of the observed pinning level near E_V in n -type GaN.

Second, extrinsic impurities need to be considered. Oxygen and hydrogen possibly present due to prior air (and water) exposure could be implanted in the course of FIB preparation. However, oxygen in GaN is an n -type dopant and thus cannot induce the observed pinning deep inside the bandgap,[207] while hydrogen has no charge transfer level in the bandgap.[208] Another source of extrinsic impurity stems from the protective layers deposited onto the bulk samples prior to FIB milling process. In the system used in this thesis, this protective layer consists of either platinum or carbon. Hence, contamination from both atomic species is anticipated to be present inside the FIB chamber and could be incorporated into the sample. While little is known about the role of platinum as a point defect in GaN, Pt has been suggested to act as a donor,[209] which conflicts with the observed Fermi-level position.

In contrast, carbon can occupy nitrogen sites (C_N), which are predicted to have the (0/-) charge transfer level ~ 0.8 eV above E_V . [210, 114] This is in good agreement with the observed pinning level of 0.57 eV above E_V . Hence, in view of all other defect levels not exhibiting suitable charge transfer levels and the abundant presence of carbon in the FIB (see below), it can be concluded that the measured surface Fermi-level pinning on TEM lamellas is due to the implanted C_N .

6.3.2 Implantation of C_N by FIB

Building on the previous arguments centered on electrostatics, it has been revealed that C_N is at the origin of surface Fermi-level pinning on FIB-prepared GaN lamella. In this section, it will be demonstrated from the ion/atom interaction perspective that the FIB process can, indeed, lead to the implantation of a substantial amount of carbon inside GaN. Note that in conventional FIB instruments, carbon is always found to be in abundant amount inside the chamber, even if no carbon protective layer is deposited during the FIB process.[211] Major sources of C include the hydrocarbon contamination from exterior as well as the precursors of gas injection system, e.g., even the Pt and W gas sources in the FIB system contain carbon.

The distribution of implanted C as well as recoiled Ga and N in form of vacancies and interstitials into GaN layer is studied using the stopping and range of ions in matter/transport of ions in matter (SRIM/TRIM) software.[101] For the calculation parameters, the host GaN layer is assumed with a thickness of 20 nm. A 2 nm-thick carbon layer is added on top of the GaN layer. Note that the thickness of the carbon layer does not correspond to the much thicker carbon protective layer deposited on the bulk sample prior to lamella cutting. Instead, it resembles a thin carbon film deposited onto the lamella's surface by the electron and ion beams during FIB process. For the incoming Ga^+ ion beam, the same grazing incident angle (5°) and energy (5 kV) have been taken, as those utilized during the final polishing step of the FIB process. To improve the quality of statistics, a total number of 1×10^7 incoming Ga^+ ions are involved during the calculation.

In Fig. 6.8(a), (b), and (c), the calculated distribution of C, recoiled Ga, and recoiled N atoms, are displayed, respectively. The interface between C and GaN layer is indicated by green dotted line. Fig. 6.8(d) depicts the corresponding implantation profiles of recoiled C (black line), N vacancies (red line) and interstitials (green line), as well as Ga vacancies (blue line) and interstitials (purple line), taking the actual FIB ion dose into consideration. It is evident that C recoils sufficiently deep into the subsurface region of the GaN crystal, with a concentration significantly higher than the doping concentration. The distribution of C exhibits an exponential decay into the GaN layer. Note that for the interpretation of the large vacancy and interstitial concentrations, one needs to recall that the simulation does not consider recombination of defects.[101] If recombination is taken into account, most of the N and Ga vacancies will be annihilated already at room temperature in the GaN layer remaining crystalline due to the low diffusion barriers.[104, 105]

On the basis of the calculated carbon implantation profile, it can be concluded that in the underlying crystalline core of GaN lamella, only the exponential tail of the carbon concentration profile is present. At the start of the exponential tail, the carbon concentration is well above the doping concentration, compensating fully the doping and pinning the Fermi-level at the C_N (0/-) charge transfer level. Given the short exponential decay length and the high doping concentration, the pinning takes places only in the near surface region of the crystalline lamella core. Thus the compensating C_N can be reasonably approximated by a surface states, as modeled within the self-consistent electrostatic potential calculation.

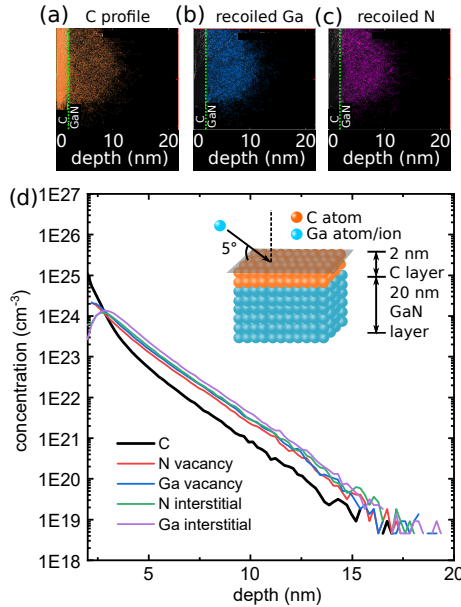


Figure 6.8: (a, b, c) Distribution of C, recoiled Ga, and recoiled N atoms into the GaN, calculated from SRIM/TRIM software.[101] (d) Corresponding implantation profiles, derived using a total Ga⁺ ion dose of 1×10^{17} ion/cm². The sketch on the top right illustrates the geometry of simulated structure.

6.3.3 Discussion of the healing process

Having established that C_N is at the origin of the surface Fermi-level pinning on as FIB-prepared TEM lamellas, in this section, the underlying physics mechanism responsible for the shift of pinning level in the course of annealing will be discussed. Recall that a few physical process can potentially occur during annealing, including thermal ionization of dopants, re-crystallization and melting of material, and healing of point defects:

(i) As a rule of thumb, re-crystallization of the amorphous material takes place at 40% of the melting temperature.[212] With a melting temperature of approximately 2500 °C for bulk GaN,[213] this corresponds to an annealing temperature of 1000 °C, which is two times higher than the maximum temperature reached in the experiment. Hence, a re-crystallization of the amorphous outer shell cannot be responsible for the observed change in the electrostatic properties presented in Fig. 6.5.

(ii) To the first order approximation, the ionization of dopants is only governed by temperature. The free charge carrier concentration at room temperature before and after annealing remains effectively identical. Therefore, the observed shift in E_{pin} before and after annealing cannot be attributed to the thermal ionization of dopants.

(iii) Upon annealing, point defects in the defect-rich inner shell can be anticipated to become mobile, healing/restoring the pristine properties of the semiconductor, as shown schematically in Fig. 6.7(b). Within this framework, the temperature dependence of the pinning level E_{pin} directly reflects to the concentration changes of FIB-implanted point defects in the defect-rich inner shell. Indeed, the thermal-induced healing can lead to an irreversible reduction in C_{N} concentration, eventually falling below the doping concentration. This, in turn, lifts the C_{N} -induced near surface Fermi-level pinning. As a consequence, the pinning level E_{pin} shifts from its C_{N} -induced value close to E_{V} towards a midgap position, arising from the amorphous-crystalline interface.

At this stage, it should be addressed that the healing process of point defects can, in principle, occur through several atomic migration/jump paths (see Chap. 3). For some paths, the charge state of point defects, and thus their electronic properties, maintain unchanged after jump. This can occur, for instance, after a jump of nitrogen atom from a Ga substitutional site N_{Ga} to an interstitial site N_{i} at Fermi-level of ~ 0.5 eV, i.e., $\text{N}_{\text{Ga}}^+ \rightarrow \text{N}_{\text{i}}^+$. [112] On the other hand, extrinsic impurities often undergo a change in their charge states after jump. For example, a carbon atom, initially located as a substitutional impurity on a nitrogen site C_{N} , which carries a single-negative charge at the Fermi-level of approximately 0.8 eV, can jump to an interstitial site C_{i} and acquire a reversed single-positive charge. [108] In the specific case being examined in this chapter, it is reasonable to assume that the electronic characteristics of C_{N} will be altered after the jump processes, as the lamella's surface transits from being predominantly pinned by C_{N} to being pinned by the states at the interface between the amorphous outer shell and crystalline core after annealing.

6.4 Summary

In this chapter, off-axis electron holography is utilized to investigate the surface Fermi-level pinning E_{pin} and its dynamics in the course of annealing. Some of the important conclusions are:

(i) On the basis of the revealed E_{pin} and the direction of band bending, negatively charged carbon substitutional impurities on nitrogen sites C_N , implanted during the FIB process, are identified to be the origin of observed surface Fermi-level pinning on GaN lamellas. The value of $E_{\text{pin}}=0.57\text{ eV}$ for as FIB-prepared TEM lamellas, closely aligns with the (0/-) charge transfer level of C_N . In addition, the presence of a single negatively charged C_N is expected to induce an upward band bending at the surface, which also corroborates with the experimental finding. Furthermore, according to the SRIM/TRIM calculations, it has been revealed that carbon can be implanted as deep as 15 nm into GaN during the FIB process.

(ii) The origin of dynamics of $\Delta\phi_{\text{peak}}$ during in-situ annealing experiments on δ -doped GaN structures has been addressed. After excluding other potential factors that could contribute to variations in phase change during annealing, it is concluded that the observed temperature-dependent dynamics of $\Delta\phi_{\text{peak}}$ are associated with the shift in E_{pin} , which in turn arises from the thermal-induced irreversible healing of C_N . The shift in E_{pin} is found to activate at 250-300 °C, indicating the activation of the C_N healing (see Fig. 6.5(c)). At 400-490 °C, a midgap surface Fermi-level pinning of 1.90 eV is reached, implying a completed transition from pinning dominated by C_N to pinning induced by the amorphous/crystalline interface. This pinning level remains unchanged at this midgap position after cooling-down.

(iii) The thermal-induced irreversible migration of C_N are corroborated with the results from the two-cycle annealing experiment, where the most prominent observation is that $\Delta\phi_{\text{peak}}$ (hence E_{pin}) is found to stay constant before and after the second annealing cycle (see Fig. 6.3(c)).

These findings unravel several important facts: First, they indicate an irreversible healing of FIB-implanted C_N , gradually reducing its concentration upon annealing and subsequently lifting the C_N -induced Fermi-level pinning effect. Second, it is shown that relatively low temperatures, such as 300 °C, are sufficient to initiate defect healing, consequently reducing the width of the FIB-induced defect-rich, electrically inactive inner shell. Moreover, even a short annealing duration (approximately 30 minutes) at 490 °C is adequate for the local concentration of C_N to decrease below the doping concentration, thus restoring the electrical properties of the pristine material. Such post-growth low-temperature annealing steps in the course of opto-electronic device manufacturing can be beneficial to reduce the amount of radiative recombination centers and thus increase the performance of such devices.

In the forthcoming chapter, a novel in-situ experimental setup, with specific emphasis on the temporal evolution of E_{pin} upon annealing, will be introduced. It will demonstrate that with the time-resolved annealing dynamics, the derivation of

relevant parameters and, as a result, the identification of the underlying physical process responsible for the observed healing effect can be accomplished.

Chapter 7

Thermal dynamics of Fermi-level pinning: Substitutional C site switching

7.1 Overview

In the previous chapter, the thermal-induced shift of surface Fermi-level pinning E_{pin} is discussed. In particular, the transition from C-dominant pinning to the pinning arising from the states at the amorphous/crystalline interface is revealed. In this chapter, the results of another in-situ annealing experiment, specifically focusing on the temporal evolution of the E_{pin} , will be discussed. It will be demonstrated that electron holography can be used to identify point defect reactions and quantify their dynamics by probing the time and temperature dependence of the Fermi-level upon annealing.

7.2 Electron holography results

As a model system, lamellas containing a n - n^+ doping step (bulk sample A3162, for details see Chap. 2) will be used. The doping levels in the n and n^+ GaN are $8 \times 10^{17} \text{ cm}^{-3}$ and $3.5 \times 10^{18} \text{ cm}^{-3}$, respectively, as determined by SIMS. Note that the experimental details remain generally the same with those carried out in the previous Chap. 6. The only difference is that all holograms presented in this chapter are acquired at room temperature.

Figure 7.1 displays an overview of phase maps extracted from the n - n^+ GaN doping step for as FIB-prepared TEM lamellas before annealing and after a certain

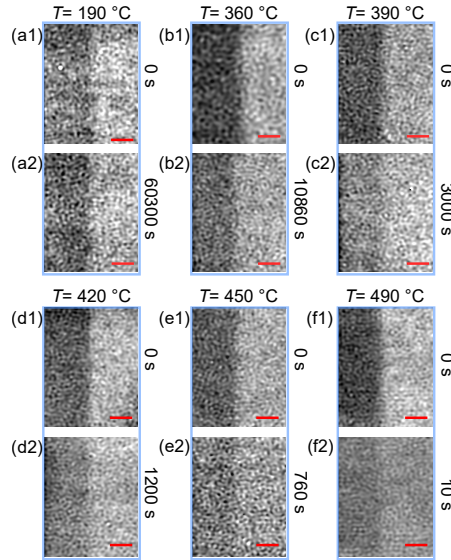


Figure 7.1: Overview of phase maps extracted from the n - n^+ GaN junction before annealing and after extended annealing for different annealing temperatures. The scale bars correspond to a distance of 50 nm.

annealing time, for various annealing temperatures. The growth direction [0001] points from left to right and the n -doped layer exhibits a darker contrast compared to the adjacent n^+ -doped layer. Figure (a1) and (a2) illustrate the phase maps acquired at the lowest annealing temperature, i.e., $T=190^\circ\text{C}$. It can be observed that even after an extended annealing time of approximately 17 hours, the phase contrast across the doping step remains effectively unchanged. Note that the grey scale is the same for Fig. 7.1(a1) and (a2).

In contrast, at higher annealing temperatures (depicted in Fig. 7.1(b)-(f)), the phase contrast decreases after a certain annealing time. At higher annealing temperatures, the decrease in phase contrast takes place faster and thus the annealing time can be progressively reduced. In particular, at the highest annealing temperature of 490°C , the phase contrast rapidly reduces and stabilize within 10 s. It is important to note that the temperature ramping time from the room temperature to 490°C takes approximately 140 s. Therefore, the observed reduction and stabilization of phase contrast can be expected to occur even before reaching 490°C . Thus, only data acquired under annealing temperature of 360°C , 390°C , 420°C , and 450°C are subjected to the subsequent analysis.

Next, I focus on the quantitative evolution of electron optical phase map across the n - n^+ GaN junction during annealing: Fig. 7.2(a) illustrates the evolution of phase maps upon annealing at 420° C. It can be observed that the phase contrast between n and n^+ GaN layers reduces with annealing time. To quantify these changes induced by annealing, phase profiles from measured electron optical phase maps averaged over a width of 400 nm are extracted. Figure 7.2(b) depicts examples of the derived phase profiles (symbols) acquired after successive annealing at 420° C for different times. Before annealing, in the as FIB-prepared state, the lateral change of the phase across the n - n^+ GaN junction has the shape of a broadened step function with a height, i.e., phase step $\Delta\phi_{\text{junction}}$ of 0.37 rad (see Fig. 7.2(a)). Upon annealing $\Delta\phi_{\text{junction}}$ becomes smaller, reducing to 0.26 rad after 120 s and finally to 0.17 rad after 960 s annealing. Additional annealing does not result in a further change of $\Delta\phi_{\text{junction}}$ anymore, suggesting that the healing process is terminated.

For a quantitative understanding of the decrease in $\Delta\phi_{\text{junction}}$ with annealing, a self-consistent electrostatic simulation of the phase across the junction is carried out, as described in Chap. 3 and in Ref.[190, 35] The calculated electrostatic potential is used to derive the phase profiles across the n - n^+ GaN junction for different E_{pin} . The green dashed line in Fig. 7.2(b) yields the phase profile calculated for a TEM lamella without surface pinning (i.e., being unpinned). The "unpinned" phase step is smaller than any of the measured ones at any annealing stage. Hence, the TEM lamella cannot be unpinned near its surfaces. The best-fitting simulation results for the as-prepared and fully healed TEM lamellas are shown as solid lines in Fig. 7.2(b). Note, the surface Fermi-level pinning-increased phase step across the junction is due to the doping level dependent screening length of the near surface electrostatic potential (induced by the pinning), as described in detail in Chap. 5 and in Ref.[190, 35]

The simulation yields the following Fermi-level pinnings: (i) In the as FIB-prepared state, an averaged surface Fermi-level pinning of $E_{\text{pin}}=(0.57 \pm 0.13)$ eV above the valence band edge (E_V) is found. This pinning level value is consistent with previous experimental values and is compatible only with the (0/-) charge transfer level of carbon substitutionals on nitrogen sites (C_N)[190] which has been calculated to be around 0.8 eV above E_V . [210, 114, 214, 215, 216] All other intrinsic defects[104, 112] and possible FIB-implanted impurities (e.g., Pt[209]), as well as carbon-related complex defects[114, 217], do not exhibit appropriate acceptor-type charge transfer levels in the vicinity of the measured Fermi-level pinning energy.

(ii) After termination of the thermal healing process (e.g., 960 s and longer annealing) the pinning level increases to $E_V+(2.14 \pm 0.09)$ eV. This midgap pinning level is attributed to the states present at the amorphous shell-crystalline core interface

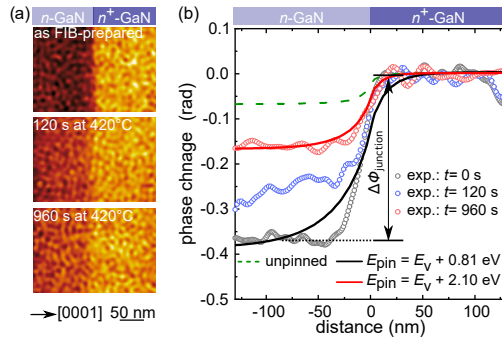


Figure 7.2: (a) Electron optical phase maps of the n - n^+ GaN junction measured by electron holography in TEM. The top figure illustrates the phase distribution of an as FIB-prepared TEM lamella, whereas the middle and bottom figures were acquired after annealing at 420°C for 120 s and 960 s, respectively. (b) Corresponding line profiles revealing the change of the electron optical phase across the n - n^+ GaN junction upon annealing at 420°C (open symbols). The junction interface is located at 0 nm spatial position. The lines represent simulations of the phase profile for different pinning levels at the surface of the TEM lamella. The lowest pinning level in the as FIB-prepared state is attributed to FIB-implanted C_N , whereas the higher one after annealing arises from the states at the amorphous-crystalline interface near the surface of the TEM lamella.

of the TEM lamella.[190, 35] Continued annealing does not result in any further increase in E_{pin} (see Chap. 6).

7.3 Data analysis

7.3.1 Time constant analysis

At this stage, the temporal evolution of $\Delta\phi_{\text{junction}}$ upon annealing is quantified further: Fig 7.3(a) illustrates the decay of $\Delta\phi_{\text{junction}}$ versus annealing time t for four lamellas, each subjected to a different annealing temperature T (colored symbols). For all data sets, the phase step is between 0.37 and 0.45 rad in the as FIB-prepared state. Annealing leads to an exponential decay of $\Delta\phi_{\text{junction}}$, which approaches asymptotically a saturation value, ranging between 0.15 and 0.18 rad. The time required to reach the saturation value strongly decreases with temperature. The time dependence of $\Delta\phi_{\text{junction}}$ can be described in first approximation by an exponential decay:

$$\Delta\phi_{\text{junction}}(t, T) = \Delta\phi_0 \cdot \exp\left(-\frac{t}{\tau(T)}\right) + \Delta\phi_{\infty} \quad (7.1)$$

where $\Delta\phi_{\infty}$ is the saturation value after complete healing, and $\Delta\phi_0 + \Delta\phi_{\infty}$ is the phase step at the junction in the as FIB-prepared state. $\tau(T)$ is the temperature-dependent time constant of the healing process. For each temperature, an exponential fit of measured $\Delta\phi_{\text{junction}}(t)$ values is shown as solid line in Fig 7.3. For data sets acquired at 420 °C and 450 °C enlarged insets are added for better visibility of the decay. The physically most relevant parameter is the time constant $\tau(T)$. Table 7.1 provides the values of $\tau(T)$ obtained for different annealing temperatures. Notably, to account for the temperature ramping time, 40 s are added to the lower error of the time constant.

T (°C)	time constant τ (s)
360	5308^{+1483}_{-1443}
390	912^{+197}_{-157}
420	147^{+68}_{-28}
450	18^{+44}_{-4}

Table 7.1: Time constant (τ) obtained from the exponential fit to the electron optical phase step across the n - n^+ GaN junctions for different annealing temperatures.

In order to identify the time constants' physical background, the decay of $\Delta\phi_{\text{junction}}$ is related with the surface Fermi-level pinning. For this purpose, all phase profiles are simulated, using the methodology described in Chap. 3. Figure 7.3(b) illustrates the evolution of the derived pinning levels as a function of time and temperature. The values reveal an exponential convergence from pinning levels of $E_V + (0.57 \pm 0.13)$ eV towards $E_V + (2.14 \pm 0.09)$ eV after extended annealing.

It is recalled that the lower pinning value is assigned to C_N defects implanted during FIB preparation, whereas the higher pinning level is assigned to the presence of states at the interface between the amorphous outer shell and the crystalline core, see Chap. 3 and Ref.[190] The latter cannot be healed thermally at the low temperatures used and remains even after healing.

7.3.2 Derivation of activation barrier and diffusion length

C_N defects pin the Fermi-level if their concentration is sufficiently above the doping concentration. Lowering the C_N concentration will gradually shift the pinning from being C_N dominated to being dominated by the states at the amorphous/crystalline interface. Hence, the shift in pinning levels reflects the reduction of the concentration of C_N . As a first approximation, this reduction in C_N concentration can be described as a thermal migration process. Once the C_N concentration is sufficiently below the doping concentration, carbon becomes electrically irrelevant. Therefore, the time constant $\tau(T)$ of the $\Delta\phi_{\text{junction}}$ decay reflects the time needed to reduce the C_N concentration sufficiently below the doping concentration. Since exactly the same FIB preparation procedure is applied to prepare TEM lamellas, it can be expected that a consistent C implantation depth and, concentration is present in each lamella. Thus, the diffusion length L , required for electrically insignificant C_N concentration can be anticipated to be a constant and temperature independent value given by

$$L = \sqrt{D(T) \cdot \tau(T)} = \text{const.} \quad (7.2)$$

$D(T)$ is a temperature dependent diffusion coefficient[104] defined by

$$D(T) = D_0 \cdot \exp\left(-\frac{E_b}{k_B T}\right) \quad (7.3)$$

where D_0 is the pre-exponential factor dependent on geometry and crystal structure. E_b is the activation barrier energy and k_B is the Boltzmann constant. Inserting

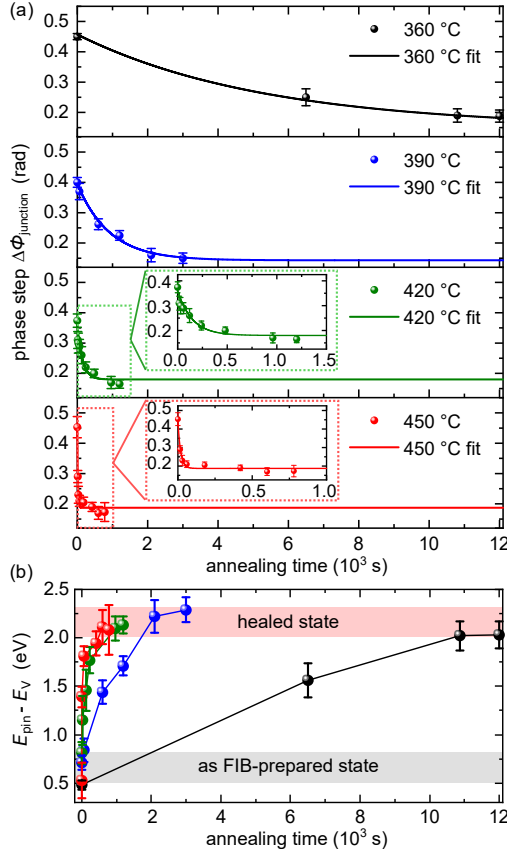


Figure 7.3: (a) Time evolution of the phase step $\Delta\phi_{\text{junction}}$ across the n - n^+ GaN junction for different annealing temperatures. (b) Derived pinning levels of the Fermi energy at the surface of the TEM lamellas versus annealing time. The data reveals a shift of the average pinning from $E_V + (0.57 \pm 0.13)$ eV, attributed to carbon impurities on nitrogen sites (as FIB-prepared state), to $E_V + (2.14 \pm 0.09)$ eV, attributed to the states at the amorphous outer shell-crystalline core interface (healed state).

Eq. (7.3) into Eq. (7.2) yields an Arrhenius equation:

$$\ln\left(\frac{1}{\tau}\right) = \ln\left(\frac{D_0}{L^2}\right) - \left(\frac{E_b}{k_B}\right) \cdot \frac{1}{T}. \quad (7.4)$$

Figure 7.4 depicts the logarithm of the inverse time constant $1/\tau$ derived from the exponential decay of $\Delta\phi_{\text{junction}}$ in Fig. 7.3(a) versus inverse temperature ($1/T$). The data exhibits a linear relation in accordance with Eq. (7.4). The slope of the linear fit (blue line) yields an activation barrier energy $E_b = 2.27 \pm 0.26$ eV.

The intercept of the Arrhenius plot is found to be

$$\ln(D_0/L^2) = (32.9 \pm 4.5) \ln(1/\text{s}). \quad (7.5)$$

According to Eq. (7.4) the intercept is related to the diffusion length L . The pre-exponential factor D_0 is given by $g \cdot a^2 \cdot \nu$, where a is the (in-plane) lattice constant, ν the attempt frequency, and g the geometry factor.[104] The geometry factor depends on the crystal structure and exact diffusion path(s) and can be approximated to be in the order of one.[218] The attempt frequency is approximated by the frequency, where the phonons of nitrogen atoms have the highest density of states, i.e., $\sim 1.6 \times 10^{13} \text{ s}^{-1}$. [219] Using these values, a diffusion length after a time of 3τ (at which full healing is achieved) of $(0.28_{-0.25}^{+2.40}) \times a$ is obtained. This points to a single atomic jump process being responsible for lifting the Fermi-level pinning induced by C_N .

Note that when a single atomic site switch instead of macroscopic diffusion process takes place, Eq. (7.4) can also be derived from the corresponding rate equations: The switching rate of carbon from substitutional to another site, $\frac{dc_s(t)}{dt}$, is proportional to the substitutional carbon concentration $c_s(t)$, the attempt frequency ν , the number of equivalent neighboring sites in the crystal lattice N , and the Boltzmann factor:

$$\frac{dc_s(t)}{dt} = -c_s(t) \cdot N \cdot \nu \cdot e^{-E_b/(k_B T)}. \quad (7.6)$$

This first order differential equation can be solved by using an exponential decay as an ansatz:

$$c_s(t) = c_s(0) \cdot e^{-t/\tau} \quad (7.7)$$

yielding:

$$1/\tau = N \cdot \nu \cdot e^{-E_b/(k_B T)} \quad (7.8)$$

which is equivalent to Eq. (7.4) if $N = g \cdot a^2/L^2$.

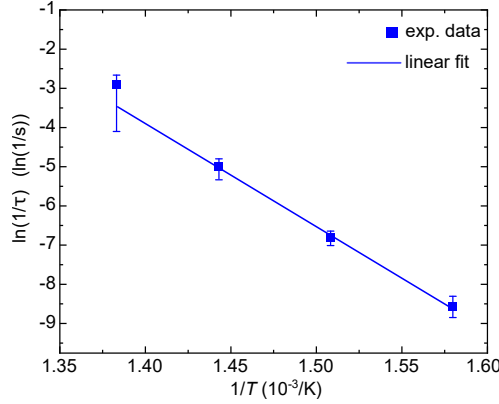


Figure 7.4: Arrhenius plot of the measured $\ln(1/\tau)$ values versus $1/T$. The line represents a linear fit according to Eq. (7.4). The slope yields an activation barrier energy $E_b=2.27\pm 0.26$ eV.

7.4 Discussion

To understand the measured activation barrier energy and small diffusion length, the atomic mechanisms related to carbon point defects during annealing needs to be addressed. Before annealing the surface of the as FIB-prepared lamella is pinned at $\sim E_V+0.57$ eV, which is attributed to the singly negatively charged C_N^- (see Chap. 3, 6, and Ref.[190] for details). During annealing this pinning level vanishes, reducing the downward shift of the FIB-induced surface potential. One possible explanation for this behaviour would be the diffusion of C_N^- from the surface towards the crystalline bulk and/or the amorphous outer shell, effectively reducing the C_N^- concentration below the doping concentration.

C_N^- diffusion can be realized via nitrogen vacancies. The nitrogen vacancy has, however, a rather high migration barrier of ~ 4 eV for the $+1e$ charge state at the given Fermi-level position.[104, 105] Thus, vacancy mediated migration of substitutional C can be ruled out.

Alternatively, diffusion can take place through carbon interstitials, which can be created by atomic kick-out or a switching process. The activation barrier energy for this diffusion process has been calculated to be strongly affected by the charge state of C_i . [105] In particular, C_i^+ and neutral C_i exhibit higher activation barrier energies of 2.4 eV and 3.0 eV, respectively. Hence, as the surface Fermi-level increases, the diffusion of C_i becomes less likely. In addition, the Coulomb interaction between

the negatively charged C_N^- and the positively charged C_i^{2+} further reduces the diffusion probability.

However, interstitial diffusion is actually not needed for lifting the Fermi-level pinning near the valence band edge, since with a substitutional to interstitial site switch of C, the presence of (0/-) charge transfer levels in the lower part of the bandgap vanish (C_i have no such charge transfer levels): Upon site switch from the substitutional onto an interstitial site the charge of carbon changes from negative to positive[105] and thereby carbon becomes electrically inactive already (for n -type GaN and in presence of a further midgap pinning, e.g., at the amorphous-crystalline interface). In addition once switched, the positively charged C_i experiences a repulsive Coulomb interaction with the newly formed positively charged N vacancy, effectively blocking a back jump. Hence, a single site switch is sufficient.

This is in-line with the measurements: First, classical carbon outdiffusion would require a diffusion length well above 10 nm since the C implantation profile at the given energy is expected to have a width of ~ 15 nm.[190] Therefore, the experimentally obtained diffusion length in the order of one atomic jump distance contradicts to the diffusion process. Instead the short diffusion length is rather consistent with a C site switching process. Therefore, the experimentally obtained activation barrier energy of 2.27 ± 0.26 eV is attributed to the energy barrier of the carbon site switching process.

A transformation of C_N into C-related defect complexes would also reduce the pinning, due to the absence of suitable acceptor-like states in the lower part of the bandgap for C-defect complexes.[214, 215, 115] This transformation can be anticipated to require, however, complex atomic reactions with several correlated jump processes, which lead to larger migration barrier energy. Hence, it is rather unlikely that such complex processes can occur at given low annealing temperatures.

On the basis of the above results, one can estimate the thermal stability of C-doped semi-insulating GaN layers in, e.g., HEMTs, since the C site switch would remove the deep level in the lower part of the bandgap responsible for achieving insulating properties. It can be anticipated that continuous operation at a maximum temperature of approximately 220° C can be sustained over a 20-year period.

7.5 Summary

In this chapter, the temporal evolution of FIB-implanted C point defects in GaN upon annealing is quantified by probing the Fermi-level changes using off-axis elec-

tron holography. It has been revealed that the switching of C from substitutional to interstitial sites is the atomic process responsible for lifting the Fermi-level pinning in the lower part of the bandgap and hence for removing the semi-insulating properties of C-doped GaN insulating layers. This process has an activation barrier energy of 2.27 ± 0.26 eV.

Chapter 8

A demonstration on quantification of phase map: Case of (Al,In)N/GaN interface

8.1 Overview

In this chapter, the GaN/(Al,In)N/GaN heterostructure is selected as the exemplary material system to illustrate the quantification of electrostatic potential as well as polarization changes from measured phase map. The content is structured as follows: First, a comprehensive characterization on lamella properties is performed, including phase change maps, lamella crystalline thickness, strain, and chemical composition. Second, a self-consistent electrostatic potential calculation is conducted, with the inputs derived from these measured parameters. Finally, the calculated result is compared with the experimental phase change profile.

8.2 Results

8.2.1 Electron holography

Off-axis electron holography is carried out to extract the phase map across a GaN/(Al,In)N/GaN heterostructure #2 (from bulk sample A3162, for details see Chap. 2). The corresponding phase map is displayed in Fig. 8.1. The [0001] growth direction points from left to right. The green dotted lines indicate the positions of the interfaces between the GaN and (Al,In)N layers. For the sake of clarity, the interface closer to the substrate is referred to as the *lower* interface, while the

reversed interface is labelled as the *upper* interface. The extracted phase profile (yellow solid line) is overlaid on the phase map. Note that the central (Al,In)N layer exhibits a darker contrast, while the adjacent GaN layers display brighter contrast. This different contrast is primarily attributed to the difference in mean inner potentials V_{MIP} of these two layers.

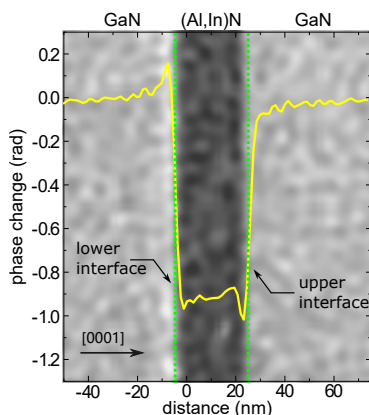


Figure 8.1: Phase map acquired across the (Al,In)N/GaN heterostructure. The phase change profile (yellow line) averaged over a width of 750 nm is overlaid. Two types of interfaces are marked with green dotted lines: The interface closer to the substrate is denoted as the lower interface, while the opposite interface is the upper interface. Peaks in phase only occur near the interfaces.

Both lower and upper interfaces turn out to give rise to different phase changes. The lower interface exhibits a thin bright line, manifesting as a peak in the phase profile on the GaN side of the interface. In contrast, a negative peak appears on the (Al,In)N side near the upper interface. Within the (Al,In)N layer, the phase change is otherwise constant along the growth direction.

8.2.2 High resolution STEM

Strain

The local lattice constants of (Al,In)N and GaN layers are determined utilizing the peak pairing analysis (PPA) method in atomic-resolved HAADF images. In the course of HAADF measurements, lamella is oriented carefully such that the electron beam is parallel to the $[10\bar{1}0]$ zone axis.

Fig. 8.2(a) and (b) depict exemplary atomic-resolved HAADF images acquired from the GaN and (Al,In)N layers, respectively. The growth direction $[0001]$ points from top to bottom. In the top right corner of Fig. 8.2(a), a schematic ball-stick atomic model of GaN is overlaid. The big green and small grey spheres correspond to the gallium and nitrogen atoms, respectively. In Fig. 8.2(a), all atomic columns exhibit the same contrast in line with a pure binary alloy: Peaks correspond to gallium atom columns. The nitrogen atom column is invisible due to its lower atomic number Z compared to gallium. In contrast, Fig. 8.2(b) depicts the HAADF image acquired within the (Al,In)N layer, where the contrast of atomic columns fluctuates: Peaks with brighter contrast represent atomic columns with higher indium fractions, while peaks with a darker contrast correspond to atomic columns with higher aluminum fractions, as denoted with white dotted circles. The Gaussian center of each atomic column is determined with the help of the peak pairing analysis function embedded in the Atomap script.[73] The lattice constants c and a are measured as the separation between two neighboring intensity peaks along the $[0001]$ and $[1\bar{2}10]$ direction, respectively, as indicated with green dotted lines in Fig. 8.2(a). The lattice constants measured on the GaN substrate are utilized as the unstrained reference to calibrate potential distortion or scaling effect from the microscope.

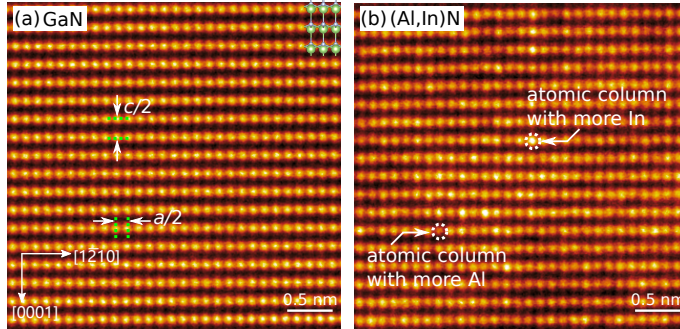


Figure 8.2: Atomic resolution HAADF images acquired on (a) the GaN layer and (b) the (Al,In)N layer. In (a), all atomic columns exhibit the same contrast: Peaks with bright contrast correspond to atomic columns of Ga and N is invisible. A GaN atomic model is overlaid on the top right. The green spheres represent gallium atoms while the grey ones are nitrogen atoms. In (b), the atomic columns exhibit contrast fluctuation. The brighter and darker peaks represent atomic columns with more In and Al, respectively. The separations between two neighboring intensity peaks correspond to the half of the lattice constant c and a , respectively.

Fig. 8.3 illustrates the measured lattice constants c and a in the vicinity of interfaces between (Al,In)N and GaN layer. Each data point has been derived by averaging results from at least 3 HAADF images acquired at the same region. The error bars correspond to one standard deviation. For each layer, the corresponding unstrained lattice constants a and c are indicated as horizontal black and red lines, respectively. The unstrained lattice constants of the ternary (Al,In)N layer are interpolated from its binary constituents' values, utilizing Vegard's law.[220] Within the GaN layer, both lattice constants a (black data point) and c (red data point) are found to be in close proximity to the unstrained values, within the precision of measurement. In the case of the ternary (Al,In)N layer, the lattice constant a is found to be nearly identical to the value of the adjacent GaN layer, while the lattice constant c is slightly smaller than that of the GaN layer.

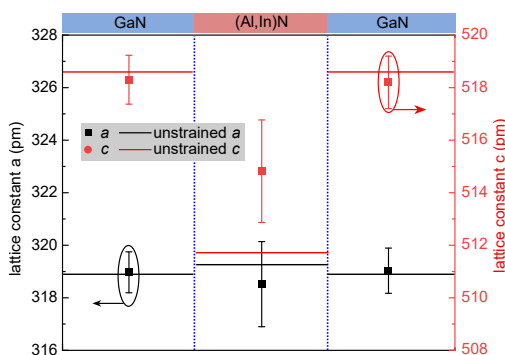


Figure 8.3: Lattice constants measured near the (Al,In)N and GaN interfaces, derived from the atomic column separations measured in HAADF images. The solid lines are the indications of unstrained lattice constants. The GaN layers are effectively unstrained while the (Al,In)N layer is biaxially strained.

To derive the corresponding strain values from measured lattice constants, one needs to compare them with unstrained lattice constants. Notably, the GaN layers are effectively unstrained with averaged strain components of $\varepsilon_{xx}=0.04\pm0.27\%$ and $\varepsilon_{zz}=-0.06\pm0.17\%$ along $[1\bar{2}10]$ and $[0001]$ direction, respectively. In contrast, the lattice of (Al,In)N layer is primarily elongated in $[0001]$ i.e., c direction. Strain values of $\varepsilon_{xx}=-0.22\pm0.5\%$ and $\varepsilon_{zz}=0.61\pm0.38\%$ are unraveled along a and c direction, respectively. Therefore, the ternary (Al,In)N layer undergoes a biaxial strain. Note that for the investigated wurtzite structure $\varepsilon_{xx}=\varepsilon_{yy}$.

The PPA method offers a precise determination of strain but is limited to localized regions. To examine strain across the heterostructures on a larger scale, geometric phase analysis (GPA) is carried out on HAADF images acquired with a larger FOV

of $46\text{ nm} \times 46\text{ nm}$, as shown in Fig. 8.4(a). The GaN layer closer to the substrate is chosen as the unstrained reference. Note that the lattice fringes are still clearly visible at this magnification.

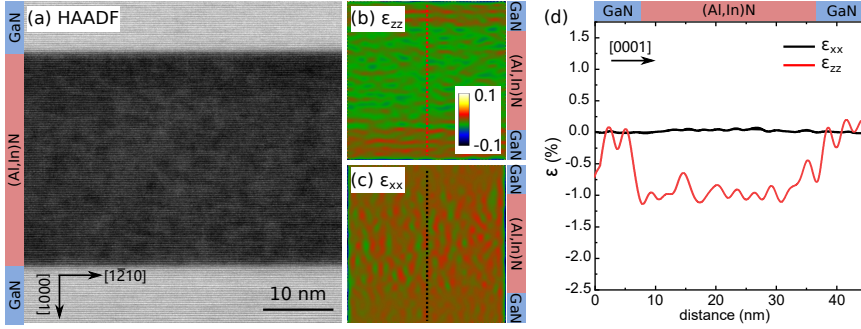


Figure 8.4: (a) HAADF image of GaN/(Al,In)N/GaN heterostructure acquired at a low magnification. Strain maps of (b) ϵ_{zz} and (c) ϵ_{xx} are derived by GPA method on (a). The red and black dotted lines mark the extraction regions for line profiles plotted in (d), respectively. These line profiles are averaged over a 45 nm width.

Figure 8.4(b) and (c) illustrate mappings of strain ϵ_{zz} along [0001] direction and ϵ_{xx} along [1210] direction, as derived from GPA method, respectively. The contrast scale is adjusted such that the compressively strained region appears in a green-bluish color, and conversely, the tensile-strained region is represented with a reddish color. The dotted colored lines indicate the position of line profiles plotted in Fig. 8.4(d). From the ϵ_{zz} map (Fig. 8.4 (b)), one can observe that the GaN and (Al,In)N layers appear to exhibit distinct contrast. This observation is well reflected in Fig. 8.4(d): Within the (Al,In)N layer, an average $\epsilon_{zz} = 0.8\%$ (red line) relative to the adjacent GaN layer is revealed. On the other hand, the lattice-matched condition between the ternary (Al,In)N and GaN layers can be corroborated from the ϵ_{xx} map. The corresponding ϵ_{xx} line profile (black line in Fig. 8.4(d)) remains constant at $\sim 0\%$ throughout the heterostructure. These findings are highly consistent with the results analyzed with PPA method.

Chemical composition mapping

The EDX measurement is carried out within a STEM. Each pixel in the HAADF image contains a corresponding EDX spectrum. The averaged EDX spectrum acquired from the GaN and (Al,In)N layers are depicted in Fig. 8.5(a) and (b), re-

spectively. The X-ray intensity of corresponding constituent elements can be clearly distinguished. The Cu-K line originates from X-rays emitted from the TEM copper grid.

The quantitative analysis of EDX spectra has been discussed in Chap. 2. Here, I briefly recall some essential parameters involved in the quantification process utilizing the spectrum acquired from (Al,In)N as an example. These parameters are listed in Tab. 8.1. The X-ray intensity of Al-K line and In-L line is obtained by integrating the full-width Gaussian peak. The K factor and absorption correction factors are calibrated with a reference sample. The resulting quantitative atomic fractions are close to the nominal composition of the ternary (Al,In)N layer, as measured from X-ray diffraction.

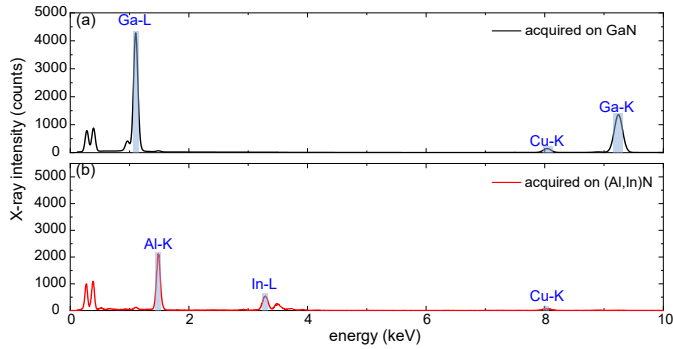


Figure 8.5: Averaged EDX spectrum acquired from the GaN layer (a) and (Al,In)N layer (b).

Element	Intensity (counts)	K factor	Abs. correction	Wt. fract.	Atomic fract.
Al-K	8406	1.00	1.26	0.539	0.815
In-L	5163	1.52	1.16	0.461	0.185

Table 8.1: Quantitative chemical information of the (Al,In)N layer extracted from EDX measurement.

Next, I turn to the quantitative chemical composition mapping across the GaN/(Al,In)N/GaN heterostructure as depicted in Fig. 8.6. Figure 8.6(a) displays the HAADF image of the heterostructure, including a (Al,In)N layer with darker contrast and surrounding brighter GaN layers. The growth direction [0001] points from top to bottom. Quantitative elemental maps of aluminum, gallium, and indium are shown in Fig. 8.6(b), (c) and (d), respectively. The x-ray intensity counts of Al, Ga, and In are calculated based on the 1.49 keV (K-line), 9.25 keV (K-line), and

3.29 keV (L-line) peaks, respectively. The white dotted rectangle represents the position where profiles in Fig. 8.6(e) are extracted. In Fig. 8.6(e), a comparison of profiles obtained from the Al map (red line) and In map (blue line) is presented. At both upper and lower interfaces, a transition region of about 4 nm is found. Within the (Al,In)N layer, a composition gradient is revealed. In particular, the indium concentration rises gradually from 16% at lower interface to the nominal concentration of 19% at the upper interface. Accordingly, the aluminum concentration decreases from 84% to 81%.

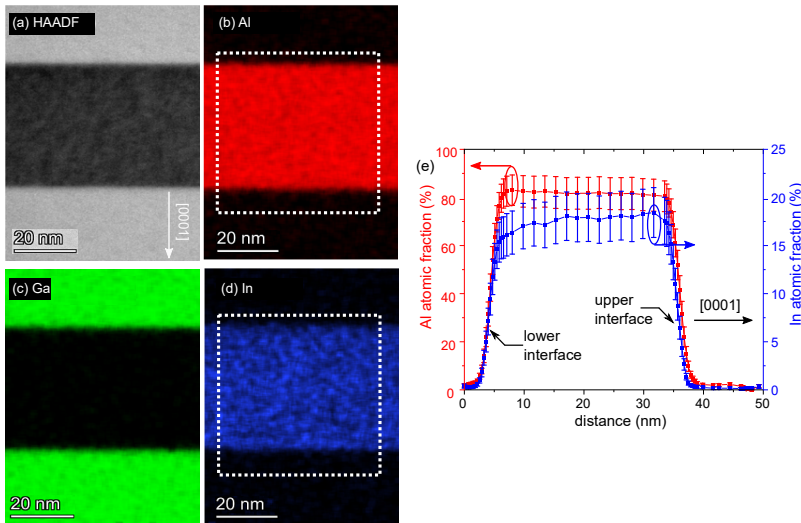


Figure 8.6: (a) HAADF image representing the region for EDX investigation. (b), (c), and (d) are the software-generated element maps of aluminum, gallium, and indium, respectively. The white dot rectangle represents the positions of profiles shown in (e) where a composition gradient is unraveled inside the (Al,In)N layer.

Crystalline thickness determination

The crystalline thickness of lamella is determined using the CBED technique. Fig. 8.7 depicts the CBED disks (0000) and (0006) of the GaN layer, obtained under the two-beam condition. In the (0006) disk, the brightest fringe (highlighted by the red dotted line) is at the exact Bragg condition without excitation error (i.e., $s=0$). The spacing between fringes corresponds to the scattering angles θ of transmitted electrons (for details see Chap. 2).

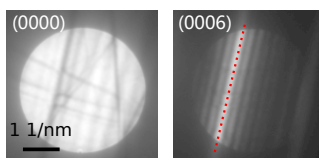


Figure 8.7: (0000) and (0006) disks acquired under the two-beam condition for crystalline thickness determination.

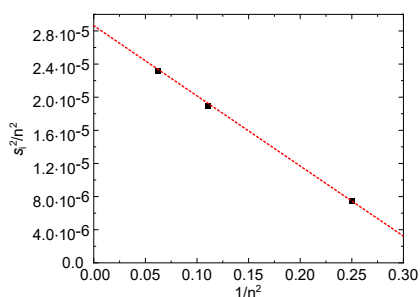


Figure 8.8: A plot of $\frac{s_i^2}{n^2}$ against $\frac{1}{n^2}$. The red dotted line represents the best linear fitting. The thickness is 187.8 nm, as derived from the intercept. The corresponding extinction distance is calculated as 109.2 nm.

The crystalline thickness is derived using the analysis method discussed in Chap. 2. Fig. 8.8 displays a plot of $\frac{s_i^2}{n^2}$ versus $\frac{1}{n^2}$. Spacings between central bright and 3 dark fringes in (0006) disk are chosen, the best linear fitting (red dotted line) is realized by assigning the fitting parameter $n=2$. The intercept of the fit on the y axis is 2.83×10^{-5} which corresponds to a crystalline thickness of 187.8 nm. The slope of the line is -8.38×10^{-5} which implies a extinction distance ε_g of 109.2 nm. It should be noted that CBED measures the crystalline thickness only, and by utilizing SEM, the overall thickness of the same lamella is measured as 210 nm, which indicates that an amorphous layer of 11 nm is formed on the surface of lamella. A repetition of this measurement at different regions of the lamella unravels an uncertainty of the crystalline thickness of 6 nm. Such a small fluctuation in the thickness suggests that the lamella is rather flat.

8.3 Self-consistent electrostatic potential calculation

8.3.1 Relevant fixed parameters

The following parameters are used as fixed values in the self consistent electrostatic potential calculations.

(i) The Fermi-level of the lamella surface is pinned by the FIB-induced carbon substitutional on nitrogen sites C_N , as discussed in Chap. 6 and in Ref.[190]. The pinning level serves as calibration for further self-consistent electrostatic potential calculations and needs to be determined first. For the investigated lamella, a surface pinning of 0.69 ± 0.20 eV above the valence band edge is determined using a doping structure in GaN in the same lamella.

The question is if this surface Fermi-level pinning energy can be applied to the adjacent (Al,In)N layers too. Indeed, calculations of C_N in the binary III-nitride compounds (i.e., GaN, InN, and AlN) reveal that the (0/-) charge transfer level aligns in all compounds with 0.2 eV relative to the vacuum energy.[108] Hence, it is reasonable to assume that in the same lamella, the surface of ternary (Al,In)N layer is also pinned at 0.69 ± 0.20 eV above E_V .

(ii) The bandgap energy E_g of effectively unstrained GaN layer is taken as 3.40 eV, as suggested from literature.[221] To determine the E_g of the biaxially strained (Al,In)N layer, the unstrained E_g must be determined first. This unstrained value is obtained through interpolation from the values of the constituent binary compounds, i.e., InN and AlN, with values of 0.60 and 6.21 eV, respectively.[222, 223] The bowing effect is considered following the methodology introduced by Pela *et al.*[150] The influence of the strain on E_g is computed using the Eq.(3.45) and (3.46) discussed in Chap. 3.[146]

The theoretical deformation potentials along with the derived strained bandgap energy are listed in Tab. 8.2. Again, the composition of (Al,In)N layer is considered to be the nominal one. The strained bandgap of GaN and (Al,In)N is found to be ~ 3.39 eV and ~ 4.48 eV, respectively.

layer	$a_{cz} - D_1$	$a_{ct} - D_2$	D_3	D_4	$E_g^{\text{unstrained}}$ (eV)	E_g^{strained} (eV)
GaN	-6.07	-8.88	5.38	-2.69	3.40	3.39 ± 0.06
$\text{Al}_{0.81}\text{In}_{0.19}\text{N}$	-4.22	-10.87	7.94	-3.35	4.50	4.48 ± 0.13

Table 8.2: Bandgap energy for strained GaN and (Al,In)N layers.

(iii) The electron affinity χ of the GaN and the nominal $\text{Al}_{0.81}\text{In}_{0.19}\text{N}$ layer under unstrained condition are 4.1 and 3.5 eV, respectively (see details in Chap. 3). The strain-induced change in χ can be considered as the shift in conduction band edge. Here, it is assumed that the change in E_g for the (Al,In)N (GaN) layer is distributed with a ratio of 1:6 (1:3) on the valence and conduction band edge, respectively. Thereby, the χ for (Al,In)N and GaN layers, taking actual measured strain into consideration, are 3.48 ± 0.11 and 4.1 ± 0.05 eV, respectively.

8.3.2 Effect of mean inner potential

The self-consistent electrostatic potential calculations across GaN/(Al,In)N/GaN heterostructure are first performed under the assumption of a homogeneous (Al,In)N with a nominal composition of $c(\text{In})=19\%$. The sign convention is such that a negative polarization difference leads to a positive sheet charge, thus forming a local minimum at the electrostatic potential (hence a maximum in phase change). The donor concentration in (Al,In)N layers is assumed to be identical to the value of adjacent GaN layer (i.e., $8 \times 10^{17} \text{ cm}^{-3}$).

It can be anticipated that the difference in V_{MIP} of the GaN and the (Al,In)N layers is the primary contribution to the measured phase change profile. The expected mean inner potential V_{MIP} for the GaN and (Al,In)N layers are calculated following Eq. (3.47) and (3.48) in Chap. 3: The unstrained values of nitride binaries are adopted from literature.[176] The V_{MIP} is assumed to be inversely proportional to the volume of the unit cell. Thereby, the resulting V_{MIP} of the GaN and (Al,In)N layer, taking measured strain into consideration, are calculated as 16.89 ± 0.12 and 16.42 ± 0.23 V, respectively, i.e., a difference of 0.47 V.

Figure 8.9 depicts the comparison between measured phase change profile (black line and symbols) and profiles calculated using theoretically expected V_{MIP} difference between the GaN and (Al,In)N layers, without (with) considering strain effect, of values of 0.44 V (0.47 V), as displayed with blue (green) line. Notably, both simulated profiles exhibit large discrepancy to the measurement. The strain effect reflects as an increment of only 0.04 rad.

The inconsistency of the V_{MIP} may be related to the uncertainty in the actual modelling of the electron density applied in the literature,[176] i.e., whether using the local density approximation (LDA) or the generalized gradient approximation (GGA). Different models can indeed yield different lattice constants, hence leading to different V_{MIP} . For instance in Ref. [176], the authors calculated the V_{MIP} for CdO using both LDA and GGA models. The former yields a value of 17.26 V, while the

latter results in 15.73 V, which is more than 1.5 V less. As for the (Al,In)N/GaN heterostructure investigated in this chapter, the phase change profile derived with the best-fit value in $\Delta V_{\text{MIP}}=0.84$ V is shown with red line.

It is important to note that, by using only V_{MIP} as the fitting parameter, the features (e.g., peaks in phase) occurring near the heterostructure interfaces cannot be reproduced.

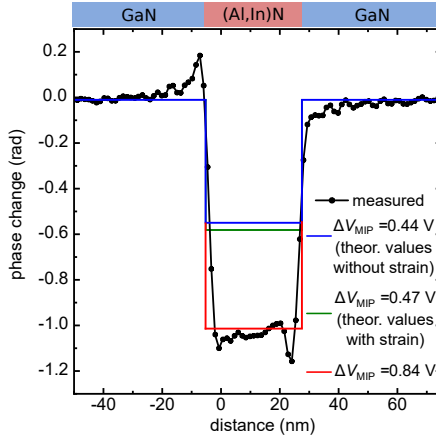


Figure 8.9: Comparison between the experimental and calculated phase change profiles across the (Al,In)N/GaN heterostructure. Theoretical mean inner potential values are used, with the blue line neglecting the strain effect, and the green line considering the strain effect. The profile derived with the best-fit $\Delta V_{\text{MIP}}=0.84$ V (red line) is attached for comparison.

8.3.3 Effect of electron affinity and polarization

To reproduce the phase peaks near the interface of heterostructure, one needs to take the influence of the electron affinity χ and polarization difference into consideration. Figure 8.10 illustrates the comparison of the measured profile (black line and symbols) with simulated results (colored lines). The calculated phase profiles are smoothed using a moving average with a width of 4 nm to account for the broadening effect due to a high tilt angle during the experiment. All the calculations are carried out with the theoretical electron affinity values: 3.48 eV and 4.1 eV for the (Al,In)N and GaN layers, respectively (see Sec.8.3.1).

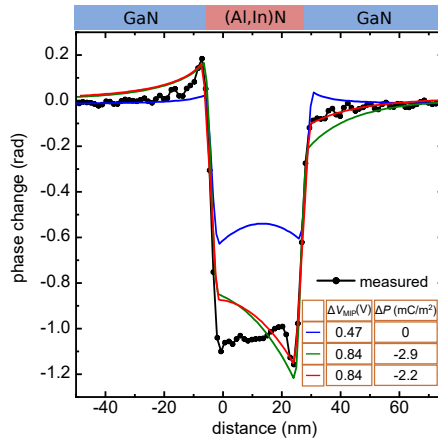


Figure 8.10: Comparison between the experimental and calculated phase change profiles across the (Al,In)N/GaN heterostructure. All the calculations are carried out with the theoretical electron affinity values. The blue line is derived using theoretical V_{MIP} difference and neglecting polarization. The red and green lines are calculated with a V_{MIP} difference 0.84 V, and using difference polarization difference values.

(i) The blue line is derived using the theoretical V_{MIP} difference between the GaN and (Al,In)N layers, accounting for the strain effect (i.e., 0.47 V) but not considering the polarization difference. Notably, the calculated phase change within the (Al,In)N layer is merely half of the measured value and cannot be resolved by adding the electron affinity. Indeed, after considering the electron affinity, minor peaks appear near the interfaces, specifically positive peaks in the GaN layer and negative peaks in the (Al,In)N layer. However, these peaks are relatively symmetric and do not agree with the measured phase profile.

(ii) The red and green lines are calculated with the best-fit V_{MIP} difference of 0.84 V between the GaN and (Al,In)N layers, and with different polarization changes at the interface as a fitting parameter. With a $\Delta P = -2.2 \text{ mC/m}^2$ (red line), the measured phase peaks occurring near interfaces are reproduced best, notably the positive peak in the GaN side of the lower interface and the negative peak in the (Al,In)N side of the upper interface.

Next, I compare the measured ΔP with the theoretical value. For the investigated (Al,In)N and GaN heterostructure, the theoretical polarization difference can be derived on the basis of Eq. (3.43) in Chap. 3, using measured strain values. The polarization constants of the ternary (Al,In)N layers are obtained by interpolating

using Vegard's law[140] and assuming a nominal composition of the $\text{Al}_{0.81}\text{In}_{0.19}\text{N}$ layer. The parameters and derived total polarization are listed in the Tab. 8.3.

	$\overline{P}_{eff}^{(H,ref)}$ (C/m ²)	e_{31} (C/m ²)	e_{33} (C/m ²)	\overline{P}_{tot} (C/m ²)
GaN	1.312	-0.551	1.020	1.310±0.012
(Al,In)N	1.290	-0.662	1.506	1.308±0.026

Table 8.3: Polarization constants[140] along with theoretical total polarization for GaN and (Al,In)N layers. The constants used for the ternary (Al,In)N layer are interpolated from values of its binary constituents by Vegard's law. The strain applied derives from the HAADF measurement.

These yield a theoretical polarization change at the interface between (Al,In)N and GaN layers, calculated with the measured strain, of $\sim -2 \pm 29 \text{ mC/m}^2$. Note the error bar is rather large due to the uncertainty of the lattice constant measurements. The value is nevertheless in excellent agreement with the measured value of $-2.2 \pm 0.7 \text{ mC/m}^2$.

8.3.4 Influence of the In composition gradient in (Al,In)N on phase map

The measured phase profile across the GaN/(Al,In)N/GaN heterostructure cannot be fully reproduced through simulation when considering a homogeneous composition for the (Al,In)N layer. In specific, with $\Delta P = -2.2 \text{ mC/m}^2$, the peaks at interfaces appear. However, the polarization difference results within the (Al,In)N layer in a steep almost linear phase slope in the (Al,In)N layer, but the experimentally found flat phase profile within (Al,In)N cannot be obtained. Therefore, an (Al,In)N layer with a homogeneous composition cannot account for the measured phase profile. In this section, it will be demonstrated how this *apparent* discrepancy can be resolved by taking the In composition gradient into account, which has been detected in the EDX measurement (see Fig. 8.6).

In the self-consistent electrostatic potential calculation, the composition gradient is modelled by replacing the single (Al,In)N layer with six sublayers, each exhibiting a progressively increased indium concentration ranging from 16% to 19%. A sketch of modelled heterostructure with composition gradient in the (Al,In)N layer is depicted in Fig. 8.11(a): From the left-most sublayer (number 1) to the right-most sublayer (number 6), the indium composition increases from 16% to 19% with an increment of 0.6% in each sublayer. These compositional changes, in turn, are effectively reflected by gradients of V_{MIP} and electron affinity χ . In specific, from the

sublayer (Al,In)N 1 to (Al,In)N 6, V_{MIP} increases from 15.9 to 16.05 V in steps of 0.03 V. Since the (Al,In)N layer is revealed to be uniformly strained (as indicated by the GPA results), the total polarization at each sublayer is assumed to be identical to the value found in calculations assuming a homogeneous composition. The electron affinity values are taken from theoretical calculations and changes accordingly to the indium concentration, assuming a 1:6 valence-to-conduction bandgap change distribution ratio.

Figure 8.11(b) illustrates the resulting phase change profile (red solid line), which agrees well with the experimental data (black symbols and line). For comparison, the phase profile calculated assuming a homogeneous (Al,In)N layer is attached (red dashed line). Notably, the steep phase slope in the profile derived using a homogeneous composition (Al,In)N layer (red dashed line) disappears and a flat phase change within the (Al,In)N layer is found. This is due to the fact that 3% decrease in In content leads to a increase in the mean inner potential of 0.15 V, which in turn corresponds to a substantial increment of phase change of 0.18 rad at the given lamella crystalline thickness.

The mean inner potential and polarization difference applied to yield the best-fit phase change profile are summarized in Tab. 8.4. For comparison, parameters calculated on the basis of literature values and measured strain are listed in brackets.

Layer	In (%)	V_{MIP} (V)	$P(\text{C}/\text{m}^2)$
GaN	/	16.89 (16.89±0.12)	1.310 (1.310±0.012)
(Al,In)N sublayer 1	16.0%	15.9 (16.27±0.23)	1.308 (1.308±0.026)
(Al,In)N sublayer 2	16.6%	15.93 (16.3±0.23)	1.308 (1.308±0.026)
(Al,In)N sublayer 3	17.2%	15.96 (16.33±0.23)	1.308 (1.308±0.026)
(Al,In)N sublayer 4	17.8%	15.99 (16.36±0.23)	1.308 (1.308±0.026)
(Al,In)N sublayer 5	18.4%	16.02 (16.39±0.23)	1.308 (1.308±0.026)
(Al,In)N sublayer 6	19.0%	16.05 (16.42±0.23)	1.308 (1.308±0.026)

Table 8.4: Parameters used for the self-consistent calculation with the best agreement to the experimental data. The theoretical values in the brackets are derived with measured strain. The detailed derivation of these parameters can be found in Chap. 3.

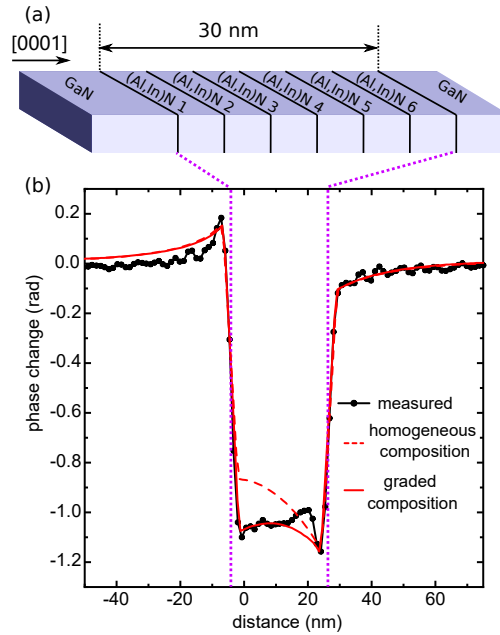


Figure 8.11: (a) Modelled lamella structure for electrostatic potential calculation. Six sublayers of (Al,In)N with gradual increasing indium composition from 16% (sublayer 1) to 19% (sublayer 6) are configured to account for the composition gradient effect. (b) Comparison between measured phase profile (black symbol and line) and profiles calculated assuming a composition gradient in (Al,In)N (red solid line). For comparison, the profile derived using a homogeneous composition is also included (red dashed line).

In summary, if a composition gradient is considered in the self-consistent electrostatic potential calculation, the measured phase profile across the GaN/(Al,In)N/GaN heterostructure can be well reproduced. The gradient in V_{MP} resulting from the composition gradient is the dominating contributing to the flat phase profile within the (Al,In)N layer. In addition, a polarization difference of $-2.2 \pm 0.7 \text{ mC/m}^2$ between (Al,In)N and GaN layer is revealed, which is in line with theory.

8.4 Discussion: Origin of the composition gradient

Composition pulling effect

At this stage, the origin of the observed composition gradient within the (Al,In)N layer needs to be elucidated. A similar phenomenon, commonly referred to as the "composition pulling effect", is frequently observed in the field of ternary III-nitride epitaxial layer growth.[224, 225, 226, 227, 168, 228, 229] It is especially prevalent when utilizing MOVPE or MOCVD growth techniques and is considered to arise due to the strain developed or relaxation within the ternary layer.

(i) Hiramatsu *et al.* studied the composition pulling effect during the initial stages of MOVPE growth of (In,Ga)N on GaN.[224] The results indicate that the lattice mismatch between the (In,Ga)N and the underlying GaN layer is at the origin of a composition gradient. During the initial growth stage, the larger indium atoms are incorporated less than intended into the compressively-strained (In,Ga)N layer to reduce the deformation energy. With increasing in thickness of the (In,Ga)N layer, this reduced In incorporation becomes less pronounced, primarily due to the reduction of lattice strain, mediated by the creation of crystalline defects.

(ii) In analogy, this consideration also applies to compressively-strained (Al,Ga)N layers grown on AlN.[225, 226, 227] In the (Al,Ga)N/AlN distributed Bragg reflector heterostructure, an Al composition gradient within the (Al,Ga)N layer was observed.[225] This gradient arises from the reduced incorporation of Ga atoms due to the compressive strain during the initial stage of the growth. He *et al.* reported a similar composition gradient in the (Al,Ga)N layer grown on AlN.[227] The authors suggest that the formation of the observed composition gradient is due to the partial relief of compressive stress arising from the generation of misfit dislocations.

(iii) For the (Al,In)N grown on GaN, similar composition gradient occurs too, but depending on the composition, the (Al,In)N layer can be both tensile and compressive strained.

Jiao *et al.* investigated the tensively strained $\text{Al}_{0.87}\text{In}_{0.13}\text{N}$ grown on GaN and revealed a clear relationship between strain and compositional grading of indium:[230] The incorporation energy of indium decreases, increasing indium incorporation with tensile strain.

Following the same line of argument, in the case of compressively strained (Al,In)N (i.e., with an In content greater than 17%–19%), it can be rather anticipated that the compressive strain prevents the incorporation of indium into the ternary (Al,In)N layer.[228, 229]

In the here studied (Al,In)N layer, no in-plane lattice strain is detected. Only in growth direction, a tensile lattice strain of $0.61 \pm 0.38\%$ was found (see Fig. 8.3). Hence, if the out-of-plane tensile strain affects the composition, the In incorporation should be increased during the initial growth stages. This is in contradiction to the experimental observation (see Fig. 8.6). Therefore, the composition pulling effect can be ruled out to be the dominant origin of the observed In composition gradient here.

Growth interruption model

Another possible explanation for the composition gradient in the ternary (Al,In)N layer can be linked to the fact that the (0001) growth surface of group III-nitrides is typically covered with a group III adlayer, such as Ga (1×1) on GaN (0001) surfaces.[231, 232] An analogous adlayer is anticipated to occur for ternary III-nitride. However, its' composition does not necessarily need to follow that of the intended ternary composition. It rather depends on the vapor pressures and incorporation efficiencies of constituent elements. During the transition from GaN to (Al,In)N growth, the adlayer needs to be exchanged from Ga to Al/In. This exchange process is not trivial, since it would lead to a gradual change of composition over extended layer thickness.

In order to circumvent this effect, a growth interruption is used at the interface between (Al,In)N and GaN.[233] Thereby, the group III adlayer is consumed up by nitrogen atom. The resulting surface exhibits a 1×1 stoichiometric top layer. During this growth interruption, the growth temperature can also be adjusted to that needed for the growth of new material. Hence, the growth of (Al,In)N on GaN starts with a GaN (0001) surface free of adlayers, known as dry surface.[234] For the (Al,In)N growth, the adlayer has to be reformed, starting with the Al/In composition ratio defined by their corresponding fluxes. Since the N flux is always present, the Al and In atoms deposited will be incorporated rather directly. Nonetheless, nitrogen atom bonds preferentially with Al since the binding energy between Al and N is higher than that between In and N. [235, 236] Therefore, the adlayer will be built up preferentially from In atoms which are not directly incorporated upon progressing growth. Eventually, this effect gives rise to a steady-state adlayer predominately occupied by In atoms.

The question is how much In is ultimately incorporated into the adlayer for reaching a steady-state growth, and thus how many monolayers (ML) of (Al,In)N need to be grown until the steady state is reached. Experimentally, one can estimate the amount of In missing in the (Al,In)N adlayer as compared to the intended composition to be $0.73_{-0.16}^{+0.26}$ ML. This value suggests that the group III adlayer exhibits an Al:In ratio of roughly 1:3 if a single adlayer is present during the steady-state growth. Hence, the need to rebuild a group III adlayer for steady state growth after growth interruption is at the origin of the observed composition gradient.

During growth of the In-deficient (Al,In)N layer, strain develops unavoidably. This is the reason why the growth does not start with pure AlN on GaN but rather with an (Al,In)N layer which exhibits a composition with around 15%-16% In resulting to a much lower lattice mismatch.

8.5 Summary

In this chapter, the findings from previous chapters are applied to interpret the phase change profile measured across the (Al,In)N/GaN heterostructure. A composition gradient along the growth direction is revealed within the (Al,In)N layer using EDX. This effect cannot be attributed to the composition pulling effect, as suggested thus far for similar composition gradients in ternary group III-nitrides. It is shown that the composition gradient is rather due to the rebuild of a group III adlayer after growth interruption, this adlayer is estimated to exhibit an Al:In ratio of 1:3.

On the basis of observed composition gradient in the (Al,In)N layer, a self-consistent electrostatic potential calculation is carried out, using polarization change as a fitting parameter. Through the quantitative comparison between the measurements and the calculated results, a polarization change of -2.2 ± 0.7 mC/m² at the (Al,In)N and GaN interface is unraveled, demonstrating an excellent agreement with the theoretical value. The difference in measured mean inner potential between the GaN and (Al,In)N layers is found, however, larger than the theoretical predictions. This discrepancy is suggested to be related to the uncertainty in the actual modeling of the electron density applied in the calculation, hence pointing to the need to reassess the modelling of mean inner potential of group III-nitrides binary as well as their alloys.

Chapter 9

Conclusion

TEM lamellas prepared by FIB exhibit surface shell layers with different degrees of damage covering the pristine crystalline core, i.e., a defect-rich crystalline inner shell and an amorphous outer shell. The high concentration of point defects notably in the inner shell gives rise to surface Fermi-level pinning, which hampers the quantitative interpretation of the phase map extracted from electron holography measurements. Most of the previous studies handled FIB-induced damage as an electrically inactive layer, neglecting fully the resulting surface potential. This simplified model can indeed provide a qualitative interpretation of data measured on, for example, p - n junction. However, such a model falls short in explaining the phase map measured across doping modulation semiconductor structures, e.g., n^+ - n doping step. Hence, a precise atomic scale description of the surface damages is needed.

In this thesis, off-axis electron holography is utilized to characterize and identify the types of FIB-induced point defects as well as their dynamics and point defect reactions during annealing, using group III-nitride semiconductors as model system. This leads to a comprehensive understanding of different types of FIB-induced shells and dead layers and their influence on the electrostatic potentials. The physical insight gained is used to demonstrate a truly quantitative potential mapping of group III-nitride hetero-interface.

First, by employing the surface Fermi-level pinning model, Chap. 5 unravels the physical origin behind the longstanding question concerning the discrepancy between theoretical predictions and electron holographic results in electrostatic potential mapping: The phase contrast at n - n^+ GaN doping steps is shown to exhibit a giant enhancement as compared to expectations, with an almost negligible thickness dependence. The origin of the giant enhancement of the phase contrast is found to arise from the doping dependent screening length of the FIB-induced surface Fermi-level pinning occurring in the defect-rich crystalline inner shell (below

the outer amorphous shell). Since the lamellas were prepared with a same set of FIB parameters, this near surface screening region remains unchanged for lamellas with different thicknesses, resulting in an essentially constant electron optical phase contrast with respect to lamella thickness. The contribution of the built-in potential is rather negligible, since it is too small for the given modulation doping and only relevant for large built-in potentials at e.g., p - n junctions. Thus, the weak built-in potential of GaN doping steps adds only a small thickness dependence to the phase contrast. This chapter dissects the previously termed "dead layers" to identify the defect-rich crystalline inner shell and the screening of its Fermi-level pinning being solely relevant for electron optical phase differences, thereby providing a quantitative approach to dead layers at surfaces of FIB-prepared TEM lamellas.

Another important observation is that, the same set of FIB parameters leads to lamellas with comparable surface Fermi-level pinning values. This conclusion is drawn on the basis of a rigorous and quantitative analysis of a substantial experimental data set (see Chap. 5, 6, and 7): The phase change contrast measured across n - n^+ GaN doping steps and δ -doped GaN layers in over 20 TEM lamellas, in conjunction with simulated results, has unraveled that the freshly FIB-prepared GaN lamellas manifest a Fermi-level pinning 0.61 ± 0.2 eV above the valence band edge. The rather small margin of error implies a comparable surface conditions among all the investigated lamellas.

This Fermi-level pinning of n -type GaN can only be achieved by a defect which exhibits a (0/-) charge transfer level close to the valence band edge. A thorough examination reveals that solely carbon substitutional on the nitrogen sites C_N carry the appropriate charge state at the observed pinning level. In addition, the implantation of carbon impurity in GaN is supported by SRIM/TRIM calculations: Utilizing the FIB parameters used in the last polishing step, it is demonstrated that carbon is implanted in high concentration, decaying exponentially into the lamella. At a depth larger than ~ 13 nm, the concentration of C_N falls below that of dopants (i.e., Si), hence the screening of the defect-induced surface potential is expected to take place.

In order to circumvent the influence of the C_N , in-situ annealing experiments are carried out in Chap. 6. It is found that the FIB-induced pinning level gradually increases from 0.57 to about 2 eV above E_V upon annealing between 250° C and 500° C and remains high after cooling down to room temperature. This indicates an irreversible thermal healing, reducing the concentration of implanted C_N and hence lifting the C_N -induced Fermi-level pinning. The dominating higher midgap pinning level is attributed to the states associated with the amorphous-crystalline

interface. The findings indicate that temperatures as low as approximately 250°C are effective in initiating defect healing. This discovery is particularly significant for the electron holography community, offering insights into methods for lifting the electrical impact of FIB-induced defects for III-nitride system.

Furthermore, time-resolved in-situ annealing experiments are performed to resolve and quantify the dynamics of FIB-implanted C_N in GaN upon annealing (see Chap. 7). On the basis of measured small migration length (i.e., in the order of one lattice constant), it has been identified that switching of C from substitutional to interstitial sites is the atomic process responsible for lifting the Fermi-level pinning in the lower part of the bandgap. This process has an activation barrier energy of 2.27 ± 0.26 eV.

Based on these findings, the quantification of the phase change profile across the (Al,In)N/GaN interface is conducted in Chap. 8. In order to simulate the phase change profile for such heterostructure with the self-consistent electrostatic potential calculation, a comprehensive set of parameters, including dopant concentration, bandgap energy, electron affinity, mean inner potential, lamella crystalline thickness, chemical composition, as well as the surface Fermi-level pinning, is required. A composition gradient along the growth direction is detected within the (Al,In)N layer. Contrary to the suggested composition pulling effect for similar gradients in ternary group III-nitrides, it is demonstrated that the observed composition gradient results from the rebuilding of a group III adlayer after growth interruption. The experimentally derived Al:In ratio in the adlayer is 1:3. On the basis of the measured parameters as well as the composition gradient in the (Al,In)N layer, a self-consistent electrostatic potential calculation is performed, utilizing polarization change as a fitting parameter. In the quantitative comparison between the measurements and the calculated results, a polarization change of -2.2 ± 0.7 mC/m² at the Al_{0.81}In_{0.19}N and GaN interface is revealed. This value shows excellent agreement with the theoretical prediction. In contrast, the measured difference in mean inner potential between the GaN and Al_{0.81}In_{0.19}N layers is found to be larger than the theoretical value, which is proposed to be linked to uncertainties in the calculated electron density and band structure arising from different approximations used in DFT calculations, hence affecting the precision of the calculated mean inner potential.

The studies presented in this thesis emphasize the critical and indispensable need for the quantitative characterization of FIB-induced damages, which is a prerequisite for truly quantitative analysis of phase change maps measured in electron holographic experiments. The identified dominant electrically active point defect, namely C_N , underscores the primary requirement for a complete ultra-high vacuum

process from lamella preparation to electron holographic measurement. Furthermore, this thesis illustrates a novel application of electron holography, identification and quantification of point defect reactions upon annealing, providing an unprecedented access to the physical processes governing device stability.

Abstract

Off-axis electron holography can provide quantitative mapping of the electrostatic potential on TEM lamellas at high spatial and energy resolution. However, the presence of surface potentials induced by point defects, implanted during focused ion beam (FIB) preparation processes, significantly influence the phase change of the transmitted electron wave, hampering the quantitative extraction of the electrostatic potential. This thesis centers on identifying the type of FIB-implanted point defects and quantifying their thermal dynamics, using group III-nitride lamellas as model system. For this purpose, the measured phase change profile is quantitatively compared to the results of self-consistent electrostatic potential calculations, that incorporate the treatment of FIB-induced point defects through the modeling of surface states resulting in a Fermi-level pinning.

The measured phase contrast across n - n^+ GaN doping structures shows a giant enhancement compared to theoretical predictions, when considering the change of the built-in potential, only. This apparent discrepancy is resolved in this thesis by demonstrating the presence of a defect-rich inner shell, covered by an amorphous outer shell: The predominant contribution to the phase contrast arises from a FIB-induced surface Fermi-level pinning, which occurs in the defect-rich crystalline inner shell of the TEM lamella, and its doping dependent screening length towards the pristine crystalline core. The contribution of the built-in potential is negligible for modulation doping and only relevant for large built-in potentials at, e.g., p - n junctions.

The FIB-induced point defects are further investigated using in-situ annealing experiments, which unravel a decrease in phase contrast across GaN n - n^+ - n doping structures, starting at temperatures as low as 250 °C. These observations are found to originate from an irreversible shift of the defect-induced Fermi-level pinning near the valence band towards a midgap pinning, present at the crystalline-amorphous interface of TEM lamella. This shift is attributed to the healing of point defects in the lamella's inner shell. By quantifying the defect pinning and their charge transfer levels, the dominant defect type in the as FIB-prepared group III-nitride lamellas is identified as substitutional carbon on nitrogen sites (C_N). This defect type as well as the widths of the amorphous and crystalline shell layers of the lamella are

consistent with transport of ions in matter (TRIM) simulations, which are used to model the final polishing step of the FIB process.

In order to identify and quantify the point defect dynamics and their reactions involved in the thermal healing process, time-resolved in-situ annealing experiments are conducted: An exponential decay of the phase contrast across the n - n^+ GaN doping structures with annealing time is observed. The temperature dependence of the corresponding time constant of the decay exhibits an Arrhenius behavior, indicative of thermally activated defect diffusion. On basis of the measured diffusion lengths in the order of a lattice constant, a site switching process of carbon, from substitutional to interstitial positions, is found to be responsible for the decay in phase contrast and thus for lifting the Fermi-level pinning in the lower part of the band gap. The activation barrier energy of the carbon site switching process is measured to be 2.27 ± 0.26 eV.

On basis of these findings, the polarization changes at the (Al,In)N/GaN hetero-interface are investigated. A composition gradient along the growth direction is observed within the (Al,In)N layer and attributed to the rebuilding of a group III adlayer after growth interruption. The quantitative comparison between the measured phase profile and the one derived from self-consistent simulations, taking into account a surface Fermi-level pinning by carbon defects and an indium composition gradient, reveals a polarization change of -2.2 ± 0.7 mC/m² at the Al_{0.81}In_{0.19}N and GaN interface, in excellent agreement with theory.

These findings underscore the critical and essential requirement for the quantitative characterization of FIB-induced damages. This is a prerequisite for a truly quantitative interpretation of phase change maps obtained in electron holographic experiments. Furthermore, the investigations illustrate a novel application of electron holography for identification and quantification of point defect reactions upon annealing, providing an unprecedented access to the physical processes governing device stability.

Elektronenholografie ermöglicht eine quantitative Kartierung des elektrostatischen Potentials in TEM-Lamellen mit hoher räumlicher und energetischer Auflösung. Die Anwesenheit von Oberflächenpotentialen, die durch Punktdefekte induziert werden, welche während der Vorbereitungsprozesse mit fokussiertem Ionenstrahl (FIB) implantiert werden, beeinflusst signifikant die Phasenänderung der Elektronenwelle und behindert die quantitative Extraktion des elektrostatischen Potentials. Diese Dissertation konzentriert sich darauf, den Typ der durch FIB implantierten Punktdefekte zu identifizieren und ihre dynamischen Eigenschaften zu quantifizieren, wobei Gruppe III-Nitrid-Lamellen als Modellsystem dienen. Zu diesem Zweck wird das gemessene Phasenprofil quantitativ mit den Ergebnissen

selbstkonsistenter elektrostatischer Potentialsimulationen verglichen, die FIB induzierten Punktdefekten durch Oberflächenzustände beschreiben, die zu einem Fermi-Level-Pinning führen.

Der gemessene Phasenkontrast über $n-n^+$ GaN-Dotierungsstrukturen zeigt eine riesige Kontrastverstärkung im Vergleich zu theoretischen Vorhersagen, wenn nur die Diffusionsspannung (built-in Potenzial) berücksichtigt wird. Dieser scheinbare Widerspruch wurde in dieser Dissertation aufgelöst, indem die Anwesenheit einer defektreichen inneren Schale, bedeckt von einer amorphen äußeren Schale, nachgewiesen wurde: Der dominierende Beitrag zum Phasenkontrast wird durch ein FIB-induziertes Fermi-Level-Pinning an der Oberfläche erzeugt, dass in der defektreichen kristallinen inneren Schale der TEM-Lamelle auftritt, in Kombination mit einer dotierungsabhängigen Abschirmlänge. Der Beitrag der Diffusionsspannung ist für Modulationsdotierung vernachlässigbar und nur relevant an z.B. $p-n$ -Übergängen mit großen Diffusionsspannungen.

Die FIB-induzierten Punktdefekte werden ferner mittels in-situ Heizexperimenten untersucht, die ab 250°C eine Abnahme des Phasenkontrasts entlang der GaN $n-n^+-n$ Dotierungsstrukturen zeigten. Diese Beobachtungen weisen auf eine irreversible Verschiebung des durch Defekte verursachten Fermi-Level-Pinnings nahe des Valenzbands in Richtung der Bandlückenmitte an der kristallin-amorphen Grenzfläche der TEM-Lamelle hin. Diese Verschiebung wird auf die Heilung von Punktdefekten in der inneren Schale der Lamelle zurückgeführt. Durch Quantifizierung des Defektpinning- und Umladungsenergieniveaus wird der dominante Defekttyp in den FIB präparierten Gruppe III-Nitrid Lamellen als substitutionelles Kohlenstoffatom auf Stickstoffplätzen (C_N) identifiziert. Dieser Defekttyp sowie die Dicken der amorphen und kristallinen Schalen der Lamelle sind konsistent mit Transport of Ions in Matter (TRIM)-Simulationen, die zur Modellierung des abschließenden Polierschritts in der FIB Präparation verwendet werden.

Um die Punktdefektdynamik und ihre Reaktionen im thermischen Heilungsprozess zu identifizieren und quantifizieren, werden zeitaufgelöste in-situ Heizexperimente durchgeführt: Ein exponentieller Abfall des Phasenkontrasts der $n-n^+$ GaN Dotierungsstrukturen mit der Temperaturzeit wird beobachtet. Die temperaturabhängige Zeitkonstante des Abfalls zeigt ein Arrhenius-Verhalten, dass auf thermisch aktivierte Diffusion von Defekten hinweist. Aufgrund der gemessenen Diffusionslängen in der Größenordnung eines Gitterabstands wird gefolgert, dass ein Positionswechsel von Kohlenstoff, von substitutionellen zu interstitiellen Gitterplätzen für den Abfall des Phasenkontrasts und damit für das Aufheben des Fermi-Level-Pinnings im unteren Teil der Bandlücke verantwortlich ist. Die Aktivierungsenergie des Kohlenstoff Positionswechsel wurde auf $2.27 \pm 0.26 \text{ eV}$ gemessen.

Auf Grundlage dieser Erkenntnisse werden Polarisationsänderungen an (Al,In)N/GaN-Heterogrenzflächen untersucht. Experimentell wurde ein Gradient in der Zusammensetzung innerhalb der (Al,In)N-Schicht in Wachstumsrichtung beobachtet, der auf die Wiederherstellung der Gruppe-III Adatomschicht nach einem Wachstumsstopp zurückgeführt wird. Der quantitative Vergleich des gemessenen Phasenprofils mit selbstkonsistenten Simulationen, die ein Oberflächen-Fermi-Level-Pinning durch Kohlenstoffdefekte sowie einen Indium-Zusammensetzungsgradienten berücksichtigen, ergibt eine Polarisationsänderung von $-2.2 \pm 0.7 \text{ mC/m}^2$ an der $\text{Al}_{0.81}\text{In}_{0.19}\text{N}/\text{GaN}$ -Grenzfläche, in exzellenter Übereinstimmung mit der Theorie.

Diese Ergebnisse unterstreichen die entscheidende und wesentliche Notwendigkeit für die quantitative Charakterisierung von FIB-induzierten Schäden. Dies ist eine Voraussetzung für eine wirklich quantitative Interpretation von Phasenänderungen, die in elektronenholographischen Experimenten gewonnen werden. Darüber hinaus veranschaulicht die Untersuchung eine neuartige Anwendung der Elektronenholographie zur Identifizierung und Quantifizierung von Punktdefektreaktionen beim Tempern und bietet einen hervorragenden Zugang zu den physikalischen Prozessen, die die Stabilität von Bauelementen bestimmen.

Acronym list

CBED	Convergent beam electron diffraction
DFT	Density functional theory
EDX	Energy dispersive X-rays
FIB	Focused ion beam
GPA	Geometric phase analysis
HAADF	High angle annular dark field imaging
MOCVD	Metal-organic chemical vapor deposition
MOVPE	Metal-organic vapour-phase epitaxy
PPA	Peak pairing analysis
SIMS	Secondary ion mass spectrometry
SRIM	Stopping and range of ions in matter
STEM	Scanning transmission electron microscopy
TEM	Transmission electron microscopy
TRIM	Transport of ions in matter

List of own publications

- [P1] K. Ji, M. Schnedler, Q. Lan, F. Zheng, Y. Wang, Y. Lu, H. Eisele, J.-F. Carlin, R. Butté, N. Grandjean, R. E. Dunin-Borkowski, and Ph. Ebert, “Identification and thermal healing of focused ion beam-induced defects in GaN using off-axis electron holography”, *Appl. Phys. Express*, vol. 17, pp. 016505, 2024
- [P2] K. Ji, M. Schnedler, Q. Lan, J.-F. Carlin, R. Butté, N. Grandjean, R. E. Dunin-Borkowski, and Ph. Ebert, “Quantifying carbon site switching dynamics in GaN by electron holography”, submitted to *Phys. Rev. Lett.*, 2024
- [P3] K. Ji, M. Schnedler, Q. Lan, J.-F. Carlin, R. Butté, N. Grandjean, R. E. Dunin-Borkowski, and Ph. Ebert, “Origin of giant enhancement of phase contrast in electron holography of modulation-doped *n*-type GaN”, *Ultramicroscopy*, vol. 264, pp. 114006, 2024

List of own publications

Bibliography

- [1] T. Matsuoka, H. Okamoto, M. Nakao, H. Harima, and E. Kurimoto, "Optical bandgap energy of wurtzite InN," *Appl. Phys. Lett.*, vol. 81, pp. 1246–1248, 2002.
- [2] S. N. Mohammad, A. A. Salvador, and H. Morkoc, "Emerging gallium nitride based devices," *Proc. IEEE*, vol. 83, pp. 1306–1355, 1995.
- [3] J. Li, K.-B. Nam, M. L. Nakarmi, J.-Y. Lin, H. Jiang, P. Carrier, and S.-H. Wei, "Band structure and fundamental optical transitions in wurtzite AlN," *Appl. Phys. Lett.*, vol. 83, pp. 5163–5165, 2003.
- [4] S. Nakamura, "III–V nitride based light-emitting devices," *Solid State Commun.*, vol. 102, pp. 237–248, 1997.
- [5] E. A. Jones, F. F. Wang, and D. Costinett, "Review of Commercial GaN Power Devices and GaN-Based Converter Design Challenges," *IEEE J. Emerg. Sel. Top. Power Electron.*, vol. 4, pp. 707–719, 2016.
- [6] H. Amano, Y. Baines, E. Beam, M. Borga, T. Bouchet, P. R. Chalker, M. Charles, K. J. Chen, N. Chowdhury, R. Chu, *et al.*, "The 2018 GaN power electronics roadmap," *J. Phys. D: Appl. Phys.*, vol. 51, p. 163001, 2018.
- [7] T. J. Flack, B. N. Pushpakaran, and S. B. Bayne, "GaN technology for power electronic applications: a review," *J. Electron. Mater.*, vol. 45, pp. 2673–2682, 2016.
- [8] K. Shirabe, M. M. Swamy, J.-K. Kang, M. Hisatsune, Y. Wu, D. Kebort, and J. Honea, "Efficiency comparison between si-igbt-based drive and gan-based drive," *IEEE Trans. Ind. Appl.*, vol. 50, pp. 566–572, 2014.
- [9] A. Lidow, M. De Rooij, J. Strydom, D. Reusch, and J. Glaser, *GaN transistors for efficient power conversion*. John Wiley & Sons, 2019.
- [10] A. A. Fletcher and D. Nirmal, "A survey of Gallium Nitride HEMT for RF and high power applications," *Superlattices Microstruct.*, vol. 109, pp. 519–537, 2017.

- [11] K. Peng, S. Eskandari, and E. Santi, “Characterization and modeling of a gallium nitride power hemt,” *IEEE Trans. Ind. Appl.*, vol. 52, pp. 4965–4975, 2016.
- [12] M. B. Johnson, O. Albrektsen, R. M. Feenstra, and H. W. M. Salemink, “Direct imaging of dopants in GaAs with cross-sectional scanning tunneling microscopy,” *Appl. Phys. Lett.*, vol. 63, pp. 2923–2925, 1993.
- [13] Ph. Ebert, T. Zhang, F. Kluge, M. Simon, Z. Zhang, and K. Urban, “Importance of Many-Body Effects in the Clustering of Charged Zn Dopant Atoms in GaAs,” *Phys. Rev. Lett.*, vol. 83, pp. 757–760, 1999.
- [14] S. Landrock, Y. Jiang, K. H. Wu, E. G. Wang, K. Urban, and Ph. Ebert, “Origin of nanoscale potential fluctuations in two-dimensional semiconductors,” *Appl. Phys. Lett.*, vol. 95, p. 072107, 2009.
- [15] K. Morgenstern, E. Lægsgaard, and F. Besenbacher, “STM study of step dynamics around a bulk dislocation intersection with a Ag(111) surface,” *Phys. Rev. B*, vol. 71, p. 155426, 2005.
- [16] R. Shikler, T. Meoded, N. Fried, B. Mishori, and Y. Rosenwaks, “Two-dimensional surface band structure of operating light emitting devices,” *J. Appl. Phys.*, vol. 86, pp. 107–113, 1999.
- [17] L. Jung, J. Pries, T. W. Maß, M. Lewin, D. S. Boyuk, A. T. Mohabir, M. A. Filler, M. Wuttig, and T. Taubner, “Quantification of carrier density gradients along axially doped silicon nanowires using infrared nanoscopy,” *ACS Photonics*, vol. 6, pp. 1744–1754, 2019.
- [18] F. Giannazzo, V. Raineri, A. La Magna, S. Mirabella, G. Impellizzeri, A. Piro, F. Priolo, E. Napolitani, and S. Liotta, “Carrier distribution in quantum nanostructures by scanning capacitance microscopy,” *J. Appl. Phys.*, vol. 97, p. 014302, 2005.
- [19] J. Sumner, R. Oliver, M. Kappers, and C. Humphreys, “Assessment of the performance of scanning capacitance microscopy for n-type gallium nitride,” *J. Vac. Sci. Technol. B*, vol. 26, pp. 611–617, 2008.
- [20] D. Sviridov, V. Jmerik, S. Rouvimov, D. Nechaev, V. Kozlovsky, and S. Ivanov, “Direct observation of spatial distribution of carrier localization sites in ultrathin GaN/AlN quantum wells by spreading resistance microscopy,” *Appl. Phys. Lett.*, vol. 114, p. 061601, 2019.

-
- [21] A. Schulze, T. Hantschel, P. Eyben, A. Verhulst, R. Rooyackers, A. Vandoooren, and W. Vandervorst, “Quantitative three-dimensional carrier mapping in nanowire-based transistors using scanning spreading resistance microscopy,” *Ultramicroscopy*, vol. 125, pp. 18–23, 2013.
- [22] E. T. Ritchie, D. J. Hill, T. M. Mastin, P. C. Deguzman, J. F. Cahoon, and J. M. Atkin, “Mapping free-carriers in multijunction silicon nanowires using infrared near-field optical microscopy,” *Nano Lett.*, vol. 17, pp. 6591–6597, 2017.
- [23] J. Stiegler, A. Huber, S. Diedenhofen, J. Gomez Rivas, R. Algra, E. Bakkers, and R. Hillenbrand, “Nanoscale free-carrier profiling of individual semiconductor nanowires by infrared near-field nanoscopy,” *Nano Lett.*, vol. 10, pp. 1387–1392, 2010.
- [24] M. B. Johnson, H. P. Meier, and H. W. M. Salemink, “Dopant and carrier profiling in modulation-doped GaAs multilayers with cross-sectional scanning tunneling microscopy,” *Appl. Phys. Lett.*, vol. 63, pp. 3636–3638, 1993.
- [25] S. Landrock, K. Urban, and P. Ebert, “Spontaneous 2D Accumulation of Charged Be Dopants in GaAs p – n Superlattices,” *Phys. Rev. Lett.*, vol. 96, p. 076101, 2006.
- [26] M. Morgenstern, J. Klijn, C. Meyer, M. Getzlaff, R. Adelung, R. A. Römer, K. Rossnagel, L. Kipp, M. Skibowski, and R. Wiesendanger, “Direct Comparison between Potential Landscape and Local Density of States in a Disordered Two-Dimensional Electron System,” *Phys. Rev. Lett.*, vol. 89, p. 136806, 2002.
- [27] J. K. Weiss, W. J. de Ruijter, M. Gajdardziska-Josifovska, M. R. McCartney, and D. J. Smith, “Applications of electron holography to the study of interfaces,” *Ultramicroscopy*, vol. 50, pp. 301–311, 1993.
- [28] H. Lichte and M. Lehmann, “Electron holography-basics and applications,” *Rep. Prog. Phys.*, vol. 71, p. 016102, 2007.
- [29] K. Yamamoto, K. Nakano, A. Tanaka, Y. Honda, Y. Ando, M. Ogura, M. Matsumoto, S. Anada, Y. Ishikawa, H. Amano, *et al.*, “Visualization of different carrier concentrations in n-type-GaN semiconductors by phase-shifting electron holography with multiple electron biprisms,” *Microscopy*, vol. 69, pp. 1–10, 2020.
- [30] Z. Gan, M. Gu, J. Tang, C. Wang, Y. He, K. Wang, C. Wang, D. Smith, and M. McCartney, “Direct mapping of charge distribution during lithiation of Ge

- nanowires using off-axis electron holography,” *Nano Lett.*, vol. 16, pp. 3748–3753, 2016.
- [31] H. Sasaki, K. Yamamoto, T. Hirayama, S. Ootomo, T. Matsuda, F. Iwase, R. Nakasaki, and H. Ishii, “Mapping of dopant concentration in a GaAs semiconductor by off-axis phase-shifting electron holography,” *Appl. Phys. Lett.*, vol. 89, 2006.
- [32] D. Cooper and R. E. Dunin-Borkowski, “Interpretation of phase images of delta-doped layers,” *Microscopy*, vol. 62, pp. S87–S98, 2013.
- [33] L. Amichi, *Etude du dopage de type p dans des nanostructures de GaN par corrélation entre sonde atomique tomographique et holographie électronique hors axe optique*. PhD thesis, Université Grenoble Alpes, 2018.
- [34] L. Amichi, I. Mouton, V. Boureau, E. D. Russo, P. Vennéguès, P. D. Mierry, A. Grenier, P.-H. Jouneau, C. Bougerol, and D. Cooper, “Correlative investigation of Mg doping in GaN layers grown at different temperatures by atom probe tomography and off-axis electron holography,” *Nanotechnology*, vol. 31, p. 045702, 2019.
- [35] Y. Wang, M. Schnedler, Q. Lan, F. Zheng, L. Freter, Y. Lu, U. Breuer, H. Eisele, J.-F. Carlin, R. Butté, N. Grandjean, R. E. Dunin-Borkowski, and P. Ebert, “Interplay of anomalous strain relaxation and minimization of polarization changes at nitride semiconductor heterointerfaces,” *Phys. Rev. B*, vol. 102, p. 245304, 2020.
- [36] C. B. Carter and D. B. Williams, *Transmission Electron Microscopy A Textbook for Materials Science*. Springer publication, 2009.
- [37] R. E. Dunin-Borkowski, A. Kovács, T. Kasama, M. R. McCartney, and D. J. Smith, *Springer Handbook of Microscopy*, ch. 16. Electron Holography, pp. 767–818. Springer Handbook, Springer, Cham, 2019.
- [38] E. Völkl, L. Allard, A. Datye, and B. Frost, “Advanced electron holography: a new algorithm for image processing and a standardized quality test for the FEG electron microscope,” *Ultramicroscopy*, vol. 58, pp. 97–103, 1995.
- [39] E. Voelkl and D. Tang, “Approaching routine $2\pi/1000$ phase resolution for off-axis type holography,” *Ultramicroscopy*, vol. 110, pp. 447–459, 2010.
- [40] R. E. Dunin-Borkowski, A. Kovács, T. Kasama, M. R. McCartney, and D. J. Smith, “Electron holography,” in *Springer Handbook of Microscopy*, pp. 767–818, Springer, 2019.

-
- [41] J. Ness, W. Stobbs, and T. Page, "A TEM Fresnel diffraction-based method for characterizing thin grain-boundary and interfacial films," *Philos. Mag. A*, vol. 54, pp. 679–702, 1986.
- [42] R. Schäublin, "Nanometric crystal defects in transmission electron microscopy," *Microsc. Res. Tech.*, vol. 69, pp. 305–316, 2006.
- [43] X. Yu, T. Asaka, Y. Tomioka, C. Tsuruta, T. Nagai, K. Kimoto, Y. Kaneko, Y. Tokura, and Y. Matsui, "TEM study of the influence of antisite defects on magnetic domain structures in double perovskite Ba₂FeMoO₆," *J. Electron Microsc. Tech.*, vol. 54, pp. 61–65, 2005.
- [44] S. Lloyd, N. Mathur, J. Loudon, and P. Midgley, "Magnetic domain-wall width in La_{0.7}Ca_{0.3}MnO₃ thin films measured using Fresnel imaging," *Phys. Rev. B*, vol. 64, p. 172407, 2001.
- [45] S. Lloyd, J. Loudon, and P. Midgley, "Measurement of magnetic domain wall width using energy-filtered fresnel images," *J. Microsc.*, vol. 207, pp. 118–128, 2002.
- [46] L. Houben, M. Luysberg, and T. Brammer, "Illumination effects in holographic imaging of the electrostatic potential of defects and *pn* junctions in transmission electron microscopy," *Phys. Rev. B*, vol. 70, p. 165313, 2004.
- [47] J. B. Park, T. Niermann, D. Berger, A. Knauer, I. Koslow, M. Weyers, M. Kneissl, and M. Lehmann, "Impact of electron irradiation on electron holographic potentiometry," *Appl. Phys. Lett.*, vol. 105, p. 094102, 2014.
- [48] D. B. Williams and C. B. Carter, *Transmission electron microscopy II Diffraction*. A Division of Plenum Publishing Corporation, 1996.
- [49] L. Allen and C. Rossouw, "Absorptive potentials due to ionization and thermal diffuse scattering by fast electrons in crystals," *Phys. Rev. B*, vol. 42, p. 11644, 1990.
- [50] S. Pennycook and D. Jesson, "High-resolution incoherent imaging of crystals," *Phys. Rev. Lett.*, vol. 64, p. 938, 1990.
- [51] S. Pennycook and D. Jesson, "High-resolution Z-contrast imaging of crystals," *Ultramicroscopy*, vol. 37, pp. 14–38, 1991.
- [52] C. Hall and P. B. Hirsch, "Effect of thermal diffuse scattering on propagation of high energy electrons through crystals," *Proc. R. Soc. A: Math. Phys. Eng.*, vol. 286, pp. 158–177, 1965.

- [53] D. Jesson and S. J. Pennycook, “Incoherent imaging of crystals using thermally scattered electrons,” *Proc. Math. Phys. Eng.*, vol. 449, pp. 273–293, 1995.
- [54] K. Sohlberg, T. J. Pennycook, W. Zhou, and S. J. Pennycook, “Insights into the physical chemistry of materials from advances in HAADF-STEM,” *Phys. Chem. Chem. Phys.*, vol. 17, pp. 3982–4006, 2015.
- [55] Y. Peng, P. D. Nellist, and S. J. Pennycook, “HAADF-STEM imaging with sub-angstrom probes: a full Bloch wave analysis,” *J. Electron Microsc.*, vol. 53, pp. 257–266, 2004.
- [56] D. Shindo, T. Oikawa, D. Shindo, and T. Oikawa, “Energy dispersive x-ray spectroscopy,” *Analytical electron microscopy for materials science*, pp. 81–102, 2002.
- [57] K. E. MacArthur, A. B. Yankovich, A. Béch e, M. Luysberg, H. G. Brown, S. D. Findlay, M. Heggen, and L. J. Allen, “Optimizing experimental conditions for accurate quantitative energy-dispersive x-ray analysis of interfaces at the atomic scale,” *Microsc. Microanal.*, vol. 27, pp. 528–542, 2021.
- [58] J. H. Jang, Y.-M. Kim, Q. He, R. Mishra, L. Qiao, M. D. Biegalski, A. R. Lupini, S. T. Pantelides, S. J. Pennycook, S. V. Kalinin, *et al.*, “In situ observation of oxygen vacancy dynamics and ordering in the epitaxial LaCoO₃ system,” *ACS nano*, vol. 11, pp. 6942–6949, 2017.
- [59] K. E. MacArthur, T. J. Slater, S. J. Haigh, D. Ozkaya, P. D. Nellist, and S. Lozano-Perez, “Quantitative energy-dispersive x-ray analysis of catalyst nanoparticles using a partial cross section approach,” *Microsc. Microanal.*, vol. 22, pp. 71–81, 2016.
- [60] G. Cliff and G. W. Lorimer, “The quantitative analysis of thin specimens,” *J. Microsc.*, vol. 103, pp. 203–207, 1975.
- [61] M. Phaneuf, “FIB for materials science applications-A review,” *Introduction to focused ion beams: Instrumentation, theory, techniques and practice*, pp. 143–172, 2005.
- [62] D. Delille, R. Pantel, and E. Van Cappellen, “Crystal thickness and extinction distance determination using energy filtered CBED pattern intensity measurement and dynamical diffraction theory fitting,” *Ultramicroscopy*, vol. 87, pp. 5–18, 2001.

-
- [63] S. M. Allen and E. L. Hall, "Foil thickness measurements from convergent-beam diffraction patterns an experimental assessment of errors," *Philos. Mag. A.*, vol. 46, pp. 243–253, 1982.
- [64] P. Delavignette and R. Vook, "A method for measuring the thickness of thin bent foils in transmission electron microscopy," *Phys. Status Solidi B*, vol. 3, pp. 648–653, 1963.
- [65] M. Luysberg, M. Heggen, and K. Tillmann, "FEI Tecnai G2 F20," *JLSRF*, vol. 2, pp. A77–A77, 2016.
- [66] J. Barthel, "Dr. Probe: A software for high-resolution STEM image simulation," *Ultramicroscopy*, vol. 193, pp. 1–11, 2018.
- [67] C. Boothroyd, A. Kovács, and K. Tillmann, "FEI Titan G2 60-300 HOLO," *Journal of large-scale research facilities JLSRF*, vol. 2, pp. A44–A44, 2016.
- [68] M. Lehmann, "Influence of the elliptical illumination on acquisition and correction of coherent aberrations in high-resolution electron holography," *Ultramicroscopy*, vol. 100, pp. 9–23, 2004.
- [69] A. Kovács, R. Schierholz, and K. Tillmann, "FEI Titan G2 80-200 CREWLEY," *JLSRF*, vol. 2, pp. A43–A43, 2016.
- [70] A. Sanchez, P. Galindo, S. Kret, M. Falke, R. Beanland, and P. Goodhew, "An approach to the systematic distortion correction in aberration-corrected haadf images," *J. Microsc.*, vol. 221, pp. 1–7, 2006.
- [71] P. Bayle, T. Deutsch, B. Gilles, F. Lançon, A. Marty, and J. Thibault, "Quantitative analysis of the deformation and chemical profiles of strained multilayers," *Ultramicroscopy*, vol. 56, pp. 94–107, 1994.
- [72] R. Bierwolf, M. Hohenstein, F. Phillipp, O. Brandt, G. Crook, and K. Ploog, "Direct measurement of local lattice distortions in strained layer structures by HREM," *Ultramicroscopy*, vol. 49, pp. 273–285, 1993.
- [73] M. Nord, P. E. Vullum, I. MacLaren, T. Tybell, and R. Holmestad, "Atomap: a new software tool for the automated analysis of atomic resolution images using two-dimensional gaussian fitting," *Adv. Struct. Chem.*, vol. 3, pp. 1–12, 2017.
- [74] J. Chung, G. Lian, and L. Rabenberg, "Practical and reproducible mapping of strains in Si devices using geometric phase analysis of annular dark-field images from scanning transmission electron microscopy," *IEEE Electron Device Lett.*, vol. 31, pp. 854–856, 2010.

- [75] H.-U. zu Berlin, “FRWRtools.” https://www.physik.hu-berlin.de/en/sem/software/software_frwrtools, 2021.
- [76] J. J. Peters, R. Beanland, M. Alexe, J. W. Cockburn, D. G. Revin, S. Y. Zhang, and A. M. Sanchez, “Artefacts in geometric phase analysis of compound materials,” *Ultramicroscopy*, vol. 157, pp. 91–97, 2015.
- [77] J.-F. Carlin and M. Ilegems, “High-quality AlInN for high index contrast Bragg mirrors lattice matched to GaN,” *Appl. Phys. Lett.*, vol. 83, pp. 668–670, 2003.
- [78] E.-H. Cirilin, J. J. Vajo, and T. Hasenberg, “Limiting factors for secondary ion mass spectrometry profiling,” *J. Vac. Sci. Technol.*, vol. 12, pp. 269–275, 1994.
- [79] M. Schnedler, V. Portz, H. Eisele, R. E. Dunin-Borkowski, and Ph. Ebert, “Polarity-dependent pinning of a surface state,” *Phys. Rev. B*, vol. 91, p. 205309, 2015.
- [80] L. Freter, Y. Wang, M. Schnedler, J.-F. Carlin, R. Butté, N. Grandjean, H. Eisele, R. E. Dunin-Borkowski, and P. Ebert, “Interplay of intrinsic and extrinsic states in pinning and passivation of m-plane facets of GaN n-p-n junctions,” *J. Appl. Phys.*, vol. 128, p. 185701, 2020.
- [81] M. McCartney and M. Gajdardziska-Josifovska, “Absolute measurement of normalized thickness, t/λ_i , from off-axis electron holography,” *Ultramicroscopy*, vol. 53, pp. 283–289, 1994.
- [82] V. Ravikumar, R. Rodrigues, and V. P. Dravid, “Direct imaging of spatially varying potential and charge across internal interfaces in solids,” *Phys. Rev. Lett.*, vol. 75, p. 4063, 1995.
- [83] L. A. Giannuzzi and F. A. Stevie, “A review of focused ion beam milling techniques for TEM specimen preparation,” *Micron*, vol. 30, pp. 197–204, 1999.
- [84] J. Mayer, L. A. Giannuzzi, T. Kamino, and J. Michael, “TEM sample preparation and FIB-induced damage,” *MRS Bull.*, vol. 32, pp. 400–407, 2007.
- [85] J. F. Ziegler, *The stopping and ranges of ions in matter*. Elsevier, 2013.
- [86] Y. Yabuuchi, S. Tametou, T. Okano, S. Inazato, S. Sadayama, Y. Yamamoto, K. Iwasaki, and Y. Sugiyama, “A study of the damage on FIB-prepared TEM samples of Al_xGa_{1-x}As,” *J. Electron Microsc.*, vol. 53, pp. 471–477, 2004.

-
- [87] S. Rubanov and P. Munroe, “FIB-induced damage in silicon,” *J. Microsc.*, vol. 214, pp. 213–221, 2004.
- [88] A. C. Twitchett, R. E. Dunin-Borkowski, and P. A. Midgley, “Quantitative Electron Holography of Biased Semiconductor Devices,” *Phys. Rev. Lett.*, vol. 88, p. 238302, 2002.
- [89] D. Cooper, A. C. Twitchett, P. K. Somodi, P. A. Midgley, R. E. Dunin-Borkowski, I. Farrer, and D. A. Ritchie, “Improvement in electron holographic phase images of focused-ion-beam-milled GaAs and Si p-n junctions by in situ annealing,” *Appl. Phys. Lett.*, vol. 88, p. 063510, 2006.
- [90] L. Amichi, I. Mouton, E. Di Russo, V. Boureau, F. Barbier, A. Dussaigne, A. Grenier, P.-H. Jouneau, C. Bougerol, and D. Cooper, “Three-dimensional measurement of Mg dopant distribution and electrical activity in GaN by correlative atom probe tomography and off-axis electron holography,” *J. Appl. Phys.*, vol. 127, p. 065702, 2020.
- [91] A. Pantzer, A. Vakahy, Z. Eliyahou, G. Levi, D. Horvitz, and A. Kohn, “Dopant mapping in thin FIB prepared silicon samples by off-axis electron holography,” *Ultramicroscopy*, vol. 138, pp. 36–45, 2014.
- [92] D. Cooper, F. Bertin, P. Salles, and G. Benassayag, “Focused ion beam specimen preparation for off-axis electron holography using Si, Ga, and Au ions,” *Appl. Phys. Lett.*, vol. 93, p. 043510, 2008.
- [93] D. Cooper, C. Ailliot, J.-P. Barnes, J.-M. Hartmann, P. Salles, G. Benassayag, and R. E. Dunin-Borkowski, “Dopant profiling of focused ion beam milled semiconductors using off-axis electron holography; reducing artifacts, extending detection limits and reducing the effects of gallium implantation,” *Ultramicroscopy*, vol. 110, pp. 383–389, 2010.
- [94] W. D. Rau, P. Schwander, F. H. Baumann, W. Höppner, and A. Ourmazd, “Two-Dimensional Mapping of the Electrostatic Potential in Transistors by Electron Holography,” *Phys. Rev. Lett.*, vol. 82, pp. 2614–2617, 1999.
- [95] B. Cai and D. A. Drabold, “Properties of amorphous GaN from first-principles simulations,” *Phys. Rev. B*, vol. 84, p. 075216, 2011.
- [96] W. Walukiewicz, “Intrinsic limitations to the doping of wide-gap semiconductors,” *Physica B*, vol. 302-303, p. 123, 2001.
- [97] Y. Dong, R. M. Feenstra, and J. Northrup, “Electronic states of oxidized GaN (0001) surfaces,” *Appl. Phys. Lett.*, vol. 89, 2006.

- [98] P. Sigmund and A. Schinner, “Binary theory of electronic stopping,” *Nucl. Instrum. Methods Phys. Res. B*, vol. 195, pp. 64–90, 2002.
- [99] J. F. Ziegler and J. P. Biersack, *The stopping and range of ions in matter*. Springer, 1985.
- [100] S. Suresh, “Cambridge solid state science series,” *Fatigue Mater.*, 1998.
- [101] J. F. Ziegler, M. D. Ziegler, and J. P. Biersack, “SRIM—The stopping and range of ions in matter (2010),” *Nucl. Instrum Methods Phys. Res. B*, vol. 268, pp. 1818–1823, 2010.
- [102] D. C. Look, D. Reynolds, Z.-Q. Fang, J. Hemsley, J. Sizelove, and R. Jones, “Point defect characterization of GaN and ZnO,” *Mater. Sci. Eng.*, vol. 66, pp. 30–32, 1999.
- [103] M. D. McCluskey and E. E. Haller, *Dopants and defects in semiconductors*. CRC press, 2018.
- [104] S. Limpijumnong and C. G. Van de Walle, “Diffusivity of native defects in GaN,” *Phys. Rev. B*, vol. 69, p. 035207, 2004.
- [105] A. Kyrtos, M. Matsubara, and E. Bellotti, “Migration mechanisms and diffusion barriers of carbon and native point defects in GaN,” *Phys. Rev. B*, vol. 93, p. 245201, 2016.
- [106] G. H. Vineyard, “Frequency factors and isotope effects in solid state rate processes,” *J. Phys. Chem. Solids*, vol. 3, pp. 121–127, 1957.
- [107] P. Erhart and K. Albe, “First-principles study of migration mechanisms and diffusion of oxygen in zinc oxide,” *Phys. Rev. B*, vol. 73, p. 115207, 2006.
- [108] J. L. Lyons, A. Janotti, and C. G. Van de Walle, “Effects of carbon on the electrical and optical properties of InN, GaN, and AlN,” *Phys. Rev. B*, vol. 89, p. 035204, 2014.
- [109] S. Zhang and J. E. Northrup, “Chemical potential dependence of defect formation energies in GaAs: Application to Ga self-diffusion,” *Phys. Rev. Lett.*, vol. 67, p. 2339, 1991.
- [110] A. Alkauskas, P. Deák, J. Neugebauer, A. Pasquarello, and C. G. Van de Walle, *Advanced Calculations for Defects in Materials: Electronic Structure Methods*. John Wiley & Sons, 2011.

-
- [111] C. Freysoldt, B. Grabowski, T. Hickel, J. Neugebauer, G. Kresse, A. Janotti, and C. G. Van de Walle, “First-principles calculations for point defects in solids,” *Rev. Mod. Phys.*, vol. 86, p. 253, 2014.
- [112] J. L. Lyons and C. G. V. de Walle, “Computationally predicted energies and properties of defects in GaN,” *npj Comput. Mater.*, vol. 3, p. 12, 2017.
- [113] D. Demchenko, I. Diallo, and M. Reshchikov, “Hydrogen-carbon complexes and the blue luminescence band in GaN,” *J. Appl. Phys.*, vol. 119, 2016.
- [114] M. Matsubara and E. Bellotti, “A first-principles study of carbon-related energy levels in GaN. I. Complexes formed by substitutional/interstitial carbons and gallium/nitrogen vacancies,” *J. Appl. Phys.*, vol. 121, p. 195701, 2017.
- [115] M. Matsubara and E. Bellotti, “A first-principles study of carbon-related energy levels in GaN. II. Complexes formed by carbon and hydrogen, silicon or oxygen,” *J. Appl. Phys.*, vol. 121, 2017.
- [116] D. Wolf, A. Lubk, A. Lenk, S. Sturm, and H. Lichte, “Tomographic investigation of Fermi-level pinning at focused ion beam milled semiconductor surfaces,” *Appl. Phys. Lett.*, vol. 103, 2013.
- [117] H. Sasaki, S. Otomo, R. Minato, K. Yamamoto, and T. Hirayama, “Direct observation of dopant distribution in GaAs compound semiconductors using phase-shifting electron holography and Lorentz microscopy,” *J. Electron Microsc.*, vol. 63, pp. 235–242, 2014.
- [118] J. Park, T. Niermann, and M. Lehmann, “Built-in potentials in GaN pn junctions measured by electron holography.”
- [119] M. Beleggia, P. F. Fazzini, P. Merli, and G. Pozzi, “Influence of charged oxide layers on TEM imaging of reverse-biased $p - n$ junctions,” *Phys. Rev. B*, vol. 67, p. 045328, 2003.
- [120] P. Somodi, A. Twitchett-Harrison, P. Midgley, B. Kardynał, C. Barnes, and R. Dunin-Borkowski, “Finite element simulations of electrostatic dopant potentials in thin semiconductor specimens for electron holography,” *Ultramicroscopy*, vol. 134, pp. 160–166, 2013.
- [121] M. Schnedler, V. Portz, P. H. Weidlich, R. E. Dunin-Borkowski, and Ph. Ebert, “Quantitative description of photoexcited scanning tunneling spectroscopy and its application to the GaAs(110) surface,” *Phys. Rev. B*, vol. 91, p. 235305, 2015.

- [122] V. Heine, “Theory of Surface States,” *Phys. Rev.*, vol. 138, pp. A1689–A1696, 1965.
- [123] F. Stern and W. E. Howard, “Properties of Semiconductor Surface Inversion Layers in the Electric Quantum Limit,” *Phys. Rev.*, vol. 163, pp. 816–835, 1967.
- [124] R. Seiwitz and M. Green, “Space Charge Calculations for Semiconductors,” *J. Appl. Phys.*, vol. 29, pp. 1034–1040, 1958.
- [125] S. M. Sze and K. K. Ng, *Physics of Semiconductor Devices*. New York: Wiley-Interscience, 3 ed., 2007.
- [126] N. D. Jäger, *Effects of individual dopant atoms on the electronic properties of GaAs investigated by scanning tunneling microscopy and spectroscopy*. Berichte des Forschungszentrum Jülich, Jülich: Forschungszentrum Jülich GmbH, 2003.
- [127] R. M. Feenstra, “Tunneling spectroscopy of the (110) surface of direct-gap III-V semiconductors,” *Phys. Rev. B*, vol. 50, pp. 4561–4570, 1994.
- [128] S. Selberherr, *Analysis and Simulation of Semiconductor Devices*. Vienna, New York: Springer, 1984.
- [129] R. M. Feenstra, “SEMITIP version 6.” http://www.andrew.cmu.edu/user/feenstra/semitip_v6, 2011.
- [130] F. Bernardini, V. Fiorentini, and D. Vanderbilt, “Spontaneous polarization and piezoelectric constants of III-V nitrides,” *Phys. Rev. B*, vol. 56, p. R10024, 1997.
- [131] I. Vurgaftman, J. á. Meyer, and L. R. Ram-Mohan, “Band parameters for III–V compound semiconductors and their alloys,” *J. Appl. Phys.*, vol. 89, pp. 5815–5875, 2001.
- [132] H. Morkoc and J. Leach, “Polarization in GaN Based heterostructures and heterojunction field effect transistors (HFETs),” *Polarization Effects in Semiconductors: From Ab Initio Theory to Device Applications*, pp. 373–466, 2008.
- [133] P. Gangwani, S. Pandey, S. Haldar, M. Gupta, and R. Gupta, “Polarization dependent analysis of AlGaIn/GaN HEMT for high power applications,” *SSEL*, vol. 51, pp. 130–135, 2007.

-
- [134] L. Shen, R. Coffie, D. Buttari, S. Heikman, A. Chakraborty, A. Chini, S. Keller, S. DenBaars, and U. Mishra, "High-power polarization-engineered GaN/AlGa_N/Ga_N HEMTs without surface passivation," *IEEE Electron Device Lett.*, vol. 25, pp. 7–9, 2004.
- [135] B. K. Jebalin, A. S. Rekh, P. Prajooon, D. Godwinraj, N. M. Kumar, and D. Nirmal, "Unique model of polarization engineered AlGa_N/Ga_N based HEMTs for high power applications," *SUPERLATTICE MICROST.*, vol. 78, pp. 210–223, 2015.
- [136] M. Leroux, N. Grandjean, M. Laügt, J. Massies, B. Gil, P. Lefebvre, and P. Bigenwald, "Quantum confined Stark effect due to built-in internal polarization fields in (Al, Ga) N/Ga_N quantum wells," *Phys. Rev. B.*, vol. 58, p. R13371, 1998.
- [137] H. Morkoç, R. Cingolani, and B. Gil, "Polarization effects in nitride semiconductor device structures and performance of modulation doped field effect transistors," *Solid State Electron. Lett.*, vol. 43, pp. 1909–1927, 1999.
- [138] R. M. Martin, "Piezoelectricity," *Phys. Rev. B.*, vol. 5, p. 1607, 1972.
- [139] M. Feneberg and K. Thonke, "Polarization fields of III-nitrides grown in different crystal orientations," *J. Condens. Matter Phys.*, vol. 19, p. 403201, 2007.
- [140] C. E. Dreyer, A. Janotti, C. G. Van de Walle, and D. Vanderbilt, "Correct Implementation of Polarization Constants in Wurtzite Materials and Impact on III-Nitrides," *Phys. Rev. X*, vol. 6, p. 021038, 2016.
- [141] R. Resta, "Macroscopic polarization in crystalline dielectrics: the geometric phase approach," *RMP*, vol. 66, p. 899, 1994.
- [142] K. M. Rabe, M. Dawber, C. Lichtensteiger, C. H. Ahn, and J.-M. Triscone, *Modern physics of ferroelectrics: Essential background*. Springer, 2007.
- [143] F. Bernardini, V. Fiorentini, and D. Vanderbilt, "Accurate calculation of polarization-related quantities in semiconductors," *Phys. Rev. B*, vol. 63, p. 193201, 2001.
- [144] F. Bernardini and V. Fiorentini, "Nonlinear macroscopic polarization in III-V nitride alloys," *Phys. Rev. B*, vol. 64, p. 085207, 2001.
- [145] D. Vanderbilt, "Berry-phase theory of proper piezoelectric response," *J. Phys. Chem. Solids*, vol. 61, pp. 147–151, 2000.

- [146] Q. Yan, P. Rinke, A. Janotti, M. Scheffler, and C. G. Van de Walle, “Effects of strain on the band structure of group-III nitrides,” *Phys. Rev. B*, vol. 90, p. 125118, 2014.
- [147] J. Van Vechten and T. Bergstresser, “Electronic structures of semiconductor alloys,” *Phys. Rev. B*, vol. 1, p. 3351, 1970.
- [148] K. Nam, J. Li, M. Nakarmi, J. Lin, and H. Jiang, “Unique optical properties of AlGa_N alloys and related ultraviolet emitters,” *Appl. Phys. Lett.*, vol. 84, pp. 5264–5266, 2004.
- [149] C. Buchheim, R. Goldhahn, M. Rakel, C. Cobet, N. Esser, U. Rossow, D. Fuhrmann, and A. Hangleiter, “Dielectric function and critical points of the band structure for AlGa_N alloys,” *Phys. Status Solidi B*, vol. 242, pp. 2610–2616, 2005.
- [150] R. R. Pelá, C. Caetano, M. Marques, L. G. Ferreira, J. Furthmüller, and L. K. Teles, “Accurate band gaps of AlGa_N, InGa_N, and AlIn_N alloys calculations based on LDA-1/2 approach,” *Appl. Phys. Lett.*, vol. 98, p. 151907, 2011.
- [151] G. Orsal, Y. El Gmili, N. Fressengeas, J. Streque, R. Djerboub, T. Moudakir, S. Sundaram, A. Ougazzaden, and J.-P. Salvestrini, “Bandgap energy bowing parameter of strained and relaxed InGa_N layers,” *Opt. Mater. Express*, vol. 4, pp. 1030–1041, 2014.
- [152] P. Schley, R. Goldhahn, A. Winzer, G. Gobsch, V. Cimalla, O. Ambacher, H. Lu, W. Schaff, M. Kurouchi, Y. Nanishi, *et al.*, “Dielectric function and Van Hove singularities for In-rich In_xGa_{1-x}N alloys: Comparison of N- and metal-face materials,” *Phys. Rev. B*, vol. 75, p. 205204, 2007.
- [153] M. Ferhat and F. Bechstedt, “First-principles calculations of gap bowing in In_xGa_{1-x}N and In_xAl_{1-x}N alloys: relation to structural and thermodynamic properties,” *Phys. Rev. B*, vol. 65, p. 075213, 2002.
- [154] S. Schulz, M. A. Caro, L.-T. Tan, P. J. Parbrook, R. W. Martin, and E. P. O’Reilly, “Composition-Dependent Band Gap and Band-Edge Bowing in AlIn_N: A Combined Theoretical and Experimental Study,” *Appl. Phys. Express*, vol. 6, p. 121001, 2013.
- [155] S. N. Alam, V. Z. Zubialevich, B. Ghafary, and P. J. Parbrook, “Bandgap and refractive index estimates of InAlN and related nitrides across their full composition ranges,” *Sci. Rep.*, vol. 10, pp. 1–9, 2020.

-
- [156] V. Z. Zubialevich, D. V. Dinh, S. N. Alam, S. Schulz, E. P. O'Reilly, and P. J. Parbrook, "Strongly nonparabolic variation of the band gap in $\text{In}_x\text{Al}_{1-x}\text{N}$ with low indium content," *Semicond. Sci. Technol.*, vol. 31, p. 025006, 2015.
- [157] P. Rinke, M. Winkelnkemper, A. Qteish, D. Bimberg, J. Neugebauer, and M. Scheffler, "Consistent set of band parameters for the group-III nitrides AlN , GaN , and InN ," *Phys. Rev. B*, vol. 77, p. 075202, 2008.
- [158] N. Bouarissa, "Electron and positron energy levels and deformation potentials in group-III Nitrides," *Phys. Status Solidi B*, vol. 231, pp. 391–402, 2002.
- [159] Y. C. Yeo, T. C. Chong, and M. F. Li, "Electronic band structures and effective-mass parameters of wurtzite GaN and InN ," *J. Appl. Phys.*, vol. 83, p. 1429, 1998.
- [160] J. S. Escher, "NEA Semiconductor Photoemitters," *Semiconductors and Semimetals*, vol. 15, pp. 195–300, 1981.
- [161] J. I. Pankove and H. Schade, "Photoemission from GaN ," *Appl. Phys. Lett.*, vol. 25, p. 53, 1974.
- [162] V. M. Bermudez, T. M. Jung, K. Doverspike, and A. E. Wickenden, "The growth and properties of Al and AlN films on $\text{GaN}(0001)-(1 \times 1)$," *J. Appl. Phys.*, vol. 79, p. 110, 1996.
- [163] C.-L. Wu, H.-M. Lee, C.-T. Kuo, C.-H. Chen, and S. Gwo, "Absence of Fermi-Level Pinning at Cleaved Nonpolar InN Surfaces," *Phys. Rev. Lett.*, vol. 101, p. 106803, 2008.
- [164] N. Spyropoulos-Antonakakis, E. Sarantopoulou, Z. Kollia, G. Dražić, and S. Kobe, "Schottky and charge memory effects in InN nanodomains," *Appl. Phys. Lett.*, vol. 99, p. 153110, 2011.
- [165] P. Hacke, T. Detchprohm, K. Hiramatsu, and N. Sawaki, "Schottky barrier on n -type GaN grown by hydride vapor phase epitaxy," *Appl. Phys. Lett.*, vol. 63, p. 2676, 1993.
- [166] P. G. Moses, M. Miao, Q. Yan, and C. G. Van de Walle, "Hybrid functional investigations of band gaps and band alignments for AlN , GaN , InN , and InGaN ," *J. Chem. Phys.*, vol. 134, p. 084703, 2011.
- [167] M. Akazawa, T. Matsuyama, T. Hashizume, M. Hiroki, S. Yamahata, and N. Shigekawa, "Small valence-band offset of $\text{In}_{0.17}\text{Al}_{0.83}\text{N}/\text{GaN}$ heterostructure grown by metal-organic vapor phase epitaxy," *Appl. Phys. Lett.*, vol. 96, p. 132104, 2010.

- [168] W. Jiao, W. Kong, J. Li, K. Collar, T.-H. Kim, M. Losurdo, and A. S. Brown, "Characterization of MBE-grown InAlN/GaN heterostructure valence band offsets with varying In composition," *AIP Advances*, vol. 6, p. 035211, 2016.
- [169] J. Wang, F. Xu, X. Zhang, W. An, X.-Z. Li, J. Song, W. Ge, G. Tian, J. Lu, X. Wang, *et al.*, "Evidence of Type-II Band Alignment in III-nitride Semiconductors: Experimental and theoretical investigation for In_{0.17}Al_{0.83}N/GaN heterostructures," *Sci. Rep.*, vol. 4, p. 6521, 2014.
- [170] Y.-C. Tsai and C. Bayram, "Band alignments of ternary wurtzite and zincblende III-nitrides investigated by hybrid density functional theory," *ACS omega*, vol. 5, pp. 3917–3923, 2020.
- [171] H. Bethe, "Theory on the diffraction of electrons in crystals," *Ann. Phys.*, vol. 87, 1928.
- [172] A. Sanchez and M. Ochoa, "Calculation of the mean inner potential," *J. Solid State Phys.*, vol. 18, p. 33, 1985.
- [173] J. Ibers, "Atomic scattering amplitudes for electrons," *Acta Crystallogr.*, vol. 11, pp. 178–183, 1958.
- [174] M. Kim, J. Zuo, and J. Spence, "Ab-initio LDA Calculations of the Mean Coulomb Potential V₀ in Slabs of Crystalline Si, Ge and MgO," *Phys. Status Solidi*, vol. 166, pp. 445–451, 1998.
- [175] A. Lubk, D. Wolf, and H. Lichte, "The effect of dynamical scattering in off-axis holographic mean inner potential and inelastic mean free path measurements," *Ultramicroscopy*, vol. 110, pp. 438–446, 2010.
- [176] M. Schowalter, A. Rosenauer, D. Lamoen, P. Kruse, and D. Gerthsen, "Ab initio computation of the mean inner Coulomb potential of wurtzite-type semiconductors and gold," *Appl. Phys. Lett.*, vol. 88, p. 232108, 2006.
- [177] P. Kruse, M. Schowalter, D. Lamoen, A. Rosenauer, and D. Gerthsen, "Determination of the mean inner potential in III–V semiconductors, Si and Ge by density functional theory and electron holography," *Ultramicroscopy*, vol. 106, pp. 105–113, 2006.
- [178] P. Kruse, A. Rosenauer, and D. Gerthsen, "Determination of the mean inner potential in III–V semiconductors by electron holography," *Ultramicroscopy*, vol. 96, pp. 11–16, 2003.

- [179] M. Gajdardziska-Josifovska, M. McCartney, W. De Ruijter, D. J. Smith, J. Weiss, and J. Zuo, "Accurate measurements of mean inner potential of crystal wedges using digital electron holograms," *Ultramicroscopy*, vol. 50, pp. 285–299, 1993.
- [180] A. S. W. Wong, G. W. Ho, R. E. Dunin-Borkowski, T. Kasama, R. A. Oliver, P. M. Costa, and C. J. Humphreys, "The mean inner potential of gan measured from nanowires using off-axis electron holography," *MRS Online Proceedings Library (OPL)*, vol. 892, 2005.
- [181] M. Deguchi, S. Tanaka, and T. Tanji, "Determination of piezoelectric fields across InGaN/GaN quantum wells by means of electron holography," *J. Electron. Mater.*, vol. 39, pp. 815–818, 2010.
- [182] D. Cherns, J. Barnard, and F. Ponce, "Measurement of the piezoelectric field across strained InGaN/GaN layers by electron holography," *Solid State Commun.*, vol. 111, pp. 281–285, 1999.
- [183] L. Denaix, F. Castioni, M. Bryan, D. Cooper, and E. Monroy, "Inversion of the Internal Electric Field Due to Inhomogeneous Incorporation of Ge Dopants in GaN/AlN Heterostructures Studied by Off-Axis Electron Holography," *ACS Applied Materials & Interfaces*, vol. 15, pp. 11208–11215, 2023.
- [184] S. R. Alugubelli, H. Fu, K. Fu, H. Liu, Y. Zhao, M. R. McCartney, and F. A. Ponce, "Determination of electronic band structure by electron holography of etched-and-regrown interfaces in GaN pin diodes," *Appl. Phys. Lett.*, vol. 115, 2019.
- [185] N. Ikarashi, T. Ikezawa, K. Uejima, T. Fukai, M. Miyamura, A. Toda, and M. Hane, "Electron holography analysis of a shallow junction for planar-bulk metal-oxide-semiconductor field-effect transistors approaching the scaling limit," *J. Appl. Phys.*, vol. 103, 2008.
- [186] D. Shindo and Y. Murakami, "Electron holography study of electric field variations," *J. Electron Microsc.*, vol. 60, pp. S225–S237, 2011.
- [187] J. H. Yoo, J.-M. Yang, S. Ulugbek, C. W. Ahn, W.-J. Hwang, J. K. Park, C. M. Park, S. B. Hong, J. J. Kim, and D. Shindo, "Electron holography study for two-dimensional dopant profile measurement with specimens prepared by backside ion milling," *J. Electron Microsc.*, vol. 57, pp. 13–18, 2008.

- [188] S. Yazdi, T. Kasama, M. Beleggia, M. S. Yekta, D. W. McComb, A. C. Twitchett-Harrison, and R. E. Dunin-Borkowski, “Towards quantitative electrostatic potential mapping of working semiconductor devices using off-axis electron holography,” *Ultramicroscopy*, vol. 152, pp. 10–20, 2015.
- [189] K. Ji, M. Schnedler, Q. Lan, J.-F. Carlin, R. Butté, N. Grandjean, R. E. Dunin-Borkowski, and P. Ebert, “Origin of giant enhancement of phase contrast in electron holography of modulation-doped *n*-type GaN,” *Ultramicroscopy*, vol. 264, p. 114006, 2024.
- [190] K. Ji, M. Schnedler, Q. Lan, F. Zheng, Y. Wang, Y. Lu, H. Eisele, J.-F. Carlin, R. Butté, N. Grandjean, R. E. Dunin-Borkowski, and P. Ebert, “Identification and thermal healing of focused ion beam-induced defects in GaN using off-axis electron holography,” *Appl. Phys. Express*, vol. 17, p. 016505, 2024.
- [191] R. B. Dingle, “Scattering of electrons and holes by charged donors and acceptors in semiconductors,” *Philos. Mag.*, vol. 7, p. 831, 1955.
- [192] D. Cooper, “Off-axis electron holography for the measurement of active dopants in silicon semiconductor devices,” *J. Phys. D: Appl. Phys*, vol. 49, p. 474001, 2016.
- [193] M. Gribelyuk, M. McCartney, J. Li, C. Murthy, P. Ronsheim, B. Doris, J. McMurray, S. Hegde, and D. J. Smith, “Mapping of electrostatic potential in deep submicron cmos devices by electron holography,” *Phys. Rev. Lett.*, vol. 89, p. 025502, 2002.
- [194] Z. Wang, K. Sasaki, N. Kato, K. Urata, T. Hirayama, and H. Saka, “Examination of electrostatic potential distribution across an implanted p–n junction by electron holography,” *Microscopy*, vol. 50, pp. 479–484, 2001.
- [195] S. Anada, K. Yamamoto, H. Sasaki, N. Shibata, Y. Hori, K. Kinugawa, A. Imamura, and T. Hirayama, “Precise measurement of electric potential, field, and charge density profiles across a biased GaAs pn tunnel junction by in situ phase-shifting electron holography,” *J. Appl. Phys.*, vol. 122, 2017.
- [196] H. Hebal, Z. Koziol, S. Lisesivdin, and R. Steed, “General-purpose open-source 1d self-consistent schrödinger-poisson solver: Aestimo 1d,” *Comput. Mater. Sci.*, vol. 186, p. 110015, 2021.
- [197] A. Boley, D. Storm, M. McCartney, and D. Smith, “Characterization of N-polar GaN/AlGa_N/GaN Heterostructures Using Electron Holography,” *Microsc. Microanal.*, vol. 20, pp. 258–259, 2014.

-
- [198] T. Zhu and R. A. Oliver, “Unintentional doping in GaN,” *Phys. Chem. Chem. Phys.*, vol. 14, pp. 9558–9573, 2012.
- [199] V. Boureau and D. Cooper, “Highly spatially resolved mapping of the piezoelectric potentials in InGaN quantum well structures by off-axis electron holography,” *J. Appl. Phys.*, vol. 128, p. 155704, 2020.
- [200] D. Cooper, V. Boureau, A. Even, F. Barbier, and A. Dussaigne, “Determination of the internal piezoelectric potentials and indium concentration in InGaN based quantum wells grown on relaxed InGaN pseudo-substrates by off-axis electron holography,” *Nanotechnology*, vol. 31, p. 475705, 2020.
- [201] P. H. Weidlich, M. Schnedler, H. Eisele, U. Strauß, R. E. Dunin-Borkowski, and Ph. Ebert, “Evidence of deep traps in overgrown v-shaped defects in epitaxial GaN layers,” *Appl. Phys. Lett.*, vol. 103, p. 062101, 2013.
- [202] H. Eisele and Ph. Ebert, “Non-polar group-III nitride semiconductor surfaces,” *Phys. Stat. Sol. RRL*, vol. 6, pp. 359–369, 2012.
- [203] N. Jiang, “Electron beam damage in oxides: a review,” *Reports on Progress in Physics*, vol. 79, p. 016501, 2015.
- [204] T. K. Zywietz, J. Neugebauer, and M. Scheffler, “The adsorption of oxygen at GaN surfaces,” *Appl. Phys. Lett.*, vol. 74, pp. 1695–1697, 1999.
- [205] M. Schnedler, *Quantitative scanning tunneling spectroscopy of non-polar compound semiconductor surfaces*. PhD thesis, RWTH Aachen University, 2015.
- [206] T. Mattila and R. M. Nieminen, “Point-defect complexes and broadband luminescence in GaN and AlN,” *Phys. Rev. B*, vol. 55, p. 9571, 1997.
- [207] T. Mattila and R. M. Nieminen, “Ab initio study of oxygen point defects in GaAs, GaN, and AlN,” *Phys. Rev. B*, vol. 54, p. 16676, 1996.
- [208] C. G. Van de Walle, “Interactions of hydrogen with native defects in GaN,” *Phys. Rev. B*, vol. 56, p. R10020, 1997.
- [209] D.-H. Yeh, L.-Z. Hsieh, L.-B. Chang, and M.-J. Jeng, “The characteristics of platinum diffusion in n-type GaN,” *Appl. Surf. Sci.*, vol. 253, pp. 6910–6914, 2007.
- [210] J. Lyons, A. Janotti, and C. Van de Walle, “Carbon impurities and the yellow luminescence in GaN,” *Appl. Phys. Lett.*, vol. 97, p. 152108, 2010.
- [211] N. T. Farr, G. M. Hughes, and C. Rodenburg, “Monitoring carbon in electron and ion beam deposition within FIB-SEM,” *Materials*, vol. 14, p. 3034, 2021.

- [212] H. Oettel and H. Schumann, *Metallografie: Mit einer Einführung in die Keramografie*. Weinheim: Wiley-VCH, 2011.
- [213] O. Ambacher, M. S. Brandt, R. Dimitrov, T. Metzger, M. Stutzmann, R. A. Fischer, A. Miehr, A. Bergmaier, and G. Dollinger, “Thermal stability and desorption of Group III nitrides prepared by metal organic chemical vapor deposition,” *J. Vac. Sci. Technol. B*, vol. 14, pp. 3532–3542, 1996.
- [214] P. Deák, M. Lorke, B. Aradi, and T. Frauenheim, “Carbon in GaN: Calculations with an optimized hybrid functional,” *Phys. Rev. B*, vol. 99, p. 085206, 2019.
- [215] M. A. Reshchikov, D. Demchenko, A. Usikov, H. Helava, and Y. Makarov, “Carbon defects as sources of the green and yellow luminescence bands in undoped GaN,” *Phys. Rev. B*, vol. 90, p. 235203, 2014.
- [216] D. O. Demchenko, I. C. Diallo, and M. A. Reshchikov, “Yellow luminescence of gallium nitride generated by carbon defect complexes,” *Phys. Rev. Lett.*, vol. 110, p. 087404, 2013.
- [217] J. L. Lyons, E. R. Glaser, M. E. Zvanut, S. Paudel, M. Iwinska, T. Sochacki, and M. Bockowski, “Carbon complexes in highly C-doped GaN,” *Phys. Rev. B*, vol. 104, p. 075201, 2021.
- [218] J. Manning, *Diffusion Kinetics for Atoms in Crystals*. Princeton: Van Nostrand, 1968.
- [219] D.-S. Tang and L.-M. Zhang, “Phonon modes and topological phonon properties in $(\text{GaN})_x/(\text{AlN})_x$ and $(\text{AlGaIn})_x/(\text{GaN})_x$ superlattices,” *Phys. Scr.*, vol. 98, p. 085934, 2023.
- [220] B. D. Cullity, “Elements of x-ray diffraction, addison,” *Wesley Mass*, pp. 127–31, 1978.
- [221] Y. Arakawa, “Progress in GaN-based quantum dots for optoelectronics applications,” *IEEE J. Sel. Top Quantum Electron.*, vol. 8, pp. 823–832, 2002.
- [222] M. Higashiwaki and T. Matsui, “Estimation of band-gap energy of intrinsic InN from photoluminescence properties of undoped and Si-doped InN films grown by plasma-assisted molecular-beam epitaxy,” *J. Cryst. Growth*, vol. 269, pp. 162–166, 2004.
- [223] J. Piprek, *Nitride semiconductor devices: principles and simulation*. John Wiley & Sons, 2007.

-
- [224] K. Hiramatsu, Y. Kawaguchi, M. Shimizu, N. Sawaki, T. Zheleva, R. F. Davis, H. Tsuda, W. Taki, N. Kuwano, and K. Oki, "The composition pulling effect in MOVPE grown InGaN on GaN and AlGaN and its TEM characterization," *MRS Internet J. Nitride Semicond. Res.*, vol. 2, pp. 1–12, 1997.
- [225] B. Liu, R. Zhang, J. Zheng, X. Ji, D. Fu, Z. Xie, D. Chen, P. Chen, R. Jiang, and Y. Zheng, "Composition pulling effect and strain relief mechanism in AlGaN/AlN distributed Bragg reflectors," *Appl. Phys. Lett.*, vol. 98, 2011.
- [226] Z. Chen, Y. Pei, S. Newman, D. Brown, R. Chung, S. Keller, S. DenBaars, S. Nakamura, and U. Mishra, "Growth of AlGaIn/GaN/AlGaIn double hetero-junction field-effect transistors and the observation of a compositional pulling effect," *Appl. Phys. Lett.*, vol. 94, 2009.
- [227] C. He, Z. Qin, F. Xu, L. Zhang, J. Wang, M. Hou, S. Zhang, X. Wang, W. Ge, and B. Shen, "Mechanism of stress-driven composition evolution during hetero-epitaxy in a ternary AlGaIn system," *Sci. Rep.*, vol. 6, p. 25124, 2016.
- [228] K. Lorenz, N. Franco, E. Alves, S. Pereira, I. Watson, R. Martin, and K. O'Donnell, "Relaxation of compressively strained AlInN on GaN," *J. Cryst. Growth*, vol. 310, pp. 4058–4064, 2008.
- [229] J. Manuel, F. Morales, J. Lozano, D. González, R. García, T. Lim, L. Kirste, R. Aidam, and O. Ambacher, "Structural and compositional homogeneity of InAlN epitaxial layers nearly lattice-matched to GaN," *Acta Mater.*, vol. 58, pp. 4120–4125, 2010.
- [230] W. Jiao, W. Kong, J. Li, K. Collar, T.-H. Kim, and A. S. Brown, "The relationship between depth-resolved composition and strain relaxation in In-AlN and InGaIn films grown by molecular beam epitaxy," *Appl. Phys. Lett.*, vol. 103, 2013.
- [231] S. Choi, T.-H. Kim, A. Brown, H. O. Everitt, M. Losurdo, G. Bruno, and A. Moto, "Kinetics of gallium adsorption and desorption on (0001) gallium nitride surfaces," *Appl. Phys. Lett.*, vol. 89, p. 181915, 2006.
- [232] J. E. Northrup, J. Neugebauer, R. Feenstra, and A. Smith, "Structure of GaN (0001): The laterally contracted Ga bilayer model," *Phys. Rev. B*, vol. 61, p. 9932, 2000.
- [233] J.-F. Carlin, C. Zellweger, J. Dorsaz, S. Nicolay, G. Christmann, E. Feltrin, R. Butté, and N. Grandjean, "Progresses in III-nitride distributed Bragg

- reflectors and microcavities using AlInN/GaN materials,” *Phys. Status Solidi B*, vol. 242, pp. 2326–2344, 2005.
- [234] D. Green, E. Haus, F. Wu, L. Chen, U. Mishra, and J. Speck, “Polarity control during molecular beam epitaxy growth of Mg-doped GaN,” *J. Vac. Sci. Technol.*, vol. 21, pp. 1804–1811, 2003.
- [235] E. Ruiz, S. Alvarez, and P. Alemany, “Electronic structure and properties of AlN,” *Phys. Rev. B*, vol. 49, p. 7115, 1994.
- [236] A. K. Kandalam, R. Pandey, M. Blanco, A. Costales, J. Recio, and J. M. Newsam, “First principles study of polyatomic clusters of AlN, GaN, and InN. 1. Structure, stability, vibrations, and ionization,” *J. Phys. Chem. B*, vol. 104, pp. 4361–4367, 2000.

Acknowledgement

I started my PhD student career just during the Covid-19 pandemic, a period that presented numerous challenges and uncertainties. After three more years, I finally reached the finish line and at this moment I want to extend my heartfelt gratitude to the outstanding individuals who provided support and guidance throughout this journey.

I would like to express my sincere gratitude to Prof. Dr. R. Dunin-Borkowski, who provided the funding and co-supervision my PhD thesis at the Ernst Ruska-Centrum für Mikroskopie und Spektroskopie mit Elektronen (ER-C) in the Forschungszentrum Jülich. Your profound expertise in the electron holography has played a pivotal role in shaping the trajectory of my research. I am sincerely grateful for the insightful ideas and unwavering guidance that you have graciously shared with me.

I would like to express my heartfelt gratitude to Prof. Dr. J. Mayer from the Gemeinschaftslabor für Elektronenmikroskopie (GFE) der RWTH Aachen for the supervision of my PhD thesis. Furthermore, I am indebted for the enriching experience derived from Prof. Dr. J. Mayer's excellent TEM-related courses, which have played a pivotal role in enhancing my comprehension of this field.

I would like to extend my immense gratitude to Priv.-Doz. Dr. Ph. Ebert for guiding me through my PhD career and for engaging in invaluable scientific discussions that form the foundation of this thesis. Your profound expertise in surface science has been a tremendous source of inspiration for me, and I greatly appreciate all the amazing ideas you've shared, which makes a significant impact on the overall quality and depth of my work.

I wish to convey my immense gratitude to Dr. M. Schnedler for engaging in extensive and enlightening discussions on scientific endeavors, with a particular focus on the simulation of my research data. The incorporation of the term "quantitative" in my thesis owes its realization to Dr. Schnedler's invaluable suggestions and collaborative efforts. Your insights have significantly enriched the scientific depth of my work, for which I am truly grateful.

Acknowledgement

I express my sincere appreciation to Dr. Q. Lan for providing exceptional mentoring and guidance in the comprehension and utilization of TEMs and FIB. Each moment devoted to learning from Dr. Lan in the TEM room has played a crucial role in elevating my knowledge and refining my skills in these advanced techniques. Furthermore, I am genuinely grateful for Dr. Lan's invaluable contribution to my scientific research endeavors.

I extend my sincere gratitude to Prof. Dr. N. Grandjean, Dr. R. Butté, and Dr. J.-F. Carlin from Ecole Polytechnique Fédérale de Lausanne, Switzerland, for generous providing of samples and assistance in interpreting and assessing the experimental results.

I would like to thank Dr. L. Freter, Dr. Y. Lu, Dr. Y. Wang, Mrs. X. Bai, and Prof. F. Zheng, for the involvement in the initial experiments and simulations.

I also would like to sincerely thank Prof. Dr. H. Eisele from the Institut für Physik, Otto-von-Guericke Universität Magdeburg for valuable scientific discussions.

I would like to sincerely thank Dr. D. Rosenzweig for the fruitful scientific discussions.

I would like to sincerely thank Dr. L. Lymperakis from the Department of Physics, University of Crete for fruitful discussions on the growth interruption model of group III-nitrides.

I would like to sincerely thank Dr. J. Jo, Dr. A. H. Tavabi, Mr. P. Lu, Dr. T. Denneulin, Dr. A. Kovács, and Ms. L. Risters for introducing me to the TEMs and FIBs as well as related techniques.

I would like to sincerely thank U. Breuer from the ZEA-3 at the Forschungszentrum Jülich, for the SIMS measurements.

A special appreciation to my parents and my wife Penny, for thier love and support.

This thesis is carried out with the Ernst Ruska-Centrum für Mikroskopie und Spektroskopie mit Elektronen (ER-C) in Forschungszentrum Jülich, with the financial support provided by the AIDAS project - AI, Data Analytics and Scalable Simulation, France - which is a Joint Virtual Laboratory gathering the Forschungszentrum Jülich (FZJ) and the French Alternative Energies and Atomic Energy Commission (CEA).

Band / Volume 92

Computational study of structural and optical properties of two-dimensional transition-metal dichalcogenides with implanted defects

S. H. Rost (2023), xviii, 198 pp

ISBN: 978-3-95806-682-3

Band / Volume 93

DC and RF characterization of bulk CMOS and FD-SOI devices at cryogenic temperatures with respect to quantum computing applications

A. Artanov (2023), xv, 80, xvii-lviii pp

ISBN: 978-3-95806-687-8

Band / Volume 94

HAXPES study of interface and bulk chemistry of ferroelectric HfO₂ capacitors

T. Szyjka (2023), viii, 120 pp

ISBN: 978-3-95806-692-2

Band / Volume 95

A brain inspired sequence learning algorithm and foundations of a memristive hardware implementation

Y. Bouhadjar (2023), xii, 149 pp

ISBN: 978-3-95806-693-9

Band / Volume 96

Characterization and modeling of primate cortical anatomy and activity

A. Morales-Gregorio (2023), ca. 260 pp.

ISBN: 978-3-95806-698-4

Band / Volume 97

Hafnium oxide based memristive devices as functional elements of neuromorphic circuits

F. J. Cüppers (2023), vi, ii, 214 pp

ISBN: 978-3-95806-702-8

Band / Volume 98

Simulation and theory of large-scale cortical networks

A. van Meegen (2023), ca. 250 pp

ISBN: 978-3-95806-708-0

Band / Volume 99

Structure of two-dimensional multilayers and topological superconductors: surfactant mediated growth, intercalation, and doping

Y.-R. Lin (2023), x, 111 pp

ISBN: 978-3-95806-716-5

Band / Volume 100

Frequency mixing magnetic detection for characterization and multiplex detection of superparamagnetic nanoparticles

A. M. Pourshahidi (2023), X, 149 pp

ISBN: 978-3-95806-727-1

Band / Volume 101

Unveiling the relaxation dynamics of Ag/HfO₂ based diffusive memristors for use in neuromorphic computing

S. A. Chekol (2023), x, 185 pp

ISBN: 978-3-95806-729-5

Band / Volume 102

Analysis and quantitative comparison of neural network dynamics on a neuron-wise and population level

R. Gutzen (2024), xii, 252 pp

ISBN: 978-3-95806-738-7

Band / Volume 103

3D Scaffolds with Integrated Electrodes for Neuronal Cell Culture

J. Abu Shihada (2024), vii, 163 pp

ISBN: 978-3-95806-756-1

Band / Volume 104

Advances in Photoemission Orbital Tomography

A. Haags (2024), ix, 254 pp

ISBN: 978-3-95806-766-0

Band / Volume 105

Quantitative investigation of point defects and their dynamics in focused ion beam-prepared group III-nitride lamellas by off-axis electron holography

K. Ji (2024), 164 pp

ISBN: 978-3-95806-782-0

Weitere **Schriften des Verlags im Forschungszentrum Jülich** unter
<http://www.zb1.fz-juelich.de/verlagextern1/index.asp>

Information

Band / Volume 105

ISBN 978-3-95806-782-0